

PLANETARY INFRARED OBSERVATIONS:
THE OCCULTATION OF 28 SAGITTARII BY SATURN AND
THE DYNAMICS OF JUPITER'S ATMOSPHERE

by

Joseph Harrington

S. B., Physics

Massachusetts Institute of Technology, 1988

Submitted to the

Department of Earth, Atmospheric, and Planetary Sciences
in partial fulfillment of the requirements for the degree of

Doctor of Philosophy in Planetary Science

at the

MASSACHUSETTS INSTITUTE OF TECHNOLOGY

June 1995

© 1995 Massachusetts Institute of Technology

All rights reserved.

Author_____

Department of Earth, Atmospheric, and Planetary Sciences
7 October 1994

Certified by_____

Professor Timothy E. Dowling
Thesis Advisor

Accepted by_____

Professor Thomas H. Jordan
Department Head

**Planetary Infrared Observations:
the Occultation of 28 Sagittarii by Saturn and
the Dynamics of Jupiter's Atmosphere**

by

Joseph Harrington

Submitted to the
Department of Earth, Atmospheric, and Planetary Sciences
on 7 October 1994 in partial fulfillment of the
requirements for the degree of
Doctor of Philosophy in Planetary Science

Abstract

The thesis consists of three parts. Part I reports an imaging observation of the occultation of 28 Sgr by Saturn and its rings, including a map of ring optical depth at 5-km resolution, ring event timings accurate to ~ 0.05 sec (~ 1 km in the ring plane), ring masses, and observation of material both in the deepest part of the B ring and exterior to the F ring. Part II reports imaging observations of Jupiter's tropospheric cloud opacities at a wavelength of $4.9\text{ }\mu\text{m}$. Power spectrum analysis reveals an inertial enstrophy cascade between planetary wavenumbers ~ 25 and ~ 50 . The power law exponent that best fits the cascade is -3.09 ± 0.13 , close to the theoretical value of -3 . The power law indicates that there is no significant energy input in Jupiter's atmosphere in this wavenumber range, implying that baroclinic instability may not be important on Jupiter. The spectra show no slowly-moving planetary-scale waves. This is despite the detection by others of such features in images sensitive to the stratosphere. These data have ten times the spatial resolution and twice the temporal resolution of a prior null wave search at this wavelength. The question of how the thermal features are connected to the rotation rate of the interior remains open. Appendices describe new techniques for automated image mosaic assembly and planetary limb identification. Part III presents models of the impact of comet P/Shoemaker-Levy 9 on Jupiter that predict observable inertia-gravity waves resulting from the collisions.

Thesis Advisor: Timothy E. Dowling
Title: Professor

Biographical Note

Joseph Harrington was born on 5 January 1967 in Vienna, Austria, to Drs. Joseph and Diethild Harrington. He attended the Westborough, Massachusetts, public schools starting in the fall of 1973 and graduated from Westborough High School in June of 1984. On 27 May 1988, he earned the Bachelor of Science in Physics from the Massachusetts Institute of Technology. In September of 1988, he entered the Planetary Science doctoral program in the Department of Earth, Atmospheric, and Planetary Sciences at MIT. In addition to the academic curriculum, he taught four classes, built and ran the Planetary Science Computing Facility, and observed Jupiter's aurorae at the National Aeronautics and Space Administration's Infrared Telescope Facility with Dr. R. L. Baron and Prof. T. Owen (Institute for Astronomy, University of Hawaii). He has published Part I and Chapter 1 of Part III of this thesis and has collaborated on three other peer-reviewed papers:

- BARON, R., J. E. P. CONNERNEY, T. SATOH, T. OWEN, AND J. HARRINGTON 1994. Variability of Jupiter's H_3^+ Aurorae. Submitted to *Nature*.
- FRENCH, R. G., P. D. NICHOLSON, M. L. COOKE, J. L. ELLIOT, K. MATTHEWS, O. PERKOVIĆ, E. TOLLESTRUP, P. HARVEY, N. J. CHANOVER, M. A. CLARK, E. W. DUNHAM, W. J. FORREST, J. HARRINGTON, J. L. PIPHER, A. BRAHIC, I. GRENIER, F. ROQUES, AND M. ARNDT 1993. Geometry of the Saturn system from the 3 July 1989 occultation of 28 Sgr and Voyager observations. *Icarus* **103**, 163–214.
- HAMMEL, H. B., S. L. LAWSON, J. HARRINGTON, G. W. LOCKWOOD, D. T. THOMPSON, AND C. SWIFT 1992. An Atmospheric Outburst on Neptune from 1986 through 1989. *Icarus* **99**, 363–367.
- HARRINGTON, J., M. L. COOKE, W. J. FORREST, J. L. PIPHER, E. W. DUNHAM, AND J. L. ELLIOT 1993. IRTF Observations of the Occultation of 28 Sgr by Saturn. *Icarus* **103**, 235–252.
- HARRINGTON, J., R. P. LEBEAU, K. A. BACKES, AND T. E. DOWLING 1994. Dynamic response of Jupiter's atmosphere to the impact of comet Shoemaker-Levy 9. *Nature* **368**, 525–527.

Acknowledgments

This work could not have been completed without help from many people. Those who assisted one of its constituent parts are acknowledged near the end of that part. In addition, I thank my advisor, Prof. Timothy Dowling, for his patience and unbending standards, and for giving directions without steering. I also thank my thesis committee, Profs. J. L. Elliot, Richard Binzel, Peter Stone, and Richard French (Wellesley College) for their advice and encouragement, and for taking the time to be on the committee. Prof. Elliot deserves special mention for having advised me as an undergraduate and early graduate student. Dr. Heidi Hammel has encouraged me and lent a sympathetic ear since my undergraduate days as well.

I have received a lot of support from friends too numerous to list, but particularly from my fellow graduate students, housemates, and the wonderful people at pika. Above and beyond the call of duty, Leslie Young and Paul Starkis provided a room for nearly my first month in Hawai'i.

I thank my parents and my brother Rob for their years of support and encouragement. I will always treasure the memory of my grandparents, who each in their way have shown me that one who achieves much can and should remain humble and compassionate. Their lives will always be examples to me.

Notes About Style

Part I was published in *Icarus* and Chapter 1 of Part III was published in *Nature*. These sections appear here as close to their published form as allowed by the MIT thesis specifications, with changes to ensure that no two tables, figures, or formulae in the entire document have the same number and to correct typesetting errors of fact. To minimize the effect of the journals' different styles while maintaining the integrity of the published works, the unpublished part of the document follows the style of *Icarus*, isolating the differences to a single chapter. Further, the References section of Part III includes all the references of the *Nature* paper in the more familiar *Icarus* format, which has paper titles. The main text of Part II is in preparation for submission to *Icarus* but its appendices are not. The appendices therefore appear after the end matter of the main text (unlike the appendix of Part I, which appears in its published location).

Contents

| | | |
|------------|--------------------------------------------------------------------------------------------|------------|
| I | IRTF Observations of the Occultation of 28 Sgr by Saturn | 17 |
| 1 | INTRODUCTION | 21 |
| 2 | OBSERVATIONS | 25 |
| 3 | TIMING SYSTEM | 29 |
| 4 | DATA REDUCTION | 35 |
| 5 | RING EVENT TIMES | 41 |
| 6 | OPTICAL DEPTH PROFILE MORPHOLOGY | 47 |
| 7 | RING MASSES | 57 |
| 8 | CONCLUSIONS | 63 |
| A | APPENDIX: IMAGING OBSERVATIONS OF OCCULTATIONS | 65 |
| II | A Power Spectrum Analysis of Jupiter's Tropospheric Thermal Emission | 79 |
| 1 | INTRODUCTION | 83 |
| 2 | OBSERVATIONS | 93 |
| 3 | IMAGE PROCESSING | 97 |
| 4 | SPECTRAL ANALYSIS | 113 |
| 5 | WAVE SEARCH | 129 |
| 6 | CONCLUSIONS | 137 |
| A | NOTES ON OBSERVING TECHNIQUE | 151 |
| B | AUTOMATIC MOSAIC ASSEMBLY | 157 |
| C | AUTOMATICALLY CENTERING THERMAL JUPITER IMAGES | 171 |
| D | FLUID DERIVATIONS FOR OBSERVERS | 175 |
| III | Predictions for the Impact of Comet P/Shoemaker-Levy 9 on Jupiter | 189 |
| 1 | Dynamic response of Jupiter's atmosphere to the impact of comet Shoemaker-Levy 9 | 191 |
| 2 | PREDICTION DETAILS AND LIMITATIONS | 203 |
| 3 | CONCLUSIONS | 217 |

List of Figures

| | | |
|-------|--------------------------------------------------------------|-----|
| I.1 | IRTF Occultation Geometry | 23 |
| I.2 | Photometry Apertures and Filter Comparison | 39 |
| I.3 | Ring Profiles | 48 |
| I.4 | Profile Comparisons | 53 |
| I.5 | New Feature | 55 |
| II.1 | 4.9- μ m Jupiter Mosaic of 22 March 1992 | 102 |
| II.2 | Zonal Mean Image Intensity | 103 |
| II.3 | 4.9- μ m Jupiter Maps and Transform Amplitudes | 104 |
| II.4 | Kinetic Energy and Cloud Intensity Spectra | 114 |
| II.5 | Zonal and Meridional Power Spectra | 119 |
| II.6 | Scales that Affect the Spectra | 125 |
| II.7 | Errors in Zonal FFT Phase Fits | 132 |
| II.8 | RMS Transform Amplitude Fluctuation | 134 |
| II.9 | Wave Observability Limit | 135 |
| II.10 | Mosaic Overspecification Example | 159 |
| II.11 | Thermal Jupiter Mosaic Pieces | 162 |
| II.12 | Correlation Diagram | 164 |
| II.13 | Correlation Images | 166 |
| II.14 | Thermal Jupiter Final Mosaic | 170 |
| II.15 | Infrared and Visible-Light Images of Jupiter | 172 |
| II.16 | Calculating Images for Centering | 174 |
| II.17 | Potential Vorticity Example | 177 |
| III.1 | Zonal temperature deviation profiles | 195 |
| III.2 | Model of comet impact | 198 |
| III.3 | 1,197-mbar Model Profiles for 6 Days | 209 |

List of Tables

| | | |
|---------|----------------------------------------------------------|-----|
| I.I | 1989 July 3 Occultation Parameters | 26 |
| I.II | Ring Event Times | 43 |
| I.III | Ring Masses and Mean Optical Depths | 61 |
| II.I | Synopsis of Data and Observations | 94 |
| II.II | Linear Fits to Regions of the Spectra | 118 |
| III.1 | Ranges of zonal temperature deviation profiles | 199 |
| III.II | Impactor Sizes for Various Energies | 204 |
| III.III | Sizes and Temperatures of Heating Discs | 208 |

Part I

IRTF Observations of the Occultation of 28 Sgr by Saturn

IRTF Observations of the Occultation of 28 Sgr by Saturn

JOSEPH HARRINGTON,^{*,1,2} MAREN L. COOKE,^{*} WILLIAM J. FORREST,^{‡,2}
JUDITH L. PIPHER,^{‡,2} EDWARD W. DUNHAM,^{*,3} AND J. L. ELLIOT^{*,†}

^{}Department of Earth, Atmospheric, and Planetary Sciences
Room 54-410
Massachusetts Institute of Technology
Cambridge, Massachusetts 02139*

*[†]Department of Physics
Massachusetts Institute of Technology
Cambridge, Massachusetts 02139*

*[‡]Department of Physics and Astronomy
University of Rochester
Rochester, New York 14627*

Received November 4, 1992; revised March 24, 1993.

¹To whom correspondence should be addressed.

²Visiting Astronomer at the Infrared Telescope Facility, which is operated by the University of Hawaii under contract from the National Aeronautics and Space Administration.

³Present Address:
MS 245-6
NASA Ames Research Center
Moffett Field, California 94035

Publication reference:

HARRINGTON, J., M. L. COOKE, W. J. FORREST, J. L. PIPHER, E. W. DUNHAM, AND J. L. ELLIOT 1993. IRTF Observations of the Occultation of 28 Sgr by Saturn. *Icarus* **103**, 235–252.

© 1993 Academic Press, Inc. Reprinted by permission.

We obtained an infrared-imaging time series ($\lambda=3.255\ \mu\text{m}$, $\Delta t = 0.25\ \text{sec}$) of the 1989 July 3 occultation of 28 Sgr by Saturn and its rings using the NASA Infrared Telescope Facility (Mauna Kea, HI) and the University of Rochester 62×58 -pixel InSb array camera. The radial extent of the beam in the ring plane was $\sim 20\ \text{km}$, and the rings were sampled approximately every 5 km. The images show stellar signal throughout the ring event, including the densest parts of the B ring, although some signal may be due to indirect light diffracted into the beam (P. D. Nicholson, O. Perković, K. Matthews, and R. G. French 1991, *Bull. Am. Astron. Soc.* **23**, 1178). The time associated with each pixel readout is accurate to within 60 μsec of UTC. We present a table of interpolated ring event times.

Although qualitative ring structure at scales of 10–100 km is consistent with the Voyager stellar and radio occultation profiles, our profile varies systematically with respect to the Voyager data over large radius scales. The most likely explanation for this is indirect stellar signal diffracted through the rings; to date there is no quantitative model of this effect, and the ring masses derived here have not been corrected for it.

The projected stellar diameter of $\sim 20\ \text{km}$ put most density- and bending-wave trains below our resolution; fitting models to these waves for surface mass density was therefore not attempted. The Voyager Photopolarimeter Subsystem occultation data do not suffer such smearing, so the mass extinction coefficient determined by L. W. Esposito, M. O’Callaghan, and R. A. West (1983, *Icarus* **56**, 439–452) was used to estimate the mass of the rings, based on the 1989 July 3 data. The masses derived in this fashion are $(2.42 \pm 0.93) \times 10^{22}\ \text{g}$ (total), $(0.097 \pm 0.037) \times 10^{22}\ \text{g}$ (C ring), $(1.84 \pm 0.71) \times 10^{22}\ \text{g}$ (B ring), and $(0.49 \pm 0.19) \times 10^{22}\ \text{g}$ (Cassini division and A ring). We present masses and mean optical depths of individual ring sections.

Chapter 1

INTRODUCTION

On 1989 July 3, Saturn, its rings, and Titan occulted 28 Sgr, a K4 giant star with magnitudes: $K = 1.50 \pm 0.04$, $I = 3.90 \pm 0.06$ (Neugebauer and Leighton 1969), and $V = 5.388 \pm 0.011$ (Sinachopoulos 1989). Considering only photon statistics, this event had the highest signal-to-noise ratio of any occultation by Saturn observed since the advent of modern detectors, and it was the first occultation by Saturn's rings where stellar signal was detectable throughout the entire event. Taylor (1983) first predicted the occultation, and it was also discussed by Killian and Dalton (1985).

The star's sampling beam at Saturn's distance spans ~ 20 km, so features much smaller than 20 km are not readily discernible from this occultation. The angle between the beam and the ring plane was $25^\circ 24' 14''$, but fortunately the occultation path ran roughly in the direction of the minor axis of the projected beam ellipse (see Fig. I.1). Although Sinachopoulos (1989) reports the star as double, the companion

is located $12''.9$ away and has a V magnitude of 13.5; we did not detect this star in the short exposures used during the occultation.

Most major telescopes in the viewing area recorded the event (Brahic *et al.* 1989, di Cicco and Robinson 1989, Dunham *et al.* 1989, French *et al.* 1989, Harrington *et al.* 1989, Hubbard *et al.* 1989, Porco *et al.* 1989, Reitsema *et al.* 1989, and Sicardy *et al.* 1989). Many observers worked in the infrared, both to maximize stellar signal and to minimize reflected light from the planet and rings. They chose absorption bands of molecular species in Saturn's atmosphere (CH_4) and (for those sites with sufficiently dry skies) rings (H_2O) to reduce reflected light still further.

Several observers used imaging detectors. These systems have the advantages that the photometric aperture can be placed on the image after the fact, substantially reducing noise introduced by tracking errors; the background light field can be fitted and removed far more accurately than is possible with single-channel photometers, providing higher quality data and allowing observation of fainter stars; and the images themselves can be inspected if anomalies are found in the lightcurve or to identify events of spatial significance, such as the location of a central flash. However, imaging photometers generate copious quantities of data, making data storage and analysis more difficult. In addition, few of these systems are capable of operation at high speed or with accurate synchronization to an external time signal.

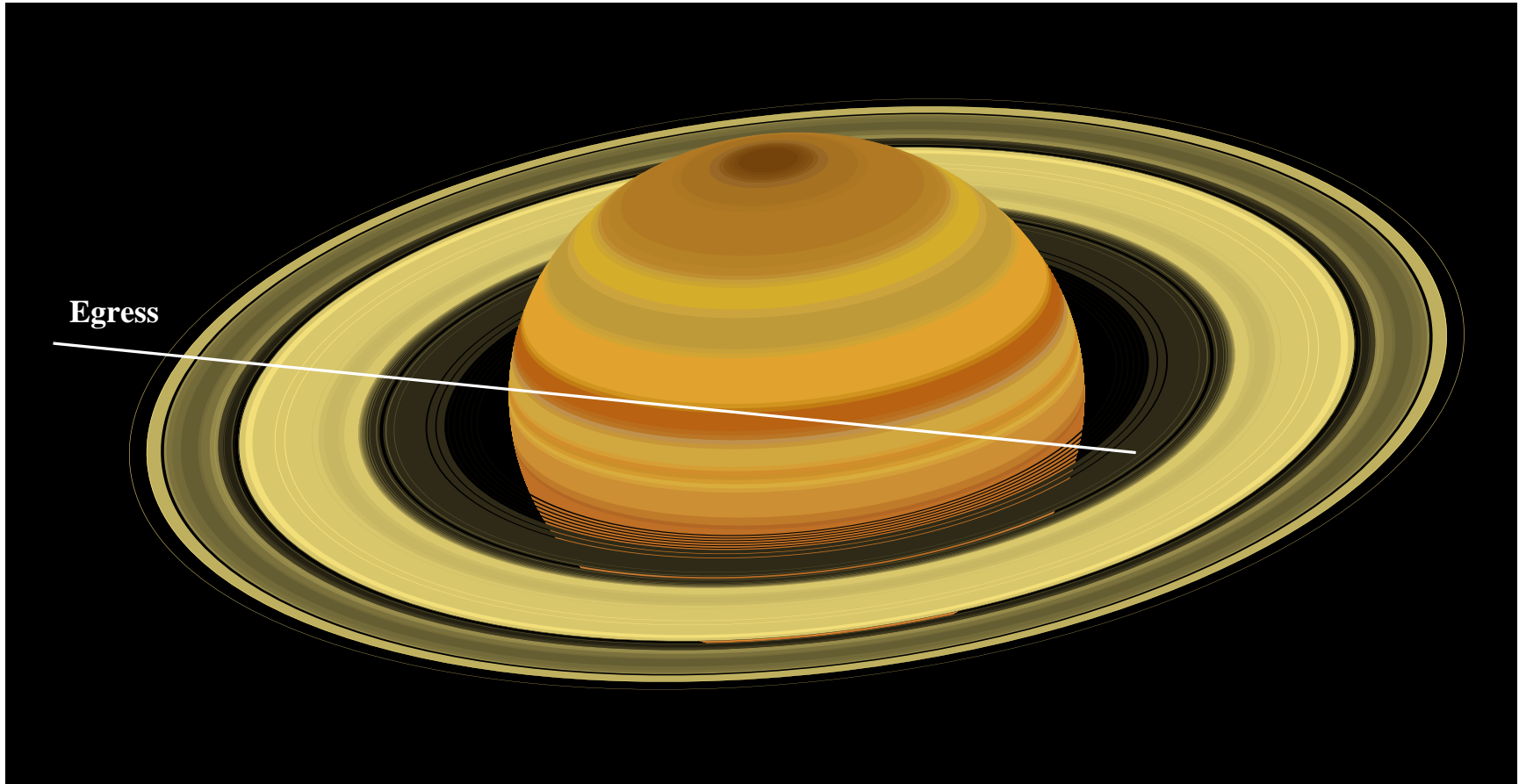


Fig. I.1. Event geometry for the occultation as viewed from the IRTF. The white line is the path of the star as we recorded data.

We present here our observations of the event with the NASA Infrared Telescope Facility (IRTF) and the University of Rochester IR array camera, our method for generating optical depth profiles, and our first ring results. These results include ring feature times, a discussion of ring profile morphology, and ring mass estimates. We discuss the challenges associated with imaging observations of occultations, and our approaches to them, in the appendix.

Chapter 2

OBSERVATIONS

We obtained a time series of 44,408 infrared images of the 28 Sgr occultation with the University of Rochester 62×58 -pixel InSb array camera (Forrest *et al.* 1989) at the IRTF on Mauna Kea, Hawaii. We achieved absolute timing by running the camera’s computer directly from an accurate clock (see Timing System, below). Event and observational parameters are summarized in Table I.I.

The filter wavelength is in a water ice absorption band and inside the edge of a methane absorption band (see Table I.I). This minimized background light from the rings and planet, respectively, simplifying image processing. We were fortunate to have had a clear night, with occasional patchy cirrus clouds on the horizon but none seen overhead; the hygrometer read 0% relative humidity as we started taking data. Despite careful monitoring of temperature, the signal level of the star in unocculted regions rose smoothly in time throughout the event. We believe that a small amount

of moisture may have condensed on the dewar window prior to the occultation and slowly evaporated. We corrected for this effect in the analysis.

TABLE I.I
1989 July 3 Occultation Parameters

| | |
|-------------------------|------------------------------------------------------------------|
| Telescope | 3.0-m NASA Infrared Telescope Facility |
| Site | Mauna Kea, Hawaii |
| Star | 28 Sgr = SAO 187255, HD 173469, BD -22°4854, HR 7046 |
| Spectral type | K4 III (Neugebauer and Leighton 1969) |
| V Magnitude | = 5.388 ± 0.011 (Sinachopoulos 1989) |
| K Magnitude | = 1.5 ± 0.04 (Neugebauer and Leighton 1969) |
| Sky-plane beam diameter | ~ 20 km |
| Radial beam velocity | ~ 20 km/sec |
| Beam-ring plane angle | $25^{\circ}24'14''$ |
| Camera | U. of Rochester 62×58 -pixel InSb array |
| Stored frame size | 62×12 pixels |
| Pixel scale | $0''.42/\text{pixel}$ |
| λ_0 | = $3.255 \mu\text{m}$ (methane and water ice absorption) |
| $\Delta\lambda$ | = $0.230 \mu\text{m}$ |
| Exposure time | 0.25 sec (3 averaged $\frac{1}{12}$ sec exps) |
| Timing system accuracy | $\pm 60 \mu\text{sec}$ per pixel, ± 1 ms per frame, absolute |
| Data start | 6:46:00 UTC (C ring during ingress) |
| Data end | 9:51:00 UTC (well outside F ring) |

The unocculted star was bright enough to saturate the detector in less than $\frac{1}{4}$ sec. In addition, data storage capacity was limited to 80 Mbytes, due to constraints in the camera computer. To reduce the quantity of data to a manageable amount, avoid image saturation, and still comfortably oversample the lightcurve as smoothed by the star's projected diameter, we recorded just twelve rows (rows 6–17, chosen for their cosmetic quality), exposed for $\frac{1}{12}$ second, and averaged three successive exposures to generate each recorded image.

One of the diagonal mirrors in the camera was apparently damaged in shipment and had to be replaced by a slightly smaller one. The 12 lowest-numbered columns were thus vignetted, causing this region to lose celestial signal and to be illuminated by thermal radiation from the diagonal mirror's support structure. Background and flat frame correction did not completely remove these effects, so we ignored these columns in the analysis. Unfortunately, the star reappeared from planet occultation in this area, so we have been unable to produce a reliable atmospheric emission lightcurve.

Because of problems with the telescope control system, we acquired Saturn well into ring ingress. We took several full-frame bias, flat-field, sky, and planet images before and after the event (see Data Reduction, below). Data recording began at 6:46:00 UTC and ran continuously until 9:51:00 UTC. We nodded the telescope south $9''$ at 7:46:24 and back to the base position at 8:00:00, but did not observe a central flash.

Chapter 3

TIMING SYSTEM

Occultation work requires precise timing; our ~ 20 -km/sec projected stellar velocity would produce a detectable 1-km shift in sharp ring-edge features if the timing were to drift by just 0.05 sec. Further, if a dataset is included in an astrometric solution involving more than one observation, accurate synchronization to a common time base is necessary to eliminate an unknown time shift as a degree of freedom per observatory in the fit (French *et al.* 1993).

Our timing system used a portable quartz occultation clock (Baron 1989) to drive the camera's computer directly. This clock has a frequency accuracy of approximately 10^{-9} (maximum drift over time Δt of $10^{-9} \Delta t$). There were two independent checks in the system: the IRTF's Geostationary Operational Environmental Satellites (GOES) receiver and a portable rubidium standard borrowed from the National Institute of Standards and Technology's WWVH station at Barking Sands, Kauai, Hawaii. These

three time sources are hereafter referred to as the MIT clock, the GOES receiver, and the Rb clock, respectively. The GOES receiver is a Kinometrics Model 468-DC GOES Satellite Synchronized Clock, nominally accurate to within 1 ms of UTC, though satellite motions are not taken into account. The Rb clock's nominal accuracy is 10^{-12} .

On 1989 July 1 at 00:07 UTC, the Rb clock's frequency was adjusted to match that of the primary time standard at WWVH and brought to Mauna Kea (the Rb clock was also synchronized to the primary, but lost synchronization on the way to Mauna Kea). The MIT clock's frequency was tuned to match the Rb clock's and it was synchronized to the GOES receiver for an approximation of the correct time. The MIT clock fed a 20-Hz signal to a phase-locked loop (PLL) circuit which generated a 60-Hz signal. This 60-Hz signal was passed to the bus interrupt line of the Rochester camera's computer.

Computers synchronize data transfers between their various components with bus interrupt signals; in the case of the Rochester camera's computer these occur 60 times each second. Interrupt service routines (ISR's) in the computer's real-time operating system run immediately upon receipt of an interrupt and generate a request-for-data (RFD) signal on the bus. The RFD is sensed by the infrared array and triggers a frame readout/clear operation if one is scheduled. The readout/clear operation sequentially resets each pair of pixels by reading their accumulated charge through a pair of amplifiers. Since there is no shutter, the chip is sensitive to light even as it

is being read. This essentially eliminates dead time between integrations, but causes the beginning and end of an integration interval to vary across the detector (the duration of integration remains constant). For this dataset, the time associated with each frame is the mid-time of integration at the location of the center of the stellar image.

The time of each pixel readout relative to the MIT clock is thus known to an accuracy dependent upon the variation in the lengths of ISR's and upon the stability of the PLL. Together these uncertainties are less than 60 μsec , and since they dominate the uncertainty and drift due to the MIT clock, absolute timing accuracy for any given pixel is also 60 μsec . Each pixel pair takes 36 μsec to read out, so the read time per row is 1.116 msec. The star's position was constant to within ± 1 pixel, and we did not compensate for stellar image motion in the timing solution, so the time associated with each frame is within ~ 1 ms of UTC.

During the event, we used the offset counter in the MIT clock to measure the differences between all time sources with a resolution of 200 nsec. We also watched diagnostic 1-Hz signals from all sources on an oscilloscope, and ran a strip chart which recorded the 1-Hz signal from the MIT clock and the exclusive-OR of this signal and a 1-Hz signal generated by the computer. During the event, the total drift between the MIT and Rb clocks was 200 nsec. The GOES receiver drifted 694.4 μsec between 4:45:00 and 9:56:00 UTC, which the WWV office in Boulder, Colorado, has attributed to satellite motions.

The PLL lost lock 42 times during the event, oscillating in frequency for a few seconds until it regained its lock. In each of these events, three extra interrupts occurred (in one case, two extra interrupts occurred). The oscillation left an obvious signature in the data, and the additional interrupts caused the waveform recorded on the strip chart to change. In the analysis, we identified each event and corrected for the resultant discrete timing error. Up to 35 images after each event were marked as “bad” to eliminate the possibility of residual effects contaminating the analysis (these are the small gaps in Fig. I.3, for example at 85,000 km).

We returned the Rb clock to the WWVH station, where the staff measured its offset and frequency relative to the primary time standard on 1989 July 3 at 23:30 UTC. This offset agreed with the offset relative to the GOES receiver during the event to within the GOES receiver’s accuracy. The WWVH staff found the Rb clock’s time to be drifting less than 100 ns/day. Our timing calculations used the Rb clock’s offsets relative to the primary and the MIT clock, rather than the GOES receiver’s offset relative to the MIT clock, because the GOES receiver is inherently much less accurate.

Since the MIT clock ran the computer directly, each frame readout represents a timing signal from a calibrated, stable time source placed directly into the data. This electronic, directly causal means of associating times with data frames avoids the timing uncertainties inherent in mechanical means such as chopping with the secondary mirror, and obviates the need to model the behavior of a computer’s clock

with respect to an accurate one when associating times with data points.

Chapter 4

DATA REDUCTION

Several corrections must be made to an astronomical array image before the numerical value of each pixel is proportional to the intensity of light from the corresponding area of the sky. These corrections eliminate the most pronounced electronic and atmospheric effects. Bias is the electronic “zero” of the array’s readout amplifier, and must be subtracted from each pixel value so that zero in the data corresponds to zero light level. Pixel-to-pixel variations in sensitivity are removed from the image by dividing by a normalized flat field frame, which is an image of a uniformly lit source. These and other basic corrections are described in more detail elsewhere (e.g., Conner 1984). In the infrared, the thermal emission of the sky is often subtracted, and for bright subjects there is usually a correction for nonlinear chip response to differing light levels.

For ease of handling, the data were broken into six sequential computer files of

occultation images, plus individual error-correction frames taken before and after the event. Bias frames were consistent before and after the event, so we averaged them to generate the frame used to process the images. The sky frames varied significantly between the pre- and post-occultation sets, so the members of each set were averaged to produce a representative frame. We then generated six new sky frames by interpolating each pixel to the mid-time of each of the six data files. The flat field was made from images of the unfocussed inside of the observatory dome and similar images of the sky to eliminate thermal contributions from the telescope itself.

The Santa Barbara Research Center 62×58 -pixel InSb array chips are known to have a nonlinear response to light. This effect is primarily caused by the increase in capacitance of each photodiode as the back bias decreases during an exposure (Forrest *et al.* 1989). The linearization function appropriate to this dataset is given by

$$\text{lin}(A) = Ae^{A/192,000}, \quad (\text{I.1})$$

where A is measured signal in analog-to-digital conversion units (ADU) and $\text{lin}(A)$ is linearized signal. One ADU corresponds to approximately 60 electrons. The functional form above was calibrated empirically by observing the signal from a flat-field source of constant flux f with varying integration times Δt . The logarithmic derivative for all pixels was fit adequately over a range of A easily containing the extremes in our data by

$$\frac{d \ln(f \Delta t)}{d \ln(A)} = 1 + mA, \quad (\text{I.2})$$

which integrates to the linearization function.

The total image correction is

$$F = \ln(F_{dome} - B) - \ln(F_{sky} - B), \quad (\text{I.3})$$

$$C = \frac{\langle F \rangle}{F} (\ln(R - B) - \ln(S - B)), \quad (\text{I.4})$$

where F is a pixel value in the corrected flat-field image, F_{dome} , F_{sky} , and B are the corresponding pixels in the averaged dome flat, sky flat, and bias images, respectively, C is a pixel value in the corrected image, R and S are the corresponding pixels in the raw data and interpolated sky images, respectively, and $\langle F \rangle$ is the mean pixel value of the flat field.

To determine the star signal above the ring background, we used the Aperture Photometry Package (Davis 1987) of the Image Reduction and Analysis Facility (IRAF) (Tody 1986). This software measures signal falling on an arbitrary aperture centered on the star (the “raw” region) and on a surrounding “background” region. In our case, the background region includes light from the sky as well as some light from the ring and planet. The raw region contains light from the star in addition to these sources; subtracting the area-weighted background signal from the raw signal gave the “star” value for each frame.

We used two different arrangements of apertures (see Fig. I.2). For most of the images, the raw region was oblong, 14 pixels wide and 12 high with semicircular ends; the background region was a circle of 10 pixels' radius, truncated at the edges of the frame and excluding the raw region. The oblong shape was chosen to compensate for small tracking errors in the long dimension of the recorded image. We took advantage of the star's relative faintness in the optically thick B ring and our good fortune in guiding during this segment of the occultation and used a smaller, circular raw aperture for images in the B ring. This aperture, 5 pixels in radius, was immediately surrounded by a background annulus 8 pixels in radius and truncated at the edges of the image. The photometry regions used outside of the B ring were defined by polygons which were evaluated every 0.5 pixels ($0''.21$); the circular B-ring apertures use the correct proportion of each pixel which intersects a circular border. Because of the tight tolerances of the image width, the polygonal apertures had a constant center in each data file, and the B-ring aperture centers were constant through the ring. The resulting lightcurve does not show the shifts in star values at borders of adjacent data files that would correspond to the abrupt shift from one sky frame to the next. This is an indication that the per-frame background subtraction was effective.

The signal level of the unocculted star increased fairly smoothly throughout the event, as mentioned under Observations. A linear function of time fit considerably better than an atmospheric extinction curve. We thus fit a line to signal levels in three unocculted regions, each an average of 201 consecutive star values. These values

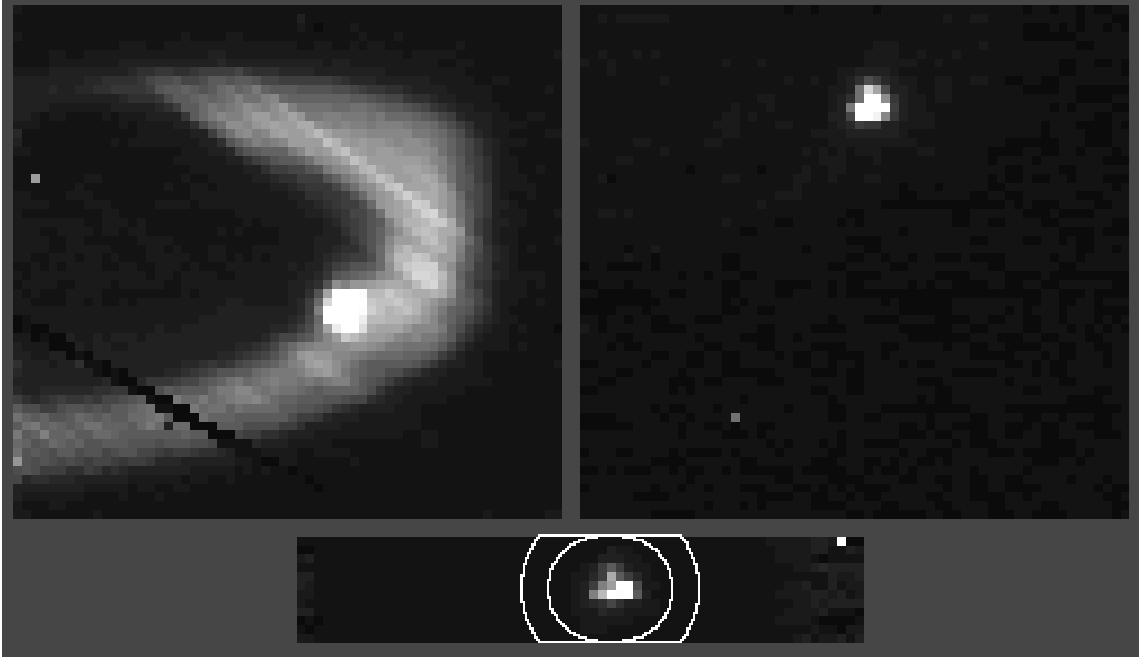


Fig. I.2. The upper left image shows Saturn, the rings, and 28 Sgr viewed through a K filter just prior to the beginning of the occultation. The planet appears very dark because of absorption by atmospheric methane at this wavelength. The image in the upper right shows the scene in our occultation filter ($\lambda=3.255 \mu\text{m}$, $\Delta\lambda=0.230 \mu\text{m}$), with the star on the region of the chip (rows 6 – 17 from the top of the image) recorded during the event. Absorption by water ice in the rings as well as by atmospheric methane reduces the reflected sunlight to a very faint background. In both images, the background away from Saturn is approximately the same. The peak pixel values of the star are 12,365 ADU at K and 17,843 ADU in the occultation filter. These images are shown with the same linear brightness scale. The bottom image shows the first frame of the recorded occultation data, marked with the polygonal photometry apertures used in the A and C rings. The inner region is wider than it is high to deal with small tracking errors which occurred in the long dimension of the array (E–W). Within each file of images (total of six files), the center of the aperture is the same. We used a five-pixel circular aperture in the B ring to take advantage of better tracking and the fainter star. The three pixels in the upper right corner are the encoded time and array temperature, present in each occultation image, which provided a useful diagnostic during the analysis.

were taken from the clear region between the planet and the rings (both ingress and egress) and from a region well outside the F ring after egress. In all three cases we were careful to avoid the flux enhancement near the rings (see Optical Depth Profile Morphology, below). We calculated normal optical depths according to the formula

$$\tau_n = -\ln\left(\frac{I}{I_0}\right) \sin(\theta) \quad (\text{I.5})$$

where τ_n is normal optical depth, I is stellar intensity, I_0 is unocculted stellar intensity (obtained from the linear fit to this value in clear regions during the occultation), and θ is the beam incidence angle of $25^\circ 24' 14''$ on the ring plane. The standard deviation of I/I_0 (0.25 sec integrations) in the three regions used to fit the I_0 line was 1.7, 1.5, and 1.0% of the transmission, respectively.

Finally, we tagged the lightcurve with ring-plane radii consistent to within a few kilometers of the Voyager radii for presumed-circular features. These radii assume the pole of Nicholson *et al.* (1990) and an offset for Saturn's position from the Jet Propulsion Laboratory DE-125 ephemeris of 1655 km east and 438 km south in the sky plane. Figure I.3a, in the section on Optical Depth Profile Morphology, presents the resulting profile for the rings.

Chapter 5

RING EVENT TIMES

In order to measure ring feature times, we interpolated the stellar signal between the 0.25 sec samples of the lightcurve. Event times are presented in Table I.II, along with estimated measurement uncertainties that depend both on the strength of the feature and on the relative noise level in the region. Typical measurement uncertainties are $0.01 - 0.05$ s — generally within a few tenths of a sample. The larger uncertainties accompany features found in optically thick regions, where the transmitted stellar signal is more noisy. Regions having more complex optical depth profiles are also more difficult to measure, as closely-spaced variations limit the interval over which mean signal levels can be characterized.

This set of features is generally inclusive of those used for the pole solution of Nicholson *et al.* (1990), and is more fully described by French *et al.* (1993). Some features that had been assumed circular during earlier work have been found to be non-circular

(or ambiguous) during the French *et al.* orbit fits; Table I.II uses the new designations. Some regions of the B ring that were obscured by high slant optical depths in the Voyager occultation data now permit reliable feature identification. These are included as features 71 – 83 both here and in French *et al.* (1993). Three members of this expanded set are the cores of narrow features and the times given represent their apparent centers, whether a signal peak (feature 51, the irregular F ring, and feature 79, newly identified in the inner B ring) or a minimum (feature 36, in the middle C ring).

The remainder of the features are the sharp edges of gaps, ringlets, or plateaux, and other abrupt optical depth transitions within the rings. These intrinsically sharp edges are smeared, however, by convolution with the large (~ 20 km) stellar diameter, and appear as gradual ramps that are often further contaminated by noise. The event times in Table I.II are the “half-light” times, measured by finding the point halfway between the mean signal on either side of the ramp and linearly interpolating between individual frame exposure times. This method can be uniformly applied to all edges in the sample, despite differences in noise level and surrounding ring characteristics. It is not ideal, since many of the edges are quite sharp and the diffracted intensity at the edge is $\frac{1}{4}$ the unocculted flux, rather than $\frac{1}{2}$. However, 28 Sgr is far from a point source, and as French *et al.* (1993) demonstrate, systematic radius errors for these measurements will be less than 0.1 km.

Our measurements of the features currently presumed circular are incorporated along

with Voyager data and other 28 Sgr observations in the new geometry analyses that are presented by French *et al.* (1993) and Hubbard *et al.* (1993).

TABLE I.II
Ring Event Times

| Feature Number ^a | UTC | Error ^b (sec) | Comment ^c |
|--------------------------------|--------------|-----------------------------|-----------------------|
| 36 | 06:47:08.589 | 0.10 | core |
| 37 | 06:49:14.089 | 0.03 | |
| 38 | 06:49:16.064 | 0.03 | |
| 43 | 06:50:15.002 | 0.02 | Titan Gap o. e. |
| 62 | 06:50:17.214 | 0.02 | Titan ringlet o. e. |
| 63 | 06:50:18.227 | 0.03 | Titan ringlet i. e. |
| 39 | 06:50:49.002 | 0.04 | plateau o. e. |
| 40 | 06:51:29.664 | 0.04 | plateau o. e. |
| 44 | 06:52:50.152 | 0.04 | innermost C ring |
| 44 | 08:41:51.187 | 0.04 | innermost C ring |
| 40 | 08:43:11.247 | 0.02 | plateau o. e. |
| 39 | 08:43:51.857 | 0.03 | plateau o. e. |
| 63 | 08:44:24.127 | 0.01 | Titan ringlet i. e. |
| 62 | 08:44:25.564 | 0.01 | Titan ringlet o. e. |
| 43 | 08:44:26.352 | 0.03 | Titan Gap o. e. |
| 38 | 08:45:24.517 | 0.03 | |
| 37 | 08:45:26.502 | 0.02 | |
| 36 | 08:47:31.484 | 0.05 | core |
| 35 | 08:49:33.364 | 0.02 | plateau i. e. |
| 34 | 08:49:42.339 | 0.05 | plateau o. e. |
| 33 | 08:50:14.314 | 0.02 | |
| 42 | 08:50:18.744 | 0.02 | |
| 31 | 08:50:26.129 | 0.05 | |
| 30 | 08:50:46.277 | 0.01 | plateau i. e. |
| 29 | 08:50:56.627 | 0.02 | plateau o. e. |
| 61 | 08:51:36.052 | 0.02 | Maxwell ringlet i. e. |
| 60 | 08:51:37.977 | 0.02 | Maxwell ringlet o. e. |

TABLE I.II—*Continued*

| Feature Number ^a | UTC | Error ^b (sec) | Comment ^c |
|--------------------------------|--------------|-----------------------------|------------------------------------|
| 28 | 08:52:26.244 | 0.03 | plateau o. e. |
| 59 | 08:52:31.054 | 0.03 | 1.47 R _S ringlet i. e. |
| 58 | 08:52:31.856 | 0.02 | 1.47 R _S ringlet o. e. |
| 27 | 08:52:52.899 | 0.02 | plateau i. e. |
| 41 | 08:52:57.674 | 0.03 | plateau o. e. |
| 26 | 08:53:19.786 | 0.03 | plateau i. e. |
| 25 | 08:53:26.656 | 0.03 | plateau o. e. |
| 57 | 08:53:35.556 | 0.03 | 1.495 R _S ringlet i. e. |
| 56 | 08:53:38.294 | 0.01 | 1.495 R _S ringlet o. e. |
| 24 | 08:53:47.531 | 0.02 | plateau i. e. |
| 23 | 08:53:57.004 | 0.02 | plateau o. e. |
| 22 | 08:54:58.706 | 0.05 | B ring i. e. |
| 83 | 08:56:48.744 | 0.04 | B flat i. e. |
| 82 | 08:57:30.369 | 0.05 | B flat o. e. |
| 81 | 08:58:38.889 | 0.05 | B flatlet i. e. |
| 80 | 08:58:53.031 | 0.05 | B flatlet o. e. |
| 79 | 08:59:10.331 | 0.08 | B flux peak core |
| 78 | 08:59:40.906 | 0.06 | B flux peak i. e. |
| 77 | 09:00:59.231 | 0.06 | B drop |
| 76 | 09:01:43.181 | 0.06 | B flux peak i. e. |
| 75 | 09:02:07.481 | 0.05 | B broad flux peak i. e. |
| 74 | 09:02:16.831 | 0.08 | B broad flux peak o. e. |
| 73 | 09:03:13.131 | 0.05 | B flux peak i. e. |
| 72 | 09:03:42.006 | 0.03 | B flux peak i. e. |
| 71 | 09:04:01.294 | 0.04 | B flux peak o. e. |
| 55 | 09:14:03.499 | 0.02 | B ring o. e., Huygens Gap i. e. |
| 54 | 09:14:16.269 | 0.02 | Huygens ringlet i. e. |
| 53 | 09:14:17.226 | 0.02 | Huygens ringlet o. e. |

TABLE I.II—*Continued*

| Feature Number ^a | UTC | Error ^b (sec) | Comment ^c |
|--------------------------------|--------------|-----------------------------|------------------------------------|
| 20 | 09:14:21.226 | 0.02 | Huygens Gap o. e. |
| 19 | 09:14:32.414 | 0.02 | 1.96 R _S gap i. e. |
| 18 | 09:14:34.729 | 0.03 | 1.96 R _S ringlet i. e. |
| 17 | 09:14:35.894 | 0.03 | 1.96 R _S ringlet o. e. |
| 16 | 09:14:36.881 | 0.03 | 1.96 R _S gap o. e. |
| 13 | 09:14:52.344 | 0.02 | |
| 15 | 09:15:07.461 | 0.03 | |
| 14 | 09:15:55.189 | 0.01 | 1.990 R _S ringlet i. e. |
| 12 | 09:15:56.944 | 0.02 | 1.990 R _S ringlet o. e. |
| 11 | 09:16:04.749 | 0.03 | |
| 10 | 09:16:07.304 | 0.02 | 1.994 R _S gap i. e. |
| 09 | 09:16:07.956 | 0.03 | 1.994 R _S gap o. e. |
| 07 | 09:17:25.331 | 0.05 | A ring i. e. |
| 04 | 09:25:53.806 | 0.01 | Encke Gap i. e. |
| 03 | 09:26:08.119 | 0.01 | Encke Gap o. e. |
| 02 | 09:28:10.719 | 0.02 | Keeler Gap i. e. |
| 01 | 09:28:12.254 | 0.02 | Keeler Gap o. e. |
| 52 | 09:28:23.276 | 0.02 | A ring edge |
| 51 | 09:31:01.946 | 0.05 | F ring core |

^a Feature numbers and precise locations are as reported in Nicholson *et al.* (1990) and modified by French *et al.* (1993); these numbers should not be used without reference to those works.

^b Conservative, by-eye estimate of 2σ error.

^c i. e., inner edge, o. e., outer edge, core, apparent center. Edges are located at the half-light level.

Chapter 6

OPTICAL DEPTH PROFILE MORPHOLOGY

Figure I.3a presents the IRTF egress ring optical depth profile. No attempt has been made to account for extinction efficiency effects due to wavelength or viewing geometry (see below). The small section of C ring data available from ingress is essentially identical to the egress data presented here. There are two major qualitative differences between the infrared profiles from this event and the Voyager data. The first effect is a smearing of fine detail in our data; the second is a systematic variation in optical depth over large radius scales.

Spatial resolution was limited by the projected stellar diameter of ~ 20 km. Most of the numerous density- and bending-wave trains, which were the focus of much of the post-Voyager analysis effort, are unfortunately below this resolution; Fig. I.4 shows three profiles of the Mimas 5:3 density wave. Figure I.4a is the original Voyager Photopolarimeter Subsystem (PPS) profile (Esposito *et al.* 1983a), at a resolution

of 0.5 km. Figure I.4b is the PPS profile at 20-km resolution, showing the loss of all but the first few peaks. The last profile shows the IRTF 28 Sgr data, with even fewer resolved peaks. Likely the most useful wave information to be gained from this dataset will involve determining the phases of those waves whose leading undulations survived the convolution. Both calibrated PPS datasets used in this section were provided by the Rings Node of the Planetary Data System.

On scales slightly larger than this smearing effect, the general qualitative appearances of the profiles match very well, except for the expected differences in location of noncircular features and for the differing phases of the visible portions of density and bending waves. Superposing the profiles as in Fig. I.3c shows that edges line up very well and that the general shapes and widths of ramps and ringlets are similar between the two profiles. The structure of the rings on these scales appears not to have undergone major qualitative changes in the nearly 9 years between the first

Fig. I.3. IRTF egress and Voyager PPS ring occultation optical depth profiles. (a) IRTF 28 Sgr profile. Small structure at 143,000 km is real but could not be a ringlet (see text). No attempt has been made to adjust the optical depths for wavelength-dependent differences in extinction efficiency. (b) PPS profile averaged in flux to 20-km resolution. (c) Superposed IRTF 28 Sgr and PPS 20-km profiles. Detailed features line up well. However, a large-scale difference in optical depths is apparent. In most regions the IRTF data has lower optical depth and is smoother. (d) Difference between IRTF 28 Sgr and PPS 20-km profiles. Large-scale differences are now very apparent, including several regions (e.g., 100,500, 116,000, and 123,000 km) of suppressed optical depth and a ramp from 122,000 km through the outer edge of the A ring. Although the issue is far from resolved, a likely explanation for some of the effects may be indirect signal diffracted into the beam from particles nearby (Nicholson *et al.* 1991). Note noncircular features at, e.g., 77,800 and 140,000 km. Gaps in IRTF profile are due to timing circuit instabilities. Downward spike in PPS profile at 126,700 km has been attributed to instrument error. Axis scales vary as appropriate to each ring. Voyager data courtesy PDS Ring Node.

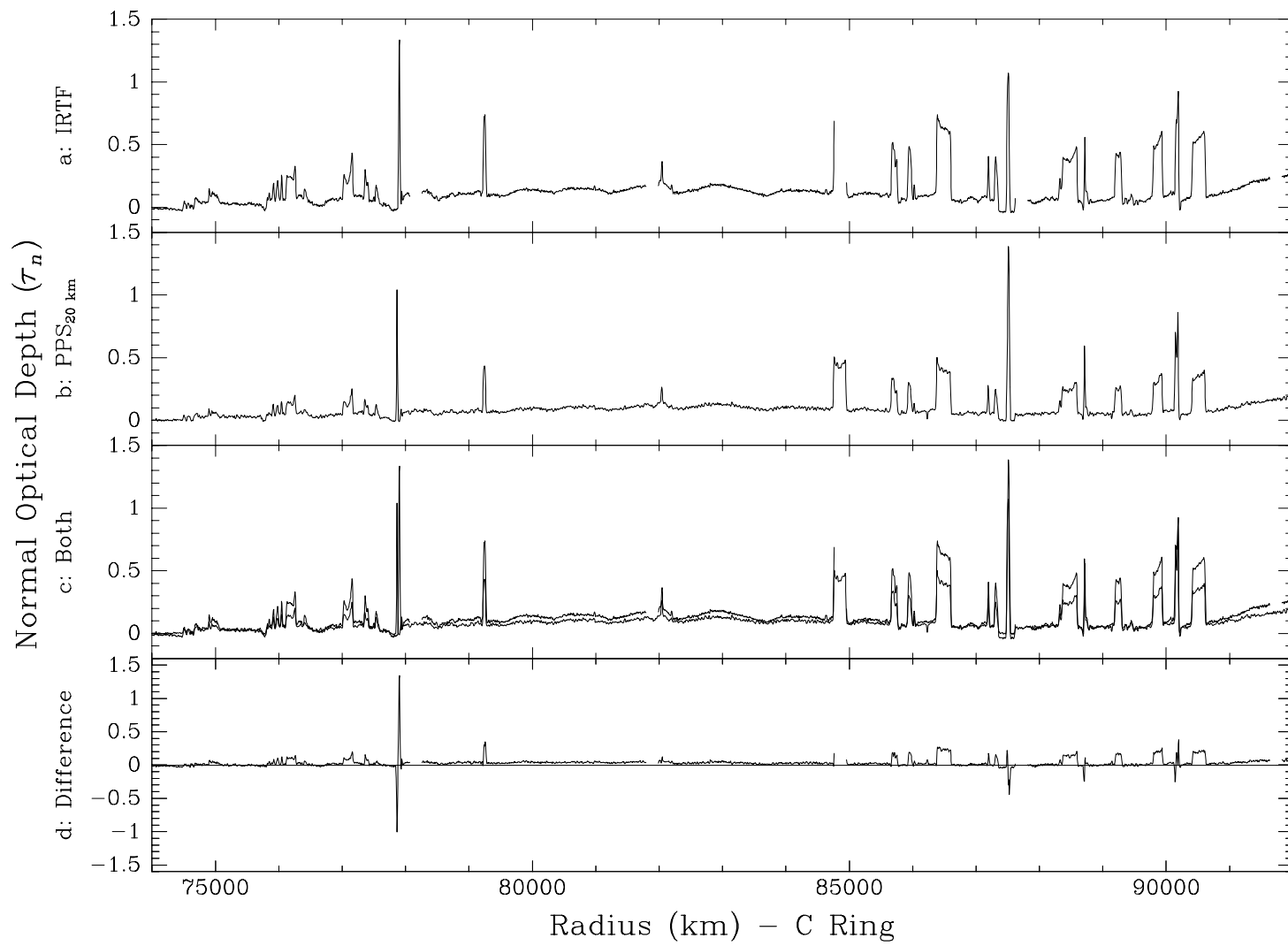


Fig. I.3—Continued

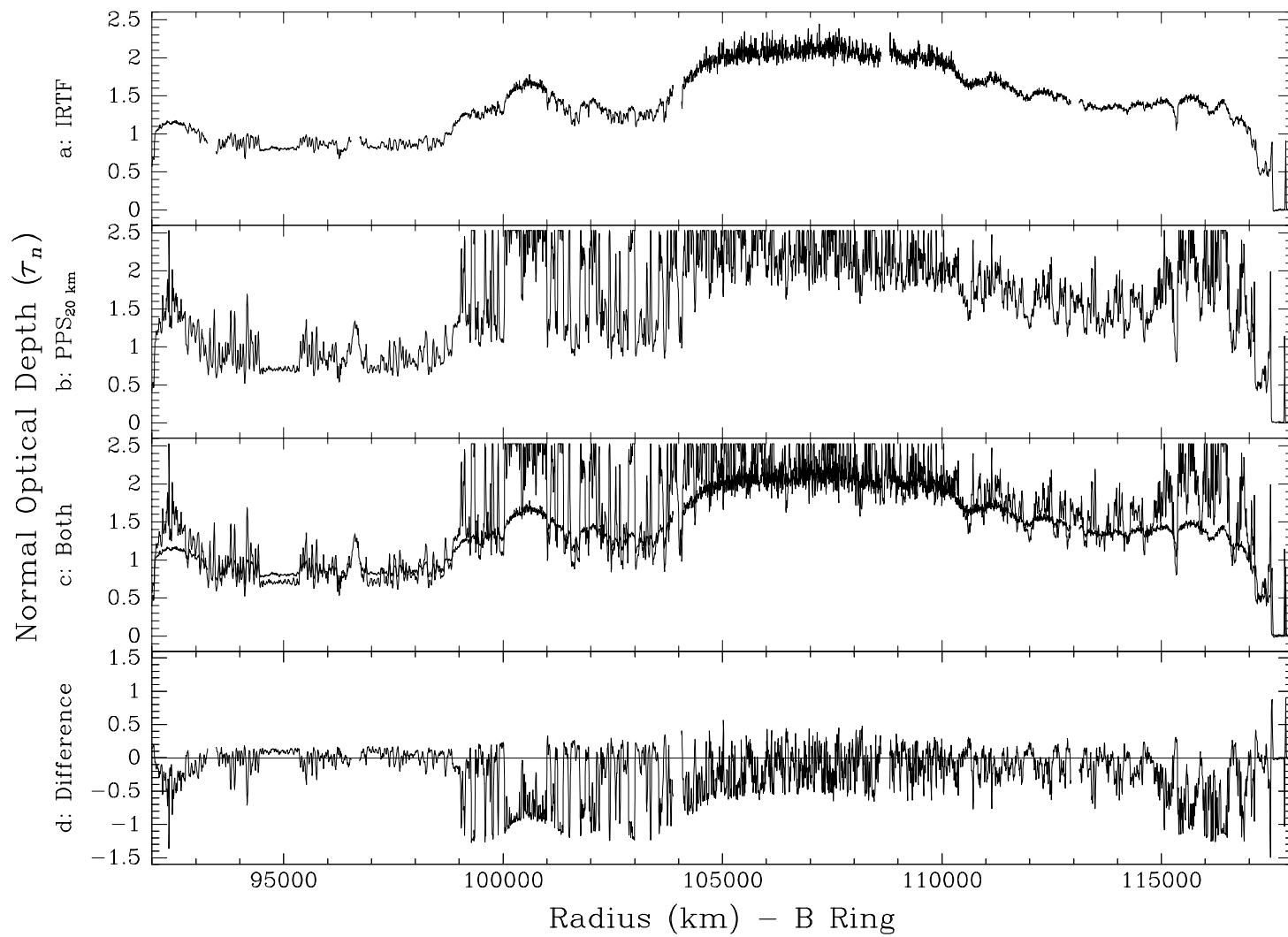


Fig. I.3—Continued

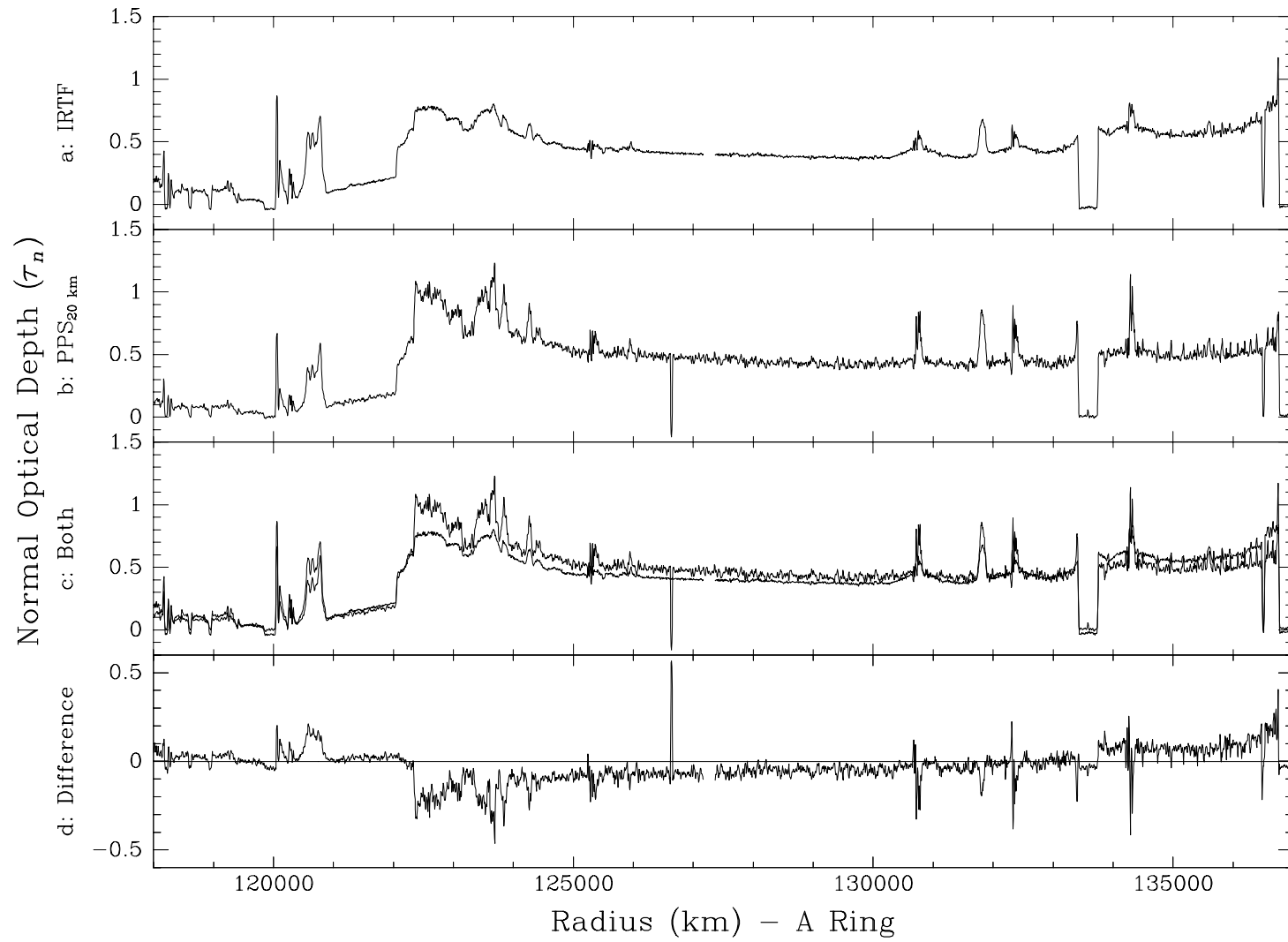


Fig. I.3—*Continued*

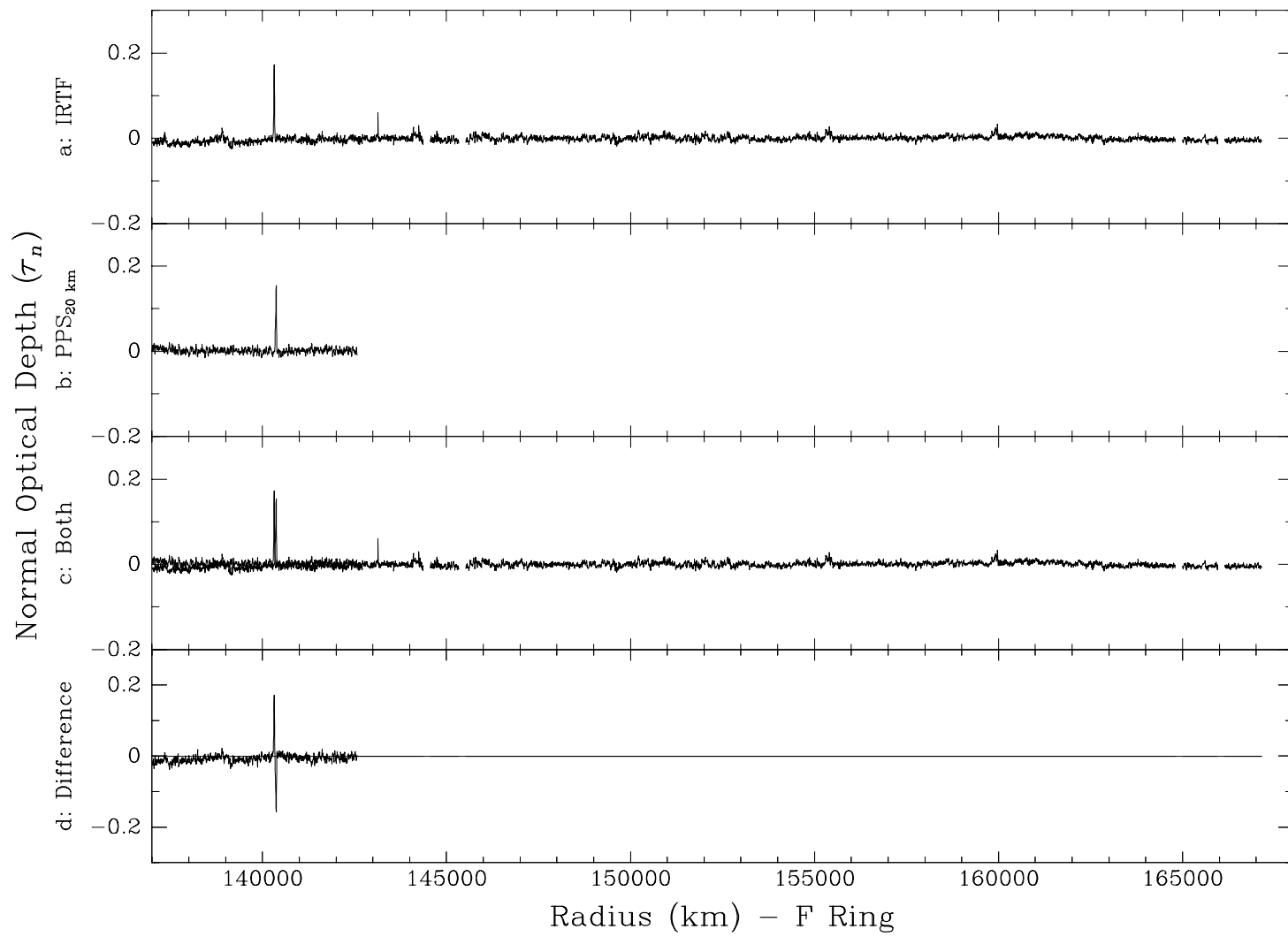


Fig. I.3—*Continued*

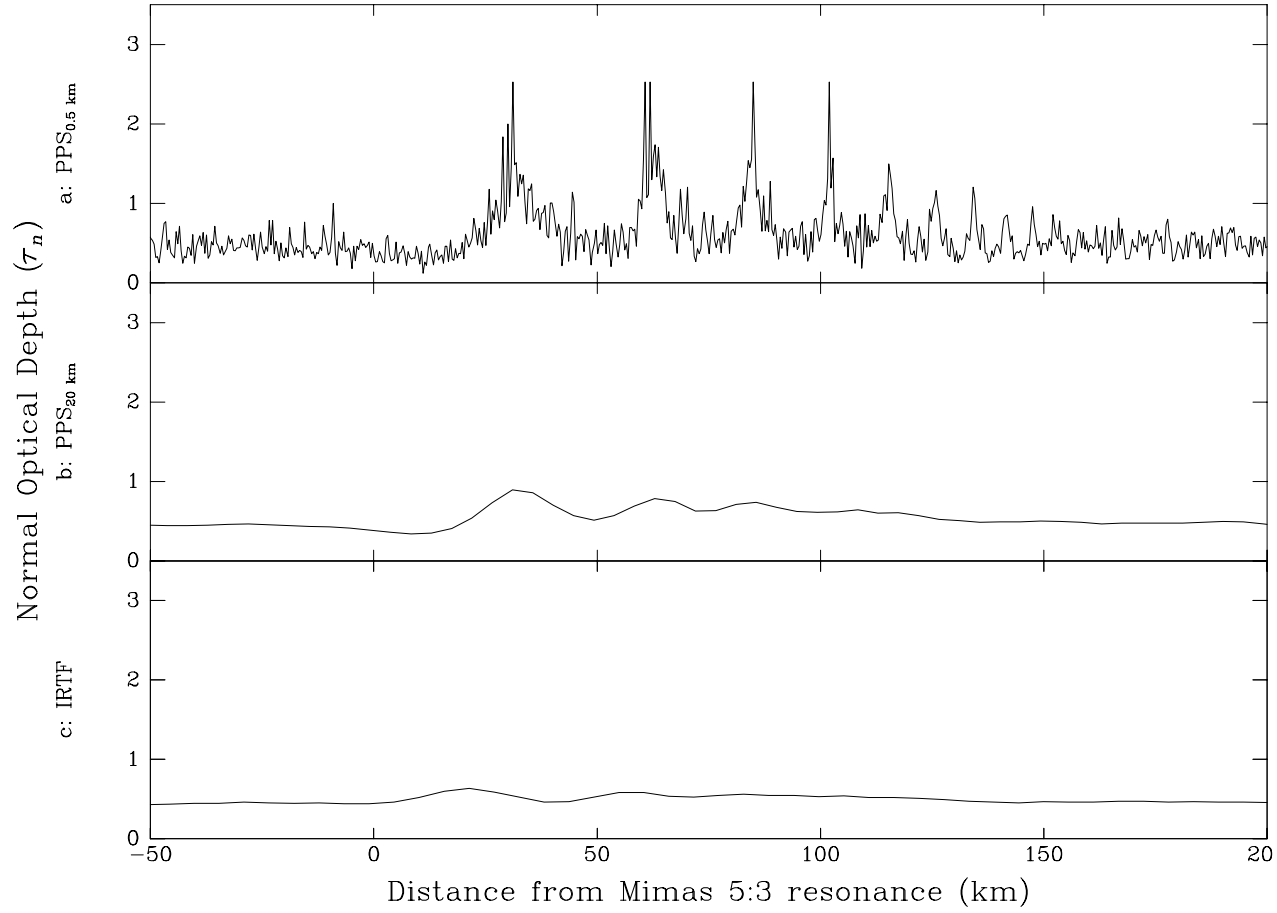


Fig. I.4. Most ring structures narrower than the ~ 20 -km projected stellar diameter were not visible in this event because of convolution with the occultation beam; this included almost all density- and bending-wave trains. Shown here are (a) the Mimas 5:3 density wave in a familiar 0.5-km-resolution version of the Voyager PPS optical depth profile, (b) the same feature in a version of the PPS profile averaged in flux over 20 km, and (c) the feature in the IRTF 28 Sgr occultation data. Voyager data courtesy PDS Ring Node.

Voyager flyby and the 28 Sgr occultation.

When the 20-km PPS and IRTF 28 Sgr profiles are subtracted, as in Fig. I.3d, systematic differences between the PPS and 28 Sgr profiles become more evident. These differences are primarily on scales much larger than those considered above. A fairly regular offset of the two profiles appears in the C ring and a slope is seen in the A ring. In some regions, notably in the B ring adjacent to its edges, the optical depth is reduced considerably compared with the Voyager profile. The most opaque region in the ring, 104,000 – 110,000 km from Saturn’s center, seems “smoothed over,” but the images show signal above the ring background. Immediately outside the ring, the unocculted stellar signal rises by ~ 0.2 optical depths to meet the ring. Nicholson *et al.* (1991) have tentatively associated these effects with indirect light diffracted through the rings and the extinction efficiency of ring particles at infrared wavelengths: the ring particles diffract light with a distribution function that decreases with increasing deflection angle. This produces a faint halo around the bright stellar image. Since the photometry aperture (whose size is determined by the seeing) projects onto a moderately large region of the ring, the integrated light from this halo is enough to affect the profile qualitatively in the densest and clearest areas.

Outside the F ring at 143,141 km from Saturn’s center, a single data frame has an anomalously high optical depth ($\tau_n = 0.06$, transmission = 0.87 of full flux) for the region (see Fig. I.5). The immediately surrounding profile has a full flux of 1.001 ± 0.013 , making this a 10σ feature. The image associated with this point is

normal in all respects. Nowhere else in the data stream does such an anomalous feature appear. We believe the feature is probably real in the sense that it was not due to equipment failure or clouds. However, given its singular nature all we can say for certain is that it is not a ringlet, since our $4\times$ oversampling would cause a ringlet to appear on several consecutive frames. If the event is indeed an occultation by a stray member of the putative F-ring moonlet belt (Cuzzi and Burns 1988), the moonlet would need to block 13% of the beam. If the beam is 20 km in diameter, the corresponding spherical body's diameter would be 7.2 km, which is within the range of 0.1 – 10 km proposed by Cuzzi and Burns.

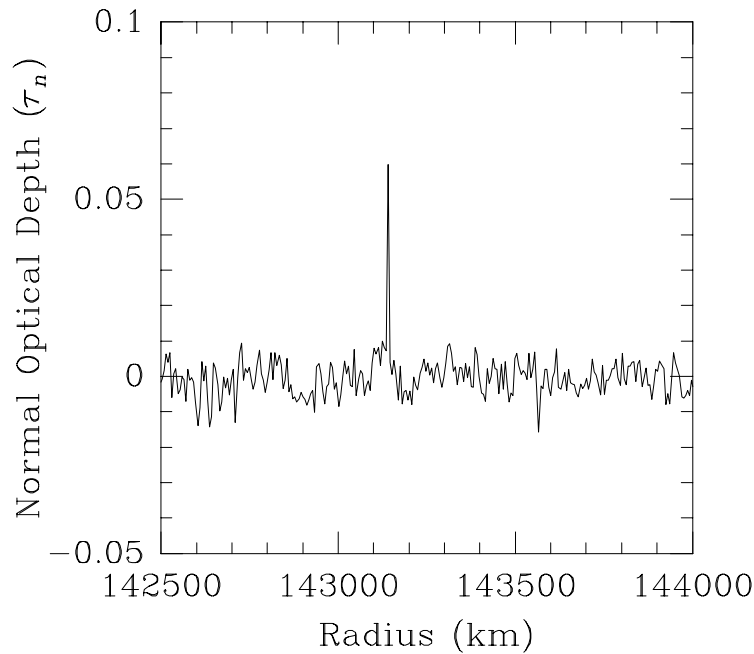


Fig. I.5. This new feature, located exterior to the F ring at 143,141 km from Saturn's center, occurs in a single image, which is normal in all respects. The sampling rate was such that a ringlet would appear on several consecutive frames, ruling out the possibility that the feature is an undiscovered ringlet. Further possibilities are discussed in the text.

Chapter 7

RING MASSES

Prior to the Voyager encounter, the mass of Saturn's rings was undetermined. Imaging and other direct observations did little to indicate what the mass could be, and the rings did not observably affect the orbits of the moons or the trajectory of Pioneer 11. Null *et al.* (1981) calculated an upper bound of 1.7×10^{-6} Saturn masses (9.7×10^{23} g) from this latter fact.

However, optical depth is directly related to the total mass of material in the beam. If one makes several assumptions about ring composition and uses models to fit for the surface mass density at many locations, one can use an occultation optical depth profile to make very rough mass estimates. Indeed, both the Voyager PPS (Esposito *et al.* 1983b, hereafter referred to as EOW) and UVS (Holberg *et al.* 1982) teams performed such an analysis, with good agreement between their results.

As presented by EOW in their Eq. (4), the mass M_{12} between two ring radii R_1 and R_2 can be estimated by integrating the normal optical depth τ_n as a function of radius r , with a mean mass extinction coefficient $\bar{\kappa}$ obtained from model fits to density waves:

$$M_{12} = \frac{2\pi}{\bar{\kappa}} \int_{R_1}^{R_2} \tau_n(r) r dr. \quad (\text{I.6})$$

Equation I.6 assumes axisymmetry and a constant $\kappa(r)$. Because of the rings' differential rotation, axisymmetry is a good assumption. A constant κ is less valid: Showalter and Nicholson (1990) find a higher fraction of large particles in the A ring than in the C ring and inner Cassini Division, for example. Larger particles would present less cross-sectional area per unit mass, lowering κ locally. Further, $\kappa = \tau_n/\sigma$, where σ is the surface mass density. To date, the best indicators of surface mass density have been fits of linear models to sometimes-nonlinear spiral waves in the rings. Finding a meaningful representative optical depth inside a density wave is itself a non-trivial matter, since the sharp peaks of the waves are smoothed in the lower-resolution lightcurves (see Fig. I.4). Using the 20- and 0.5-km PPS profiles, we were unable to reproduce the mean optical depth numbers stated for several density waves in EOW's Table I (EOW used the original 0.1-km-resolution profile). The mean optical depths of density waves in the 20- and 0.5-km PPS profiles also differed from each other, though mean optical depths in more quiescent regions were consistent. Finally, the high peak density of some of the waves may induce collision rates that locally alter the particle-size distribution, yielding a κ that is not representative

of the rest of the rings.

Despite these many caveats, the optical depth integral remains the best mass estimate to date. Although the numbers produced may only approximate the actual mass, Eq. I.6 is useful as an area-weighted means of comparing systematic differences between profiles, with or without $\bar{\kappa}$. As such it complements the mean optical depth of a ring section.

Only the optically deep B ring has thus far resisted this technique. The detection thresholds of EOW and Holberg *et al.* were $\tau_n=2.55$ and $\tau_n=2.85$, respectively, and Holberg *et al.* state that at least 15% of the B ring was below the limit. However, the Voyager observations provided many determinations of surface mass density from model fits to density and bending waves (EOW, Cuzzi *et al.* 1984), so all that was needed was an occultation with signal throughout the B ring. Because of the convolution effects explained above under Optical Depth Profile Morphology, we did not attempt to derive surface mass densities by fitting models to density-wave trains, nor, for the reasons just discussed, were we able to determine useful mean optical depths inside the density waves (and thus potentially eliminate wavelength-dependent effects in our assumed $\bar{\kappa}$). We must thus use EOW's mass extinction coefficient of $(1.3 \pm 0.5) \times 10^{-2} \text{ cm}^2/\text{g}$ to estimate ring masses from the IRTF 28 Sgr data. The estimated masses and the mean optical depths of each region from our egress profile are presented in Table I.III. Also included are the same quantities measured by the same method from the 20-km PPS profile used in Figs. I.3 and I.4, and, for

convenient comparison, the numbers published in EOW. As one would expect from the similarities of the profiles, mass estimates from this occultation are similar to the Voyager numbers, with an overall tendency to estimate a slightly lower mass.

If the systematic large-scale differences between the IRTF 28 Sgr and PPS ring profiles do turn out to be due to indirect signal and extinction efficiency differences, then our geometric optical depths (i.e., optical depths related to the fraction of a beam occupied by the physical cross sections of particles in it) would all be greater than what we observed, and the optical-depth integrals and masses would thus increase. The mass of the B ring, in particular, would still be a lower bound.

TABLE I.III
Ring Masses and Mean Optical Depths

| Region | Inner edge ^a (km) | Outer edge ^a (km) | PPS ^b mean τ_n | PPS _{20 km} mean τ_n | IRTF mean τ_n | PPS ^c mass (10^{20} g) | PPS _{20 km} mass (10^{20} g) | IRTF mass (10^{20} g) |
|----------|------------------------------------|------------------------------------|-----------------------------------|---------------------------------------|-----------------------|--------------------------------------------|------------------------------------------------|--------------------------------|
| Inner C | 74,809 | 83,859 | 0.08 | 0.08 | 0.12 | 2.8 | 2.9 | 4.2 |
| Outer C | 83,859 | 91,702 | 0.15 | 0.13 | 0.17 | 5.1 | 4.3 | 5.5 |
| Inner B | 91,702 | 100,148 | 1.21 | 1.01 | 0.96 | 45.5 | 39.8 | 36.8 |
| Middle B | 100,148 | 103,768 | 1.76 | 1.80 | 1.38 | 34.1 | 32.0 | 24.7 |
| Outer B | 103,768 | 117,643 | 1.84 | 1.86 | 1.68 | 113.8 | 137.7 | 122.9 |
| Cassini | 117,643 | 121,867 | 0.12 | 0.12 | 0.16 | 3.4 | 2.8 | 3.5 |
| Inner A | 121,867 | 130,313 | 0.70 | 0.56 | 0.48 | 39.8 | 28.6 | 24.3 |
| Outer A | 130,313 | 136,949 | 0.57 | 0.46 | 0.52 | 22.8 | 19.7 | 20.8 |
| Total | 74,809 | 136,949 | | | | 284.5 | 267.8 | 242.7 |

Note. $\bar{\kappa} = (1.3 \pm 0.5) \times 10^{-2} \text{ cm}^2/\text{g}$. Formal fractional error of mass numbers derived in this work = ~ 0.4 . Mass numbers presented in this table in most cases exceed their precision, but since the uncertainty is primarily in the constant mass extinction coefficient, the PPS_{20 km} and IRTF numbers can be compared. Since numbers from EOW were published with one digit of precision, they should not be compared to the others beyond one digit.

^a As used by EOW, converted to km. $1R_S = 60,330 \text{ km}$.

^b As reported by EOW.

^c Reported by EOW. Original publication had one digit of precision and used Saturn masses as a unit. Those numbers have been converted to grams with the planetary mass of $5.69 \times 10^{29} \text{ g}$ stated in EOW Table II.

Chapter 8

CONCLUSIONS

The 28 Sgr event has produced a collection of data sets very rich both in potential science results and in analysis challenges. Work based on highly accurate optical depths in the ring system must likely await a correction for indirect signal and extinction efficiency. Such work would include more accurate optical-depth integrals and particle-size modeling of specific features based on multiple wavelengths of observation. Those aspects of the science that do not rely on accurate optical depths in the ring system, such as atmospheric work and pole fitting based on event times, can proceed with the existing profiles and are in fact being pursued by several groups [see French *et al.* (1993) and Hubbard *et al.* (1993) for pole solutions based on an ensemble of datasets, including this one].

These observations extend the wavelength coverage of the previously existing Saturn ring optical depth profiles into the infrared and provide a different chord from the

Voyager occultations. Infrared imaging detectors, although still in their infancy, already offer much to the occultation observer. We have shown that, despite their complexity when compared to single-channel photometers, sufficient timing accuracy can be achieved with array systems to make them quite viable for occultations with much higher time resolution than this event required. Although considerably more analysis effort is required with arrays than with single-channel photometers, the ability to model and subtract the background light field, and indeed to do so several times with different methods, can result in lightcurves with lower noise than would be possible with conventional aperture photometry. As larger, faster, quieter, and more linear chips become available, we hope that new cameras will be built with occultations in mind, and refer the prospective camera designer to our appendix on the topic.

Appendix A

APPENDIX: IMAGING OBSERVATIONS OF OCCULTATIONS

The use of charge-coupled devices (CCDs) and infrared arrays in several recent occultations (this work, Elliot *et al.* 1989, Dunham *et al.* 1989, French *et al.* 1989, di Cicco and Robinson 1989) represents a major step in the development of technology and techniques for occultations. This step is not an easy one; the amount of data to be handled, and its transmission rate, can be three orders of magnitude greater than for single-channel photometers. Accurate timing can be harder to achieve as well, because the instrument system through which the signal propagates is much more complex. With this many images (over 44,400 in our case), image processing must be automated, and there are many steps before one has a lightcurve. By contrast, the single-channel photometer observer leaves the observatory with a lightcurve in hand.

The advantages of imaging an occultation are quite definite, however. The most obvious is that photometry is done after the fact. Ordinary tracking errors (other than the failure of a major telescope component) do not exist, as the digital “aperture” can, if desired, be centered on the star in each image. One can try different combinations of apertures and models of the background light field. Also, the background to subtract from each raw data point is generally calculated from an image region a few arcseconds from the star on each frame, so a varying sky brightness is no longer a major problem. The result is a lightcurve with a significantly higher signal-to-noise ratio (SNR) than is generally possible with single-channel photometers. One can therefore observe fainter stars. In addition, having actual images makes it possible to inspect the data for the causes of anomalous lightcurve features.

A camera must be designed to observe occultations. The major new concerns are the amount of data, the data rate, the frame rate, and accurate absolute timing of images. The first three of these are interrelated, and a compromise in one can affect the others.

An 8-Hz occultation observed over 4 hr would produce over 10^5 images. If the detector is a 62×58 -pixel infrared array producing 2-byte pixels, there will be 0.8 Gbytes of data to store. If multiple storage media (e.g., disks or tapes) are required to hold the data, the system must change between them without losing images. Many camera computers are real-time machines for which large or extra disks are either not available or are difficult to work into the configuration. One solution to this problem

is to have the camera computer transmit the data over a network to a machine with a bigger disk. Under this scheme, no copy of the data is kept on the camera computer, so one must ensure that the end-to-end throughput is sufficient to handle the data rate of the array in its fastest readout mode. Many commercially available distributed filesystems do not meet this criterion, but it is a simple matter to write data transmission and reception programs that “shout” and “listen” on a network and that run effectively as fast as the hardware allows.

In the case of large arrays such as most CCDs, reading and recording the entire chip is both impractical and pointless: a relatively small subframe (50×50 pixels) can easily be made to contain the star and sufficient background for photometry. Reading more can take longer, reducing the time resolution possible. The camera software must therefore be programmed to do fast subframe readouts; in CCD’s the uninteresting pixels are typically read as quickly as possible and discarded, and the region of interest is read at a slower rate to gain SNR from the readout amplifier. By adjusting the frame rate and the size of the stored frame, one has effective control over the amount of data to be saved. For the 28 Sgr event, our observing plan was a compromise to avoid saturating the detector (hence the $\frac{1}{12}$ -sec integration times), oversample the lightcurve comfortably (4 frames/sec, achieved by averaging 3 frames of $\frac{1}{12}$ sec each), and not overflow the local storage (recording only 62×12 -pixel subframes). Storage was on two disk drives, with no loss of data in the switch.

The final point to consider is timing. The main appeal of occultations is the high

spatial resolution achievable by observing rapidly in time; time is the independent variable. The better one knows when each image was taken, the more accurate the lightcurve. In many occultations a timing error that would be unnoticed in more conventional observations can produce a very noticeable deviation in apparent position of the star behind the occulting object.

If observations from many stations are to be used simultaneously, their timing systems must have good synchronization to a common time base. In addition to the accuracy of the clock, one must also know the delay between a clock signal and the action of interest (shutter closing or array readout/clear). The timing accuracy required is determined by the event geometry and the nature of the object under study, but 0.1 msec is not an uncommon figure. The GOES system provides ~ 1 msec accuracy over a large region of the globe without the need to travel to a time standard for a sync to UT. Oven-stabilized quartz and rubidium oscillators, such as those used in this work, give sufficient accuracy to drive any system in use today (10^{-10} or better), but they require a sync and can be very sensitive to environmental conditions. The solution for occultation astronomers may lie in the Global Positioning System (GPS). GPS receivers are available commercially and are designed for field work. They can receive their satellite sync almost anywhere in the world, and run with accuracies similar to those of the quartz and rubidium standards.

Until recently, almost all observers based their timing on the introduction of an observable time signal from an accurate clock into their data stream. This can be

done mechanically, for example by chopping with the secondary mirror; electrically, by adding a time signal to the analog output of a photometer; or digitally, by reading an external clock as an array reads out. Although these methods are adequate for most purposes, they require some effort during the analysis to recover the actual time of each frame. In this observation, we replaced the clock in the camera computer with an accurate one, and monitored it with a second clock. The timing solution of such a system is much simpler and the duration of each exposure is inherently more accurate.

Imaging occultations requires highly functional cameras that have been designed for the job. The additional design features are not expensive, but do require some thought and effort during development. The computer which runs a good occultation camera requires either sufficient storage capacity for a large number (10^5) of small images or the ability to transmit to another machine with such a storage medium. One must not lose data during media changes. In order to get sufficiently high time resolution and to save space, fast subframe readouts are important. Gaining this capability generally only requires writing software that takes advantage of the capabilities of the array. The most difficult feature to incorporate in an occultation camera is accurate timing. One needs a good clock, it needs a source of synchronization, and there must be a mechanism to associate its time with the data. In the ideal case, the accurate clock will be the clock running the camera, rather than an external reference. While the cost of these enhancements is not negligible, one must also ask what the cost is of failing to achieve the best possible signal-to-noise ratio

for an event, such as this one, which is statistically likely to occur only once in 80 years (Elliot 1990).

ACKNOWLEDGMENTS

We thank M. D. Myers for the excellent occultation camera software, which allowed us to synchronize the images to an accurate time base. We also thank him for his care and diligence in counting microseconds in interrupt service routines and in transferring the occultation data from 78, eight-inch, 1-Mbyte floppy disks to magnetic tape. We are grateful to T. Herbst for conceiving of and running the strip chart recorder mentioned under Timing System and for several other level-headed thoughts during the observation. We are indebted to N. Hironaka at the NIST WWVH station for loaning us the rubidium standard and for his help in analyzing the timing problems and recovering the absolute synchronization to UTC, R. L. Baron for designing the 60-Hz modification to the MIT portable clock, the staff of the IRTF for their considerable support of this observation, D. Mink and P. D. Nicholson for disseminating useful information on event circumstances prior to the occultation, P. D. Nicholson and R. G. French for their insightful comments and discussions during the data reduction phase, and referees B. Sicardy and M. Showalter for helpful

suggestions. We thank N. M. Donahue for his vital assistance in creating the synthetic Saturn image. This work was supported in part by NSF Grant AST-8906011. IRAF is distributed by the National Optical Astronomy Observatories, which is operated by the Association of Universities for Research in Astronomy, Inc., under cooperative agreement with the National Science Foundation. The Astronomical Data Center at the NASA Goddard Space Flight Center provided infrared magnitudes.

REFERENCES

- BARON, R. L. 1989. *Occultation Astronomy and Instrumentation: Studies of the Uranian Upper Atmosphere*. Ph.D. thesis, Massachusetts Institute of Technology.
- BRAHIC, A., B. SICARDY, F. ROQUES, C. FERRARI, AND I. GRENIER 1989. Observation of the July 3, 1989 stellar occultation by Saturn and its rings. *Bull. Am. Astron. Soc.* **21**, 951.
- CONNER, S. R. 1984. *Photometry of Hyperion*. Master's thesis, Massachusetts Institute of Technology.
- CUZZI, J. N., AND J. A. BURNS 1988. Charged particle depletion surrounding Saturn's F ring: Evidence for a moonlet belt? *Icarus* **74**, 284–324.
- CUZZI, J.N., J. J. LISSAUER, L. W. ESPOSITO, J. B. HOLBERG, E. A. MAROUF, G. L. TYLER, AND A. BOISCHOT 1984. Saturn's rings: Properties and processes. In *Planetary Rings* (R. Greenberg and A. Brahic, Eds.), pp. 73–199. Univ. of Arizona Press, Tucson.
- DAVIS, L. 1987. Specifications for the Aperture Photometry Package. In *IRAF User Handbook*, Vol. 2b. National Optical Astronomy Observatories. P.O. Box

- 26732, Tucson, Arizona 85726.
- DI CICCIO, D., AND L. J. ROBINSON 1989. Video images of the occultation of 28 Sagittarii by Saturn, July 2–3, 1989. *Bull. Am. Astron. Soc.* **21**, 953.
- DUNHAM, E. W., J. L. ELLIOT, A. S. BOSH, L. L. CORDELLA, AND L. A. YOUNG 1989. KAO optical observations of the occultation of 28 Sgr by Saturn. *Bull. Am. Astron. Soc.* **21**, 932.
- ELLIOT, J. L. 1990. An occult view of Titan. *Nature* **343**, 315–316.
- ELLIOT, J. L., E. W. DUNHAM, A. S. BOSH, S. M. SLIVAN, L. A. YOUNG, L. H. WASSERMAN, R. L. MILLIS 1989. Pluto’s atmosphere. *Icarus* **77**, 148–170.
- ESPOSITO, L. W., M. O’CALLAGHAN, K. E. SIMMONS, C. W. HORD, R. A. WEST, A. L. LANE, R. B. POMPHREY, D. L. COFFEEN, AND M. SATO 1983a. Voyager photopolarimeter stellar occultation of Saturn’s rings. *J. Geophys. Res.* **88**, 8643–8649.
- ESPOSITO, L. W., M. O’CALLAGHAN, AND R. A. WEST 1983b. The structure of Saturn’s rings: Implications from the Voyager stellar occultation. *Icarus* **56**, 439–452.
- FORREST, W. J., J. L. PIPHER, Z. NINKOV, AND J. D. GARNETT 1989. InSb DRO array characteristics. In *Proceedings of the Third Infrared Detector Technology Workshop* (C. R. McCreight, Compiler), pp. 157–182. (NASA Tech. Mem. 102,209).
- FRENCH, R. G., M. A. CLARK, E. TOLLESTRUP, E. ROBINSON, P. HARVEY, L. HEILMAN, R. FARR, AND R. STEINING 1989. The 3 July 1989 occultation of 28 Sgr by Saturn and its rings: Observations from McDonald Observatory. *Bull. Am.*

Astron. Soc. **21**, 928.

FRENCH, R. G., P. D. NICHOLSON, M. L. COOKE, J. L. ELLIOT, K. MATTHEWS, O. PERKOVIĆ, E. TOLLESTRUP, P. HARVEY, N. J. CHANOVER, M. A. CLARK, E. W. DUNHAM, W. J. FORREST, J. HARRINGTON, J. L. PIPHER, A. BRAHIC, I. GRENIER, F. ROQUES, AND M. ARNDT 1993. Geometry of the Saturn system from the 3 July 1989 occultation of 28 Sgr and Voyager observations. *Icarus* **103**, 163–214.

HARRINGTON, J., E. W. DUNHAM, W. J. FORREST, AND J. L. PIPHER 1989. IRTF infrared imaging observations of the occultation of 28 Sgr by Saturn. *Bull. Am. Astron. Soc.* **21**, 954.

HOLBERG, J. B., W. T. FORRESTER, AND J. J. LISSAUER 1982. Identification of resonance features within the rings of Saturn. *Nature* **297**, 115–120.

HUBBARD, W., C. PORCO, D. HUNTEN, G. RIEKE, M. RIEKE, E. ASPHAUG, R. CLARK, V. HAEMMERLE, J. HALLER, J. HOLBERG, L. LEBOSKY, R. MARCIALIS, D. MCCARTHY, B. MCLEOD, M. BUIE, J. ELIAS, D. JEWITT, E. PERSSON, T. BOROSON, S. WEST, R. LANDAU, AND W. SCHUSTER 1989. Preliminary results from the occultation of 28 Sgr by the Saturn system: Saturn. *Bull. Am. Astron. Soc.* **21**, 951.

HUBBARD, W. B., C. C. PORCO, D. M. HUNTEN, G. H. RIEKE, M. J. RIEKE, D. W. MCCARTHY, V. HAEMMERLE, R. CLARK, E. P. TURTLE, J. HALLER, B. MCLEOD, L. A. LEBOSKY, R. MARCIALIS, J. B. HOLBERG, R. LANDAU, L. CARRASCO, J. ELIAS, M. W. BUIE, S. E. PERSSON, T. BOROSON, S. WEST, AND D. J. MINK 1993. The occultation of 28 Sgr by Saturn: Saturn pole

- position and astrometry. *Icarus* **103**, 215–234.
- KILLIAN, A. M., AND A. S. DALTON 1985. Stellar occultations by Saturn’s rings for 1985–1991. *Astron. J.* **90**, 2372–2376.
- NEUGEBAUER, G., AND LEIGHTON 1969. Two-micron sky survey. In *Selected Astronomical Catalogs Volume 1* (CD-ROM released 1992). Astronomical Data Center, NASA Goddard Space Flight Center, Greenbelt, MD 20771.
- NICHOLSON, P. D., M. L. COOKE, AND E. PELTON 1990. An absolute radius scale for Saturn’s rings. *Astron. J.* **100**, 1339–1362.
- NICHOLSON, P. D., O. PERKOVIĆ, K. MATTHEWS, AND R. G. FRENCH 1991. Saturn’s rings: optical depth profiles at $\lambda 3.9 \mu\text{m}$ from the occultation of 28 Sgr. *Bull. Am. Astron. Soc.* **23**, 1178.
- NULL, G. W., E. L. LAU, E. D. BILLER, AND J. D. ANDERSON 1981. Saturn gravity results obtained from Pioneer 11 tracking data and Earth-based Saturn satellite data. *Astron. J.* **86**, 456–468.
- PORCO, C., W. HUBBARD, D. HUNTEN, G. RIEKE, M. RIEKE, E. ASPHAUG, R. CLARK, V. HAEMMERLE, J. HALLER, J. HOLBERG, L. LEBOSKY, R. MARCIALIS, D. MCCARTHY, B. MCLEOD, M. BUIE, J. ELIAS, D. JEWITT, E. PERSSON, T. BOROSON, AND S. WEST 1989. Preliminary results from the occultation of 28 Sgr by the Saturn system: Rings. *Bull. Am. Astron. Soc.* **21**, 928.
- REITSEMA, H., W. HUBBARD, D. HUNTEN, C. PORCO, N. BROSCHE, Y. NEVO, E. CARREIRA, F. ROSSI, AND L. WASSERMAN 1989. Preliminary results from the occultation of 28 Sgr by the Saturn system: Titan. *Bull. Am. Astron. Soc.*

21, 958.

- SHOWALTER, M. R., AND P. D. NICHOLSON 1990. Saturn's rings through a microscope: Particle size constraints from the Voyager PPS scan. *Icarus* **87**, 285–306.
- SICARDY, B., C. FERRARI, C. HUBERT, H. LECACHEUX, S. PAU, F. ROQUES, F. COLAS, F. SÈVRES, J. E. ARLOT, W. THUILLOT, J. L. VIDAL, C. BLANCO, S. CRISTALDI, C. BUILE, A. KLOTZ, AND E. THOUVENOT 1989. The occultation of 28 Sgr by Titan on July 3, 1989. *Bull. Am. Astron. Soc.* **21**, 958.
- SINACHOPOULOS, D. 1989. A photometric study of wide visual double stars with significant relative proper motions. *Astron. Astrophys. Suppl. Ser.* **81**, 103–114.
- TAYLOR, G. E. 1983. I.A.U. Commission 20 working group on the prediction of occultations by satellites and minor planets, Bulletin 30, 1983, Feb. 21.
- TODY, D. 1986. The IRAF data reduction and analysis system. In *Instrumentation in Astronomy VI* (D. L. Crawford, Ed.) Proc. SPIE., Vol. 627, p. 733.

Part II

A Power Spectrum Analysis of Jupiter's Tropospheric Thermal Emission

A Power Spectrum Analysis of Jupiter's Tropospheric Thermal Emission

JOSEPH HARRINGTON,^{*,1,2} TIMOTHY E. DOWLING,^{*} RICHARD L. BARON,^{†,2}
AND TOBIAS OWEN[†]

^{}Department of Earth, Atmospheric, and Planetary Sciences
Room 54-410
Massachusetts Institute of Technology
Cambridge, Massachusetts 02139*

*[†]Institute for Astronomy
University of Hawai'i
Honolulu, Hawai'i 96822*

In preparation for *Icarus*.

¹To whom correspondence should be addressed.

²Visiting Astronomer at the Infrared Telescope Facility, which is operated by the University of Hawai'i under contract from the National Aeronautics and Space Administration.

We observed Jupiter’s tropospheric clouds at a wavelength of $4.9\ \mu\text{m}$ (1% bandpass) through the NASA Infrared Telescope Facility (Mauna Kea, HI). The ProtoCAM 62×58 -pixel infrared array camera took a total of 229 full-disc 3×3 - and 4×4 -image mosaics on 19 nights spanning the period 11 Jan. through 19 Apr. 1992. Resolution was typically $0.5 - 0.75''$. We obtained full longitude coverage on 12 Jan.; 10, 27, and 28 Feb.; 12, and 22 Mar. The images show atmospheric structure at all resolved spatial scales, and have an optical depth range of ~ 4.6 . New algorithms automatically assembled the images into mosaics and located the planetary center.

Our wavelength senses deep tropospheric thermal emission and reveals overlying cloud opacities. We averaged zonal power spectra of planetary maps from the nights with 360° coverage to search for energy input scales. L. D. Travis (1978, *J. Atmos. Sci.* 35, 1584–1595) has established a correspondence between the power spectra of kinetic energy and of cloud patterns for the Earth. Assuming this holds for Jupiter, we fit power laws between wavenumber and power spectral density in spectra averaged over a wide region not obscured by dark clouds and find an exponent of -3.09 ± 0.13 between planetary wavenumbers ~ 25 and ~ 50 . The predicted power-law exponent for an enstrophy cascade is -3 . Power laws at low wavenumbers fit poorly and do not show the exponent of $-5/3$ predicted for energy cascades. Cascade power laws only occur at wavenumbers where energy input is insignificant.

The Rossby deformation radius, L_d , is near our resolution limit. However, if L_d were an energy input scale, one would expect the energy to cascade to smaller wavenumbers and to disrupt the observed enstrophy cascade. The inertial cascade is evidence that baroclinic instability is not important on Jupiter. The low-wavenumber cutoff of the enstrophy cascade corresponds to the width of the zonal jets. This is consistent with the idea that zonal turbulent scales do not exceed the meridional extent of the jets.

We also searched for slowly-moving planetary waves. A previous search at this wavelength (J. A. Magalhães *et al.* 1990, *Icarus* 88, 39–72) did not detect such waves, but had one-tenth the spatial resolution and half the temporal resolution of this work. Our spectra do not contain peaks that persist in the six planetary maps, except for the equatorial plumes at planetary wavenumber 10. We conclude that, during Jan. – Apr. 1992, the troposphere did not contain observable planetary waves. This leaves unresolved the questions of how the stratospheric slowly-moving thermal features are tied to the rotation period of the magnetic field and how the convecting deep interior interacts with tropospheric dynamics.

Chapter 1

INTRODUCTION

The data we can gather from Jupiter's atmosphere are quite different from those available for Earth's (see the review by Dowling 1994). Because small cloud features are abundant and long-lived on Jupiter, we can compile cloud-top wind fields for any region we desire. Much of Earth's atmosphere is clear at any given time and many of the clouds that do exist are orographic or change too quickly to be tracked for long periods. In this sense, we have better cloud-top wind field data for Jupiter than for Earth. On the other hand, the vertical structure of Earth's atmosphere is continuously monitored by balloons and other means, and ground, ship, and satellite weather stations monitor the interface between the atmosphere and the surface. In contrast, we have only a few measurements of Jupiter's vertical temperature profile from stellar and radio occultations (Lindal *et al.* 1981, Gautier *et al.* 1981), and spatial temperature maps with coarse vertical resolution (Orton *et al.* 1991).

All of the data for Jupiter's atmosphere comes from the stratosphere and upper troposphere, at or above the upper cloud deck, since the same clouds that give us so many wind tracers prevent us from directly measuring most properties of the deep troposphere. This is unfortunate since the predicted ammonium hydrosulfide and water cloud layers, the sources of the convective plumes, and the interface with the convecting deep interior all lie below the visible clouds. Our lack of detailed knowledge about these hidden phenomena is what impedes our understanding of even regular changes in the cloud patterns, despite more than a century of continual monitoring by professional and amateur astronomers.

We therefore need observation methods sensitive below the ~ 670 mbar ammonia cloud tops. One such method will be the entry probe to be released by the Galileo spacecraft on 7 December 1995. Another method, pursued here and by Harrington *et al.* (1994, see Part III), Flasar and Gierasch (1986), and others, is to identify different types of atmospheric waves and use their dispersion properties to infer local conditions. The most optimistic of wave approaches is the search for trapped inertia-gravity waves proposed by Ingersoll *et al.* (1994), who predicted that if impacting fragments of comet Shoemaker-Levy 9 deposited much energy in or below the putative 5-bar Jovian water cloud, the energy would be trapped in a wave guide at that level. Even for a small impactor, the amplitude of the wave would be strong enough to perturb the atmosphere well into the stratosphere, creating a thermal and perhaps a condensation trace that would be visible from Earth and that contained information about the water cloud. Pressure levels as deep as 5 bars may thus be accessible to

wave methods.

As a practical matter, however, the only inertia-gravity waves strong enough to be seen from Earth are those predicted for cometary impacts, and their wavelengths may be too short to be resolved by ground-based telescopes. Rossby waves are considerably longer than inertia-gravity waves and can manifest themselves in several different ways that might be visible from the ground. These waves act as probes of atmospheric properties such as stratification and deep structure. Many of these phenomena can have a profound effect on the nature of a planet's atmospheric dynamics. However, it can be difficult to find enough of them to fit a dispersion relation.

Many of the key questions that remain unanswered about Jupiter's atmosphere are clarified by the needs of dynamical models. Some of the most prominent features, such as the Great Red Spot (GRS) and white ovals, are already being reproduced, and even generated, by simple models that include only a relatively restricted subset of the physics (Dowling and Ingersoll 1989, Williams and Wilson 1988). These and several other models (see also Ingersoll and Cuong 1981, Marcus 1988, and the review by Dowling 1994) have one active and one underlying steady layer. The model by Dowling and Ingersoll most closely resembles the data because it uses bottom conditions derived from a vortex-tube-stretching analysis of the Voyager images of the GRS and white oval BC. As we gather more data, the models can meaningfully incorporate more physics and explain more phenomena.

The vortex-tube-stretching analysis (Dowling and Ingersoll 1988) reduced the so-called 1-1/2 layer models to only one free parameter in the region covered by the data. One way to express this parameter is as the effective deformation radius, L_d , of the active layer. As discussed in Harrington *et al.* (1994) and Part III and shown in Appendix D, L_d strongly influences the behavior of phenomena such as Rossby and inertia-gravity waves and vortices. It is the length scale of the smallest vortices and because it strongly influences the formation, behavior, and longevity of vortices. The deformation radius is related to the stratification, and to date the best determinations of this quantity for Jupiter have come from analysis of the vertical temperature profile, $T(p)$, where T is temperature and p is pressure. We have a good value of $L_d \approx 3,000$ km in the stratosphere (Conrath *et al.* 1981), where $T(p)$ is well-known. However, $T(p)$ is poorly known in the troposphere and in addition it asymptotically approaches the adiabatic profile ($L_d=0$). Since L_d follows the difference between the actual and the adiabatic profile, it would be difficult to derive L_d directly from $T(p)$ accurately even if $T(p)$ were well-known in the troposphere. At the present time, estimates for L_d in the troposphere of Jupiter lie in the range 500–2,500 km, uncertain by a factor of 5. Since L_d is usually squared, key terms in atmospheric models are uncertain by a factor of 25.

Dowling (1993, 1995) has proposed that Jupiter’s zonal wind field obeys a potential vorticity distribution that keeps it nearly neutrally stable with respect to Arnol’d’s second stability criterion, based on a vorticity analysis of Voyager wind data. The

empirical relation of Dowling's (1993) Eq. 15 states

$$L_d^2 \frac{\partial \bar{q}}{\partial y} \approx \bar{u}, \quad (\text{II.1})$$

where q is the potential vorticity, u is the zonal wind (positive eastward), y is the north-south coordinate, and an overbar indicates a zonal average. This implies a certain approximate dispersion relation for Rossby waves on Jupiter. The quasi-geostrophic dispersion relation (see Appendix D) is:

$$c \approx \bar{u} - \frac{L_d^2 \frac{\partial \bar{q}}{\partial y}}{1 + \frac{L_d^2}{R^2} \left(\frac{m^2}{\cos^2(\lambda)} + n^2 \right)}, \quad (\text{II.2})$$

where c is the wave phase speed, m and n are the number of wavelengths in the zonal and meridional directions, and λ is planetographic latitude. Substituting gives

$$c \approx \bar{u} \left(1 - \frac{1}{1 + \frac{L_d^2}{R^2} \left(\frac{m^2}{\cos^2(\lambda)} + n^2 \right)} \right). \quad (\text{II.3})$$

Eq. II.3 says that the longest waves (small m and n) move slowly with respect to the deep planetary interior. This idea is supported by several observations of slowly-moving thermal features in Jupiter's atmosphere (see below). The relation could be tested by measuring the speeds of a few waves with different planetary wavenumbers. If the observations confirmed the relation, they would also give a value for the deformation radius at the depth of the observed waves.

A number of previous observations of planetary-scale periodic features on Jupiter

and Saturn lead us to a general search for such features in Jupiter's troposphere. The difficulty of calculating L_d from $T(p)$ points to the use of other methods, such as the wave analyses proposed and attempted here and in Harrington *et al.* (1994, see Part III). On Saturn, Voyager detected a ribbon-like wave (Sromovsky *et al.* 1983) near 20° N and a six-lobed polar hexagon (Godfrey 1988). At least the hexagon, and possibly the ribbon, can be interpreted as Rossby waves. Although there are many wave-like features in Voyager images of Jupiter's cloud tops, the only globally periodic features seen are the equatorial plumes. Thought to be convection sites, the plumes appear quite different from the features on Saturn. Allison (1990) has suggested that conditional instabilities associated with deep waves drive the convection.

Infrared observations have also detected global, periodic, thermal features in Jupiter's stratosphere and upper troposphere (Deming *et al.* 1989, Magalhães *et al.* 1989, 1990); these features move slowly with respect to the interior rotation rate. Deming *et al.* (1989) report activity at 20° N and Magalhães *et al.* (1989) reports thermal waves at 15° N, planetary wavenumber 9, 270 mbar and 20° N, wavenumber 11, in $45\text{-}\mu\text{m}$ cloud opacities. Unfortunately, all these observations used single-channel or linear-array detectors. They either do not sample many latitudes (Deming *et al.* 1989) or they have poor spatial resolution (Magalhães *et al.* 1989,1990).

The observed slow wave velocity relative to the presumed period of internal planetary rotation (system III) implies a mechanism whereby the dynamics of the stratosphere and upper troposphere are tied, possibly indirectly, to the deep interior. Hart *et al.*

(1986a,b) have proposed one possible mechanism: a pattern of convection cells in the planetary interior, the top of which form a fluid velocity pattern static in the rest frame of the interior. They simulate the interior convection of the giant planets both by numerical methods and by means of a physical model flown in space. For rapidly-rotating spheres with a purely radial temperature gradient, these models form narrow convection cells that extend from pole to pole but cover only a few tens of degrees in longitude. If this “banana-cell” pattern of alternating upward and downward velocity were strong enough, it could affect the effective thickness of the troposphere and act as a forcing selection mechanism for Rossby waves. Such a pattern might give rise to waves stationary in the rest frame of the cells and having planetary wavenumbers related to the number of convection cells. Meridionally-aligned features might also result. Detection of a strong convection pattern underlying the weather layer would begin to address the question of what ties Jupiter’s zonal wind system and stratospheric thermal waves to the rotation rate of the deep interior.

The observational challenge is to probe below the ammonia clouds. For Jupiter, $5\text{ }\mu\text{m}$ is a key wavelength region for a tropospheric wave search because it offers a view of clouds backlit by thermal emission from near the 5-bar level, deep in the troposphere. This wavelength is sensitive to different types of features from reflected-light imaging, showing particular detail in areas that are dark in reflected light. Until recently, only raster-scanned, single-channel data have been available at wavelengths near $5\text{ }\mu\text{m}$. The development of infrared array detectors allows routine imaging of tropospheric cloud opacities at this wavelength. Unlike the gradually-varying

stratospheric thermal appearance, the troposphere contains horizontal structure well below the limit of current resolution.

The troposphere is both the most dynamic region in the atmosphere and the region where L_d is least known. In this study we image Jupiter at 4.9 μm regularly over a period of about 100 days. We seek periodic structure in Jupiter's troposphere by examining cloud-intensity power spectra derived from ground-based images. Our identification of the inertial subrange of a turbulent enstrophy cascade between planetary wavenumbers ~ 25 and ~ 50 indicates a lack of energy input on these scales and raises a number of dynamical questions. The power spectrum analysis also reveals a lack of large-scale, slowly-moving features. A previous discrete wave search with data from the Voyager Infrared Imaging Spectrometer (IRIS) at the same wavelength (Magalhães *et al.* 1990) similarly yielded null results. However, the present study has ten times the linear spatial resolution and twice the temporal resolution of the spacecraft study. A lack of slowly-moving features raises questions such as how the wave phenomena observed in the stratosphere (Deming *et al.* 1989, Magalhães *et al.* 1989, 1990) are linked through the troposphere to the rotation rate of the planetary interior.

Chapter 2 describes the observations; Appendix A provides further detail on automating mosaicking observations. Chapter 3 summarizes the automatic processing of the $\sim 5,000$ images obtained, with Appendices B and C describing in detail several new techniques for constructing mosaics and for centering the planetary image at this

wavelength. Chapter 4 presents the spectral analysis and Chapter 5 presents several different wave search methods. We conclude with interpretation and considerations for future observers in Chapter 6. A final appendix presents the physics of Rossby waves in a manner tractable to those without a fluid dynamics background.

Chapter 2

OBSERVATIONS

We obtained 229 full-disc, 3×3 - and 4×4 -image mosaics of Jupiter at wavelengths near $5\text{ }\mu\text{m}$ with the ProtoCAM 62×58 -pixel InSb array camera (Toomey *et al.* 1990) at the NASA Infrared Telescope Facility (IRTF) on Mauna Kea, Hawai'i. Frame exposure times were 10 sec for 3×3 mosaics and 17 sec for 4×4 mosaics, the total time being divided into 100 summed chip readouts. Read noise for the array is ~ 300 electrons, and there are 24 electrons/ADU (analog-to-digital unit). We used a circular variable filter with a 1% spectral bandpass. Table II.I presents a synopsis of the data and observations. The schedule gave us regular observations approximately every two weeks for over three months. We were fortunate to lose only one night (29 Jan) to an instrument failure and we lost no significant time to weather.

We shared observing time with an auroral program that had very similar imaging needs (Connerney *et al.* 1993b, Baron *et al.* 1994). By combining telescope time

TABLE II.I
Synopsis of Data and Observations

| Date | Day ^a | From UTC ^b | To UTC ^b | λ μm | # of Mosaics 3×3 4×4 | Personnel ^c | Notes |
|--------|------------------|--------------------------|------------------------|----------------------------|----------------------------|------------------------|------------|
| 11 Jan | 633 | 10:54 | 15:00 | 4.5 4.9 | 2 4 | RLB, JH | |
| 12 Jan | 634 | 9:54 | 16:23 | 4.9 | 14 | RLB, JH | 360° |
| 13 Jan | 635 | 10:41 | 16:34 | 4.9 | 12 | JH | |
| 25 Jan | 647 | 11:54 | 16:23 | 4.9 | 11 | JH | |
| 30 Jan | 652 | 10:12 | 13:00 | 4.65 4.75 4.9 5.2 | 1 1 4 1 | RLB, TO | sep. proj. |
| 31 Jan | 653 | 9:42 | 10:52 | 4.9 | 2 | RLB, TO | sep. proj. |
| 3 Feb | 656 | 10:54 | 15:25 | 4.9 | 10 | JH | |
| 9 Feb | 662 | 11:17 | 16:13 | 4.9 | 10 | JH | HST |
| 10 Feb | 663 | 8:35 | 16:43 | 4.9 | 21 | JH | 360°, HST |
| 27 Feb | 680 | 7:06 | 14:50 | 4.9 | 24 | JH | 360° |
| 28 Feb | 681 | 7:04 | 15:26 | 4.9 | 21 | 1 JH | 360° |
| 7 Mar | 689 | 6:14 | 9:23 | 4.9 | 9 | JH | |
| 8 Mar | 690 | 6:12 | 10:10 | 4.9 | 12 | JH | |
| 12 Mar | 694 | 6:05 | 14:27 | 4.9 | 11 | 5 JH | 360° |
| 20 Mar | 702 | 6:19 | 8:59 | 4.9 | 8 | JH | |
| 21 Mar | 703 | 6:36 | 9:20 | 4.9 | 7 | JH | |
| 22 Mar | 704 | 6:00 | 13:21 | 4.9 | 8 | 9 JH | 360° |
| 6 Apr | 719 | 5:22 | 9:24 | 4.9 | | 8 JH | |
| 19 Apr | 732 | 5:28 | 9:25 | 4.9 | | 13 JH | 4.9-only |

^a Julian day -2,448,000.

^b Start time of first (last) mosaic imaging sequence.

^c List of observers: RLB: Richard Baron, JH: Joseph Harrington, TO: Tobias Owen.

Notes:

360° Night with full longitude coverage.

sep. proj. This night's observations were for a separate project of RLB and TO.

HST Hubble Space Telescope observed Jupiter on this night.

4.9-only no parallel auroral imaging on this night.

allocations, we were able to extend our temporal coverage to several months while keeping the observations frequent enough to resolve weather changes on Jupiter and to span the Ulysses spacecraft encounter (relevant to the aurora project). By alternating mosaics at our two different wavelengths on all but the last two nights, both projects received maximum longitude coverage and minimal exposure to bad seeing, weather, or instrument problems. A final major benefit was that the same observer could perform both sets of observations, requiring only one person to travel to the telescope.

Mosaic assembly is based on a comparison of the overlapping regions of two images. If the contents of the overlap region changes, it makes registration much more difficult, especially if the assembly is automatic. Particularly variable effects for these observations included planetary rotation, telescope pointing, image quality (due to changing image point-spread function, tracking errors, and focus), and thermal emission from the sky. When possible, we guided on a moon of Jupiter to stabilize pointing and tracking; doing so resulted in noticeably improved images.

The key to limiting variable effects at the telescope is rapid imaging. To accommodate this need, the IRTF staff provided a special version of the camera control program that enabled us to specify telescope offsets in command files. We then wrote command files that set up filters and took mosaics at our two wavelengths and two resolutions. This reduced mosaic time from 11–13 minutes to 7 minutes, and reduced observer intervention from continual to four times per mosaic: inserting the acquisition camera pickoff mirror into the telescope beam, centering the planet on a

television screen, removing the pickoff mirror, and typing the command file name. The reduced interaction virtually eliminated the opportunities for human error and freed the observer for other tasks for most of the 7 minutes.

We also focused every few hours, whenever there was a temperature change in the dome of more than a few degrees, and whenever the images began to look poor. The image quality would have benefitted from even more frequent refocus, but we could not afford the time. The Earth's atmosphere emits strongly at this wavelength, requiring that each object image be followed immediately by an image of nearby sky for later subtraction. We took linearity, dome and sky flat field, dark current, and bias images for standard error corrections.

Chapter 3

IMAGE PROCESSING

The size of the dataset, over 5,000 images including calibration, motivated the development of an automated processing system. The benefit of this approach becomes clear when considering a change to an early stage of processing. To propagate such a change manually through the entire dataset might mean many days of work and poor reproducibility. An automatic pipeline that can be run with a single command after each change ensures both reproducible work and the constant availability of the latest processed data, even when experimenting with many techniques at once. Also, one need not store many versions of each image; the raw data and the pipeline together can produce any given reduced data item upon request.

The reduction pipeline consists of a series of independent, general-purpose modules, some called by higher-level modules and the highest run explicitly from command lists with one command per final mosaic. The strategic use of command lists allows

individual treatment of aberrant images without special-purpose code in the modules. Examples of specific processing include dealing with mosaics whose images appear in a non-standard order, or which have 4×4 instead of 3×3 frames. The pipeline consisted of five phases: frame processing, mosaicking, centering, correcting for limb darkening, and mapping. Frame processing further consists of individual camera frame corrections for readout amplifier bias, nonlinear response, bad pixels, sensitivity variations (flat field), thermal emission from the sky, and orientation.

A program provided by the IRTF performed corrections for readout amplifier bias and pixel response linearity. Linearity data are a series of frames with increasing exposure times that look at a uniformly-emitting source: dewar window cover. We took useful linearity data by the standard IRTF procedure on 27, 28 Feb., 12, 21 Mar., and 6 Apr. Linearity data taken on 9 Feb., 7, 16 Mar., and 18 Apr. were unusable for reasons that are not clear. Since the operator must manually place the metal cover over the window before the linearity exposures, one hypothesis for the damaged data is that the operator's hands warmed the cover significantly, and that it cooled during the 20-30 minute run of the linearity command file on the nights with bad data. We chose to discard those data and used linearity frames from the nearest night with good data. By plotting the values of several pixels *versus* exposure time, looking at histograms of pixel values, and consulting with the IRTF staff, we determined which sets of linearity data to use. Since the IRTF procedure only recommends taking these data once per run, and the change between the sets is not large, we believe our final correction to be adequate.

We used the linearity correction factors for the array to create bad pixel lists on each night with good linearity data. The correction factors are very different for bad and good pixels, so we made a histogram of the factors for each night and set a cutoff value that included all reasonably good pixels. The bad pixel lists consisted of the outliers plus a few pixels added by hand later. Interpolating data from surrounding good pixels was adequate correction for bad pixels in the images.

We took flat fields on 13 Jan., 9, 10, 27, 28 Feb., 7, 8, 12, 20, 21, 22 Mar., 6, and 19 Apr., and used the nearest night with flat field data for the remainder. On nights with multiple image scales from 3×3 and 4×4 mosaics, we took flats with both image scales. Flat fields consisted of the reciprocal of the normalized difference between several summed images of the sky and of the dome. Each pixel in the flat field is thus a multiplicative correction factor for the sensitivity of the corresponding pixel on the chip at our wavelength. The dome-minus-sky method removes the thermal emission pattern of the telescope itself, and is only necessary in the thermal infrared (wavelengths longer than $\sim 4\text{ }\mu\text{m}$).

All images in the dataset consist of only one “observing cycle.” In IRTF parlance, an observing cycle is an object-sky image pair, and one can program several cycles in advance. The ProtoCAM program would add all object and all sky frames in a cycle to create just two image files. Since we had only one cycle in each image file, and were taking a series of images at the same wavelength and in the same part of the sky, we interpolate sky frames to the time of each object image from the two nearest

sky images, and subtract it from the object image to produce the final image pixel values (we extrapolate in the case of the first mosaic image).

Even with sky interpolation, the backgrounds in the images do not match sufficiently well for mosaicking, so we adjusted the background levels in each image by adding or subtracting a constant value to or from each image. The adjustment values for the pieces are such that the overlapping background regions of two adjacent pieces contain the same total flux after adjustment. Since the planet occupies the center mosaic piece(s), only the edge pieces can receive this adjustment. Further, there may be a disagreement in the adjustment found by rounding the planetary limb clockwise as opposed to counter-clockwise. Even distribution of the discrepancy around the edge and an interpolated shift for the central images worked reasonably well, and significantly improved the resulting mosaics.

We developed a new algorithm for automatically mosaicking images. Appendix B presents the problem of mosaicking and our solution to it. Likewise, we found a new procedure for identifying the planetary limb (sometimes called “navigating” the image) without human intervention. This was necessary because traditional techniques developed for optical images search for a low-contrast planetary disc with high contrast against the sky. In the 5- μm wavelength region, Jupiter has high-contrast features on the disc but the disc itself has relatively low contrast against the sky. The problem and our solution to it are presented in Appendix C.

Our wavelength is sensitive primarily to thermally emitted light from deep in the troposphere. The light is subject to differential attenuation as it leaves Jupiter's atmosphere, according to its emission angle. To correct this effect, we divide each pixel's value by $\mu^{\kappa-1}$ where μ is the emission angle cosine and κ is a fitted parameter. We find the value of κ by plotting lines of constant latitude in mapped images at latitudes with minimal variation in pixel value. The value $\kappa=2.25$ made these plots most linear across the planetary disc in a sampling of images. This method is like the standard Minnaert method described by Veverka *et al.* (1978) and Smith *et al.* (1986) with the incident angle cosine removed because there is minimal reflected light in these images. The lack of reflected light was borne out by the lack of a shadow when Io transited the disc. We attach no physical significance to this method or to the value of κ . As expected, we did not find it necessary to compensate for extinction by the Earth's atmosphere. Finally, we used a mapping program developed by T. Satoh (Goddard Spaceflight Center) to create a planetographic equidistant cylindrical projection of each mosaic, and laminated sections of these to make composite maps of the planet on each observing night.

Images of Jupiter in the 5- μm band are highly detailed, and ours show structure at all length scales larger than the resolution limit (see Figs. II.1 and II.6A). According to the standard interpretation (Ingersoll 1973), the images show light emitted thermally near the 5-bar pressure level (deep in the troposphere) and absorbed at higher altitudes by clouds of varying optical thickness. The prominent dark features correspond well to bright clouds in visible-light images. Thermal images at most

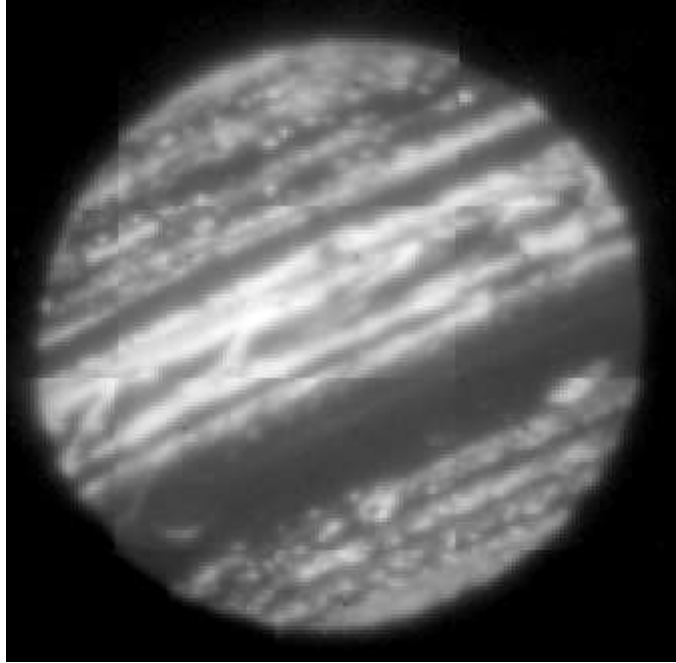


Fig. II.1. Automatically-assembled 4×4 mosaic image of Jupiter taken at a wavelength of $4.9\text{ }\mu\text{m}$ on 22 March 1992. No smoothing or pixel interpolation have been applied.

other wavelengths in the $3\text{--}20\text{-}\mu\text{m}$ range show a comparatively uniform planet.

No structure appears in the darkest regions of these images. The most prominent dark region is the latitude band containing the GRS, which is itself only barely visible. The dark zone's width and lack of structure indicate the total absorption of light from below, though scattered light from nearby bright features puts the observed light level slightly higher than that of the sky. In contrast, the brightest parts of the images are always small and peaked. The lack of wide regions of uniform brightness indicates that there is cloud structure on the entire planetary disc and that there may be no completely clear zones. This means we can measure only relative cloud optical thicknesses, and it prevents a direct probe of thermal variation in the 5-bar

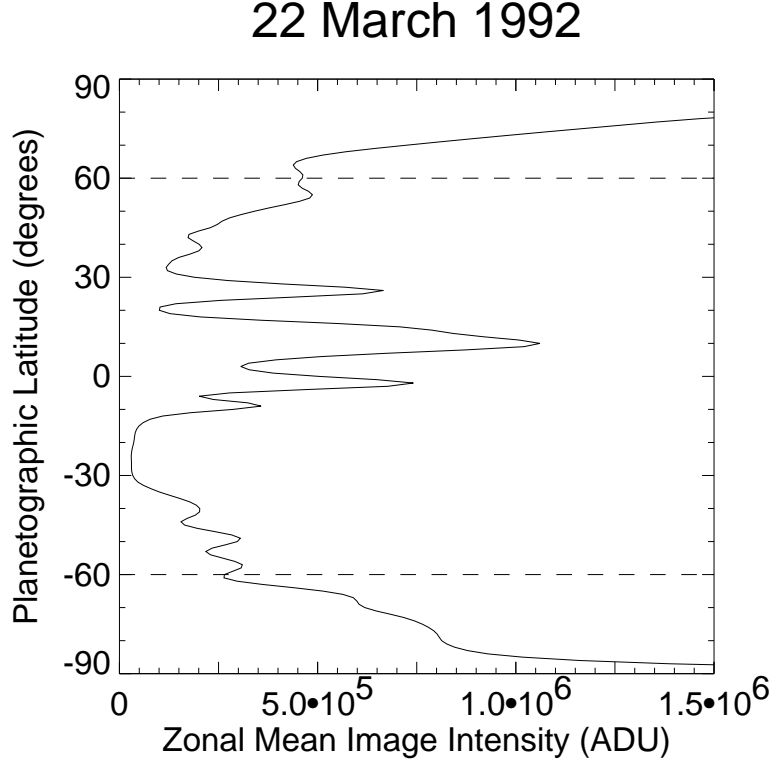


Fig. II.2. Zonal mean image intensity for the composite map of 22 March 1992 (see Fig. II.3). The plot for other nights is nearly identical. Data values poleward of 60° latitude suffer in map projection.

source region. The brightest pixels in the mapped images have intensities of $\sim 2 \times 10^6$ ADU above the sky background; the scattered light in the dimmest areas shines at 2×10^4 ADU, for a factor of 100 dynamic range without modeling and subtracting the scattered light. This corresponds to a relative optical depth of 4.6.

To filter out as many local effects as possible and to make best use of Fourier techniques, the present analysis concentrates exclusively on those nights with full 360° coverage (12 Jan., 10, 27, 28 Feb., 12, and 22 Mar.). Our principal analysis tool is a zonal, linear Fourier decomposition. We extracted 1° -wide latitude strips from the

composite maps and performed a linear fast Fourier transform (FFT) on each strip, obtaining the amplitude and phase. Since the latitude bands of Jupiter have different absolute flux levels (see Fig. II.2), their transform amplitudes also differ. To compare them, we divide each strip by its constant term, so the value at wavenumber 0 is 1.0. The processing then diverges for the two analyses. For the spectral power-law fits of Chapter 4, we square the transform amplitude to get power spectral density and then take the log (see Fig. II.5). For the wave search of Chapter 5, we create transform images by re-stacking the FFT strips (see Fig. II.3). These images have coordinates of wavenumber and latitude, and pixel values of either phase or normalized amplitude. The amplitude images receive further processing: Taken in bulk, their intensities tend to vary inversely with the wavenumber. Multiplying each amplitude value by its wavenumber leaves a transform image with features on a nearly flat background.

As one would expect from the detailed images, the amplitude plots show many fea-

Fig. II.3. The following pages show composites of mapped Jupiter images at a wavelength of $4.9\ \mu\text{m}$, one composite for each night of full longitude coverage (we interpolated over 4° of missing longitude on 12 Jan. 1992). These images prominently show the equatorial plumes. The dark region near -25° contains the Great Red Spot, which is very faint at this wavelength. Structure at latitudes poleward of 60° suffers in map projection.

Adjacent to the composites are the amplitudes of their zonal fast Fourier transform (FFT), displayed as an image with coordinates of wavenumber and latitude. To create these images, we performed a linear FFT on each strip of latitude in the mapped data, computed the transform amplitude, and re-stacked the resulting strips according to their latitude. We then normalized the amplitudes by the mean intensity level of the latitude band and multiplied by the wavenumber to remove an overall pattern. This allows us to detect features standing above the overall cloud activity pattern at relatively high wavenumbers. See text for further discussion.

12 January 1992

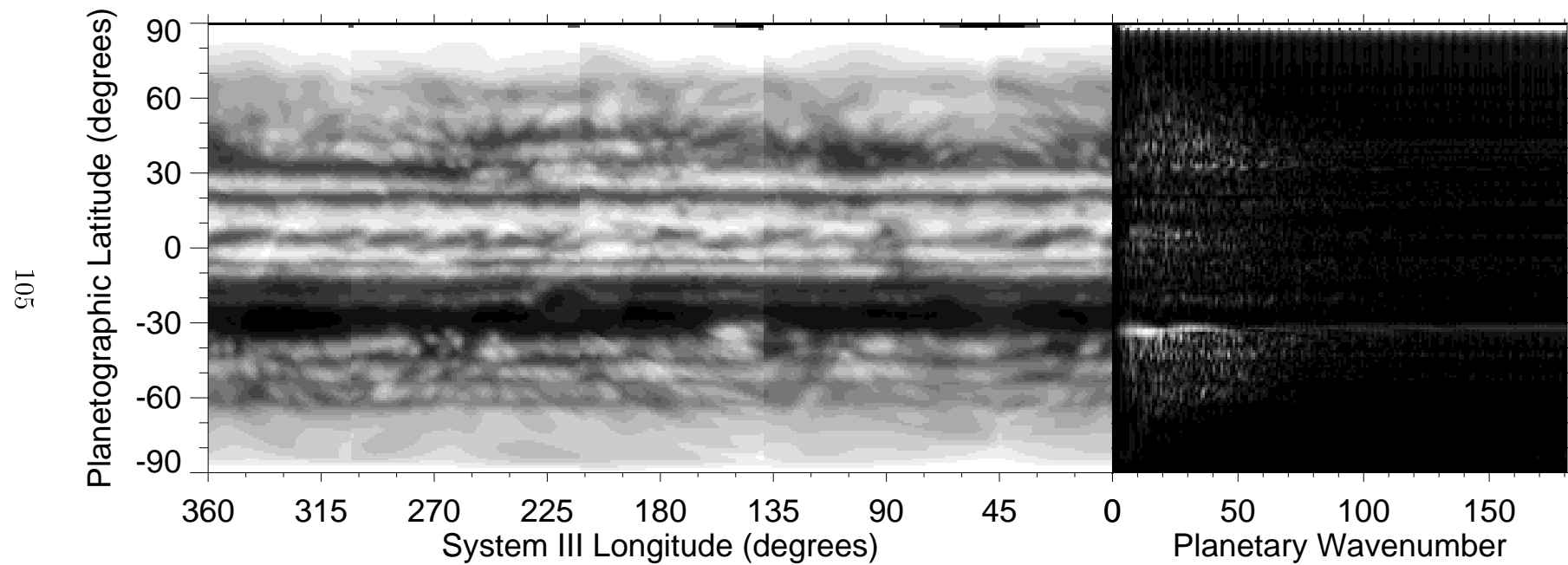


Fig. II.3—*Continued*

10 February 1992

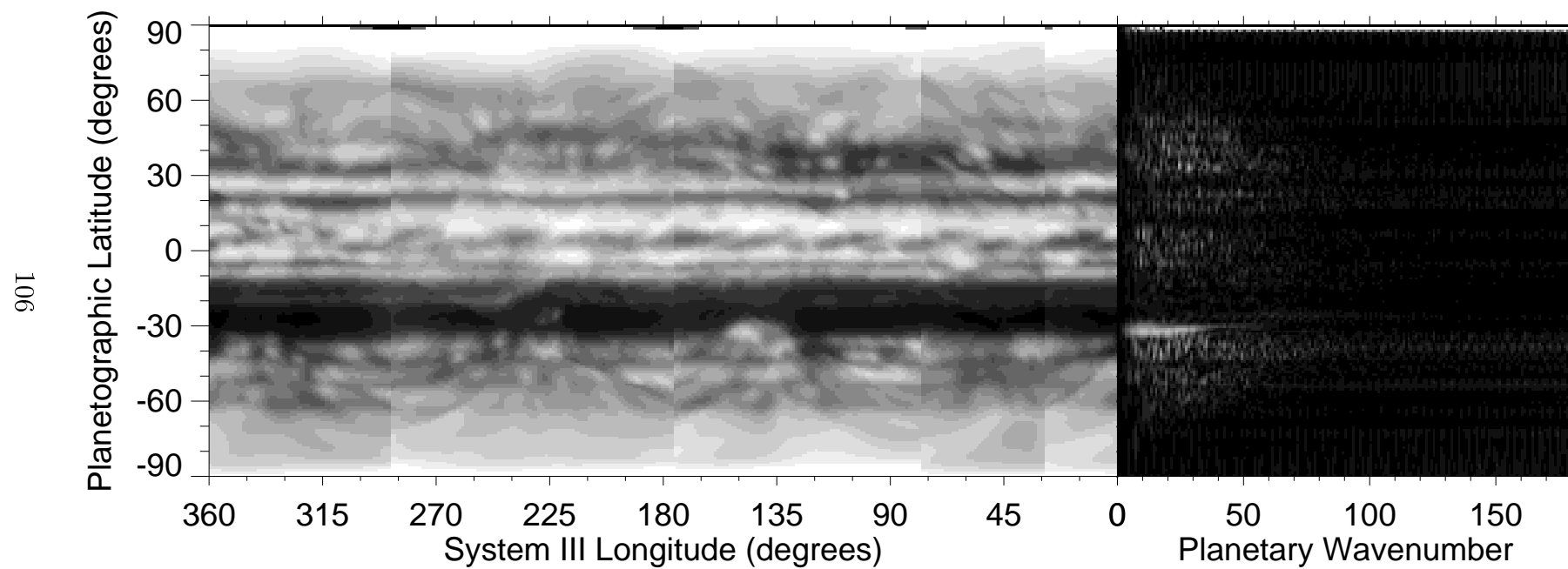


Fig. II.3—*Continued*

27 February 1992

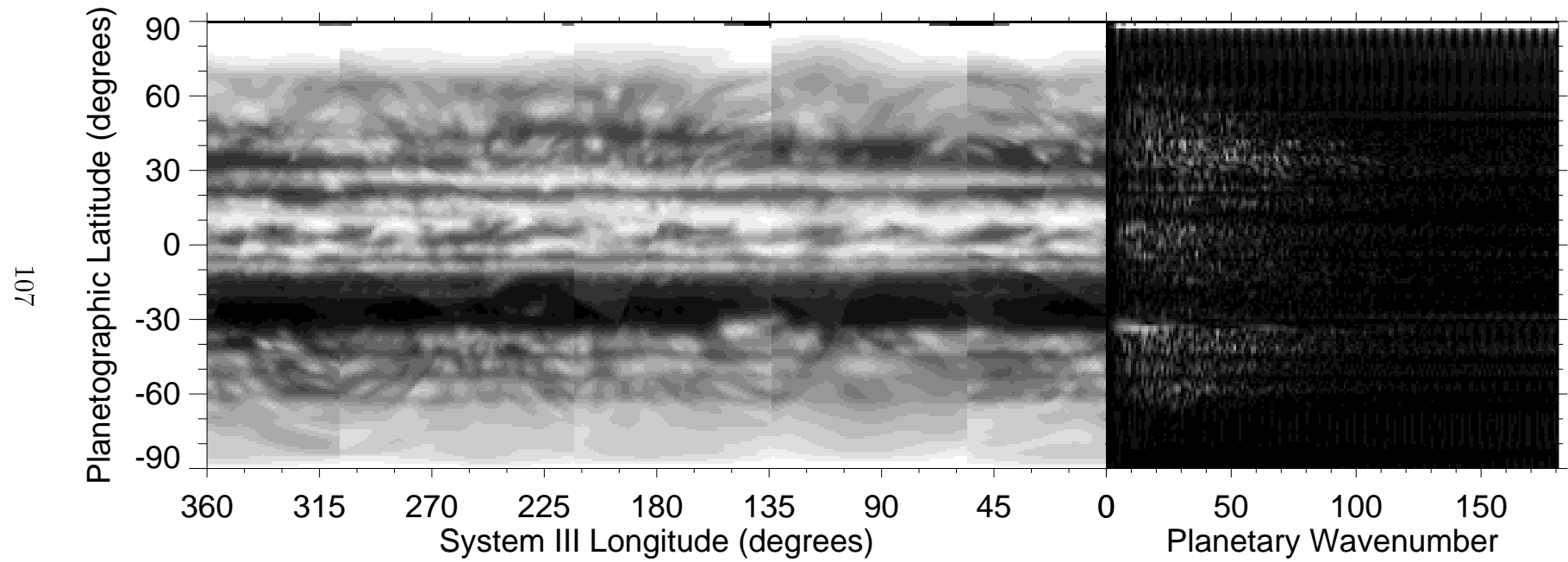


Fig. II.3—*Continued*

28 February 1992

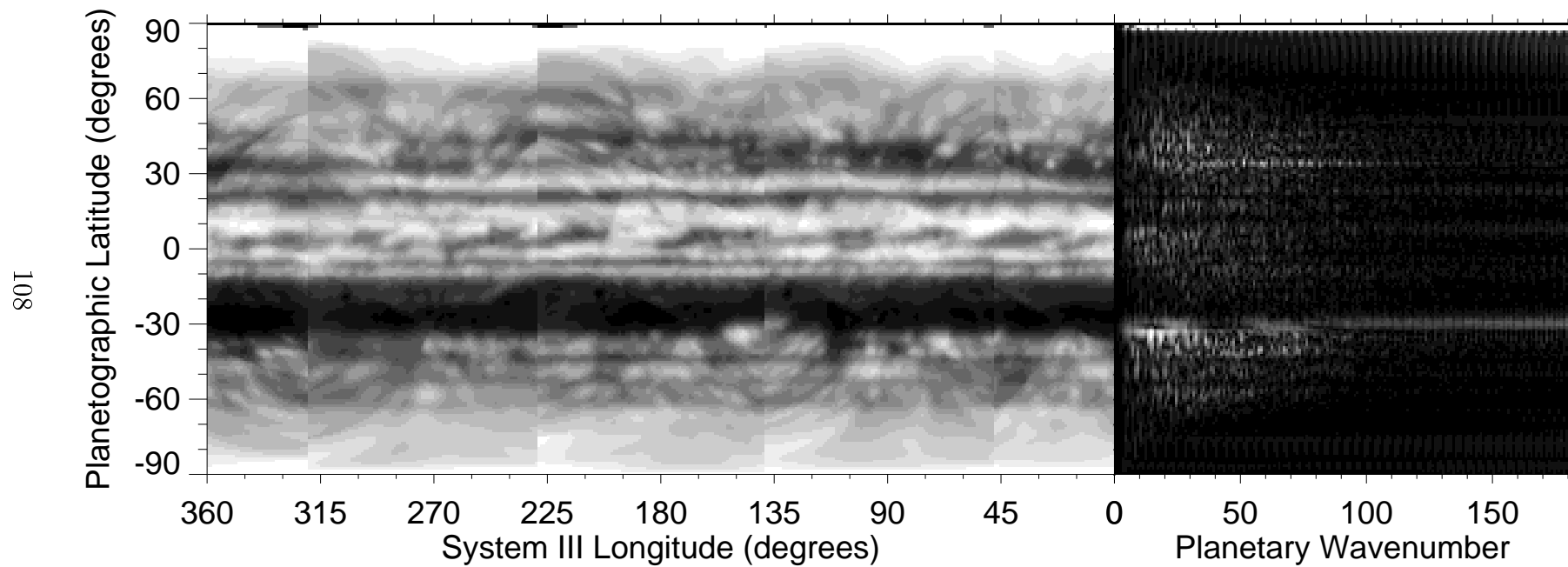


Fig. II.3—*Continued*

12 March 1992

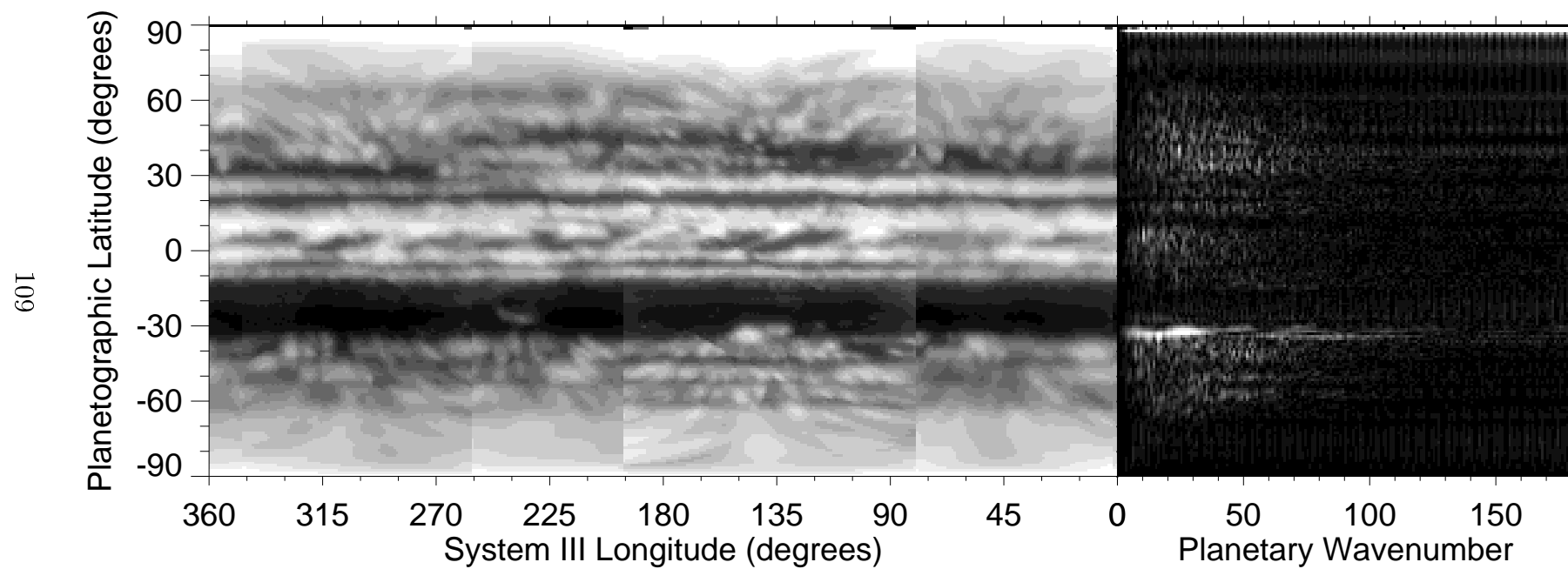


Fig. II.3—*Continued*

22 March 1992

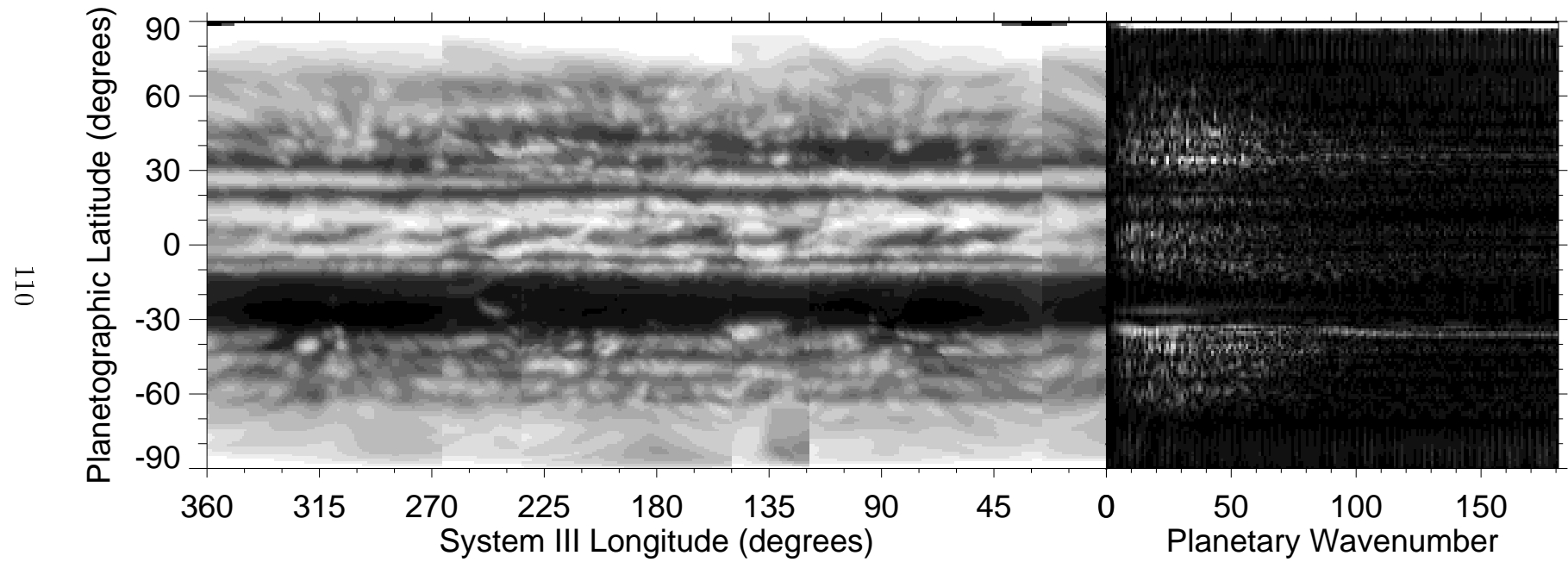


Fig. II.3—*Continued*

tures. Even after removing the overall wavenumber-dependent pattern, most of the activity is at low wavenumbers. There are few small, discrete features in the maps that are as bright as the broad bands, and those that are as bright do not appear at regular intervals and hence do not create bright features in the amplitude images. Some familiar atmospheric features are identifiable in the amplitude plots. Most prominent are the equatorial plumes and the result of their convective spread at wavenumbers 10–14, latitudes -5 – 5° . The southern edge of the GRS appears as a broad feature at latitude -27° . Other discrete bright features in the maps appear as broad features in transform amplitude as well, notably the hot spot at -32° .

Chapter 4

SPECTRAL ANALYSIS

Oceanographers and meteorologists derive information about the dynamics of their respective fluids by analyzing power spectra of kinetic energy and interpreting the results in terms of turbulence theory. One derives kinetic energy fields most directly from velocity measurements, but the analysis requires accuracies much better than the ~ 5 m/sec uncertainties of data for planets other than the Earth (Travis 1978, Limaye 1986). However, Travis found a close correspondence between power spectra of Earth's atmospheric kinetic energy and power spectra of its visible and infrared cloud intensities, based on data from Mariner 10 and several Earth-orbiting weather satellites (see Fig. II.4). Assuming that the correspondence held for Venus as well, he used cloud-intensity spectra as a surrogate for energy spectra in his analysis of Venus's atmospheric dynamics. By making the same assumption and using the present data, we add Jupiter to the set of planets for which this analysis has been carried out.

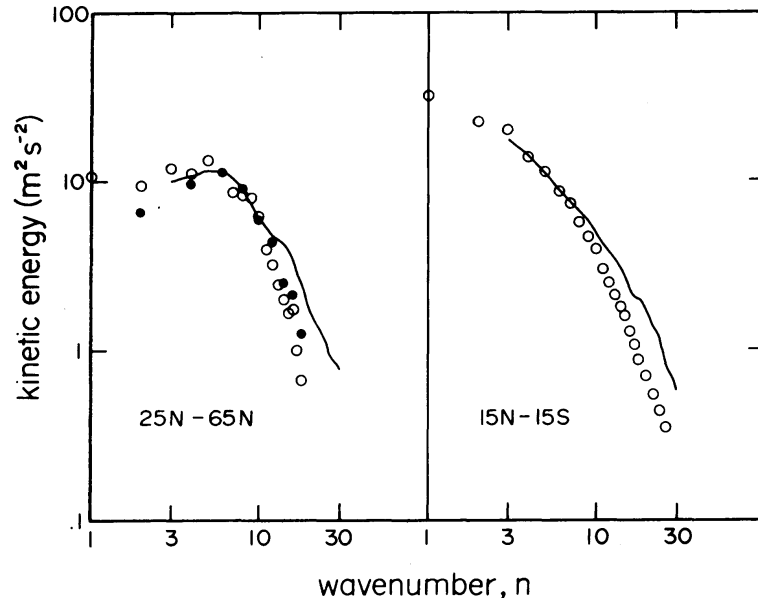


Fig. II.4. Comparison of Earth kinetic energy power spectra (circles) and cloud intensity spectra (lines) from Travis (1978). Open circles are from wind data sensitive to 200 mbar at a single latitude. Filled circles are from winds at 200, 500, and 850 mbar at two discrete latitudes. The circles are normalized to match each other at $n=6$, which Travis identifies as the scale of the deformation radius for Earth. The lines are an average of power spectra derived from 12 Earth images at a variety of visible and infrared wavelengths. The spectrum from each of the Earth images is an average of its zonal spectra over the indicated latitude region. Agreement is good at $n \leq 10$, but slopes tend to be underestimated by the cloud data at higher wavenumbers. In spite of the clearly different forms taken by the power spectra at different latitudes, the two different measurements agree on the basic form in both regions. Reproduced from *Journal of the Atmospheric Sciences*.

In 1941, Kolmogorov studied turbulence in three-dimensional, isotropic flows. He found (see Kundu 1990, p. 441) that vortex stretching draws energy from the largest vortices to the smallest, cascading the energy to ever-smaller scales until molecular viscosity dissipates it as heat. By a scaling argument, he found the form of this energy cascade's power spectrum to be proportional to $k^{-5/3}$, where k is the wavenumber.

However, fluids on a rotating planet can behave quite differently from non-rotating fluids. The Taylor-Proudman theorem (see Kundu 1990, p. 487) states that a rapidly rotating fluid resists accelerations parallel to the local axis of rotation, effectively reducing three dimensions to two. Work by Charney (1971) and many others, including most recently Danilov *et al.* (1994), addresses turbulence in this quasi-two-dimensional regime. They find turbulent cascades in kinetic energy power spectra due both to energy and to enstrophy. The energy cascade has the familiar $-5/3$ power-law exponent, but eddy merging is the dominant form of energy transfer, such that the cascade is to larger scales and smaller wavenumbers, opposite to the direction of the three-dimensional cascade. It is enstrophy, which is the square of potential vorticity and is conserved in two-dimensional, inviscid flow, that cascades to larger wavenumbers, this time with a power law of -3 . Enstrophy is a measure of filamentary structure and such structures tend to be lengthened and folded, becoming still more filamentary. Both the energy and enstrophy cascade power laws are apparent only in wavenumbers ranges where energy input and removal do not occur. Such regions are called "inertial subranges." On a log-log plot, the power spectrum of a planetary system with energy input at a single wavenumber that is far from the scales of energy

removal appears as a pair of line segments with slopes of $-5/3$ and -3 , joined at the input wavenumber.

Travis's (1978) analysis used images of clouds in both reflected visible light and thermal infrared emission to draw the comparison between kinetic energy spectra and cloud spectra. His cloud data come from a Mariner 10 image ($\lambda_{eff}=0.578 \mu\text{m}$), five pairs of visible ($0.55 - 0.75 \mu\text{m}$) and thermal infrared ($10.5 - 12.6 \mu\text{m}$) images from the SMS-1 satellite, and one such pair from the GOES-1 satellite. His Fig. 5, reproduced here in Fig. II.4, shows a solid line for the cloud brightness spectrum and circles for various kinetic energy spectra (see caption). The important result for this work is that the form of the spectrum in the two latitude regions differs at low wavenumbers, but that in each case the two differently-derived spectra follow each other. There is a tendency of the cloud brightness to overestimate the power at wavenumbers above 10. While it is not immediately clear how to translate this departure point into terms relevant to Jupiter, the planetary wavenumber equivalent to this distance on Jupiter is 119, which is above the spatial resolution of our data, and the dynamical scale L_d , which for Earth shows a clear peak at $n = 6$ in Fig. II.4, is near our resolution of $m \approx 60$ limit on Jupiter. See below for further discussion of wavenumber sensitivity limits.

To achieve maximum signal-to-noise ratio in the power spectra, we averaged the spectra at each latitude over the six nights, using log averaging for consistency with the subsequent analysis. The width of the image point-spread function (PSF) cor-

responds to about 2° on Jupiter, and this is roughly equivalent to the smoothing performed by Travis to eliminate an aliasing problem from abrupt cloud edges in his data for the Earth. We found that smoothing the data to reduce noise also reduced our sensitivity at high wavenumbers. We have therefore not further smoothed our data, nor have we rebinned their intensities.

For most latitudes within the $\pm 60^\circ$ limits of good map projection, plotting the logarithm of the resulting spectra against the logarithm of the planetary wavenumber (m) reveals a shallow negative slope with some apparent downward curvature at low wavenumbers, then a steeper slope at higher wavenumbers (usually starting near $m \sim 25$) that is relatively linear, and finally a low-intensity tail starting at $m \sim 60$, whose slope and curvature vary with latitude. Averaging neighboring latitudes in the logarithm significantly reduces noise and reveals the underlying structure more clearly. Fig. II.5 presents the power spectra of latitude ranges corresponding to the zonal jets, as well as an overall spectrum averaging the data over a large latitude range and a meridional spectrum averaged over all longitudes. Line segments illustrate linear least-squares fits to ranges of the wavenumber; these segments have the same slope as their respective fits but are displaced three sample standard deviations above and below the data. A wide separation thus indicates a relatively large scatter in the points.

Table II.II gives the range of the two fits on each plot as well as the fitted slope and intercept and the formal errors of the linear regression. The low-wavenumber

TABLE II.II
Linear Fits to Regions of the Spectra

| Latitude Range (°) | Planetary Wavenumber Range | Slope | Intercept ($\ln P$) | Scatter ($\sigma_{\ln P}$) |
|---------------------------|-----------------------------------------------|------------------|--------------------------|---------------------------------|
| 10 – 50 | 1 – 26 | -1.29 ± 0.05 | -3.86 ± 0.12 | 0.20 |
| 40 – 60 | 1 – 24 | -1.10 ± 0.06 | -4.23 ± 0.14 | 0.24 |
| 30 – 40 | 1 – 25 | -1.23 ± 0.10 | -3.39 ± 0.25 | 0.42 |
| 22 – 30 | 1 – 25 | -1.57 ± 0.07 | -3.54 ± 0.18 | 0.29 |
| 9 – 11 | 1 – 23 | -1.20 ± 0.16 | -4.49 ± 0.37 | 0.60 |
| 6 – 14 | 1 – 25 | -1.09 ± 0.15 | -4.61 ± 0.36 | 0.60 |
| -4 – 10 | 1 – 25 | -0.95 ± 0.15 | -4.19 ± 0.38 | 0.63 |
| -6 – 0 | 1 – 25 | -1.12 ± 0.12 | -3.85 ± 0.29 | 0.49 |
| -13 – -7 | 1 – 25 | -1.14 ± 0.09 | -4.81 ± 0.22 | 0.36 |
| -31 – -13 | 1 – 27 | -1.29 ± 0.09 | -4.63 ± 0.22 | 0.37 |
| -39 – -31 | 1 – 25 | -1.07 ± 0.12 | -2.38 ± 0.29 | 0.48 |
| -44 – -36 | 1 – 25 | -0.80 ± 0.13 | -4.06 ± 0.33 | 0.55 |
| -60 – -40 | 1 – 24 | -0.98 ± 0.10 | -4.33 ± 0.24 | 0.40 |
| 10 – 50 | 28 – 70 | -3.09 ± 0.13 | 2.21 ± 0.46 | 0.11 |
| 40 – 60 | 26 – 50 | -3.14 ± 0.18 | 2.17 ± 0.67 | 0.18 |
| 30 – 40 | 27 – 50 | -2.82 ± 0.21 | 2.02 ± 0.78 | 0.19 |
| 22 – 30 | 27 – 60 | -3.06 ± 0.18 | 1.82 ± 0.66 | 0.24 |
| 9 – 11 | 25 – 48 | -2.95 ± 0.34 | 0.39 ± 1.22 | 0.32 |
| 6 – 14 | 27 – 60 | -3.26 ± 0.15 | 1.97 ± 0.57 | 0.21 |
| -4 – 10 | 27 – 60 | -3.48 ± 0.11 | 3.34 ± 0.40 | 0.14 |
| -6 – 0 | 27 – 52 | -3.44 ± 0.26 | 3.05 ± 0.94 | 0.25 |
| -13 – -7 | 27 – 60 | -1.96 ± 0.26 | -2.62 ± 0.99 | 0.36 |
| -31 – -13 | 29 – 60 | -2.60 ± 0.12 | -0.75 ± 0.47 | 0.15 |
| -39 – -31 | 27 – 66 | -3.82 ± 0.17 | 5.77 ± 0.66 | 0.28 |
| -44 – -36 | 27 – 60 | -2.79 ± 0.22 | 1.82 ± 0.82 | 0.30 |
| -60 – -40 | 26 – 54 | -2.61 ± 0.12 | 0.55 ± 0.46 | 0.15 |
| Longitude Range (°) | Planetary Wavenumber Range ^a | Slope | Intercept ($\ln P$) | Scatter ($\sigma_{\ln P}$) |
| -179 – 179 | 3 – 21 | -1.15 ± 0.47 | -1.16 ± 1.13 | 0.79 |
| -179 – 179 | 24 – 60 | -3.86 ± 0.39 | 8.46 ± 1.45 | 0.40 |

^a Twice the meridional wavenumber, for comparison to zonal fits.

fit ends two wavenumbers below the beginning of the high-wavenumber fit; we chose the point between the two fits by eye. We chose the other endpoint of the high-wavenumber fit where it appeared to depart from linearity, but not higher than planetary wavenumber 60 (see below). Since the noise should be the same everywhere on a given curve, the size of the scatter should be the same if the two portions of the curve were equally linear. However, the fits to the low-wavenumber regions have much larger scatter than the high-wavenumber fits on each plot, indicating poorer linearity. Further, the low-wavenumber slopes are almost never close to the predicted $-5/3$ energy-cascade pattern. In contrast, the high-wavenumber fits are quite close,

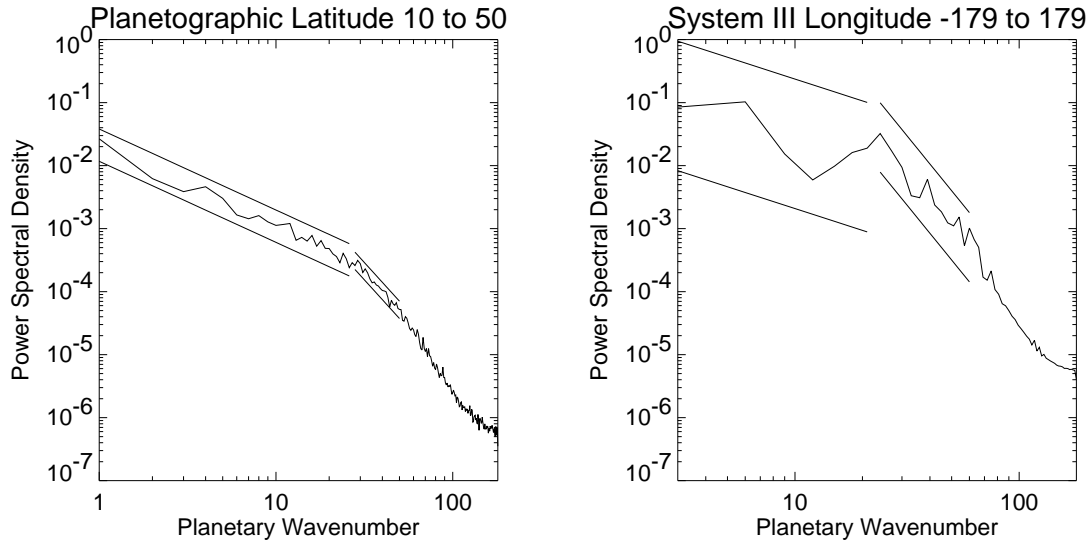


Fig. II.5. These plots show power spectra averaged over various planetary regions with linear fits in two wavenumber subranges. The line segments plotted adjacent to the data are 3 times the scatter, $\sigma_{\ln P}$, above and below the fitted segment; numerical values of the slope and error are given in Table II.II. The zonal spectra (left plot above and all plots on the following pages) show an m^{-3} power law between wavenumbers ~ 25 and ~ 50 . This is the power law of a turbulent enstrophy cascade and it indicates that there is no significant energy input to turbulence in this wavenumber region. The right plot above is a meridional spectrum averaged over all longitudes. It also shows a linear range in these wavenumbers, but the slope is -4.4 and the scatter is large.

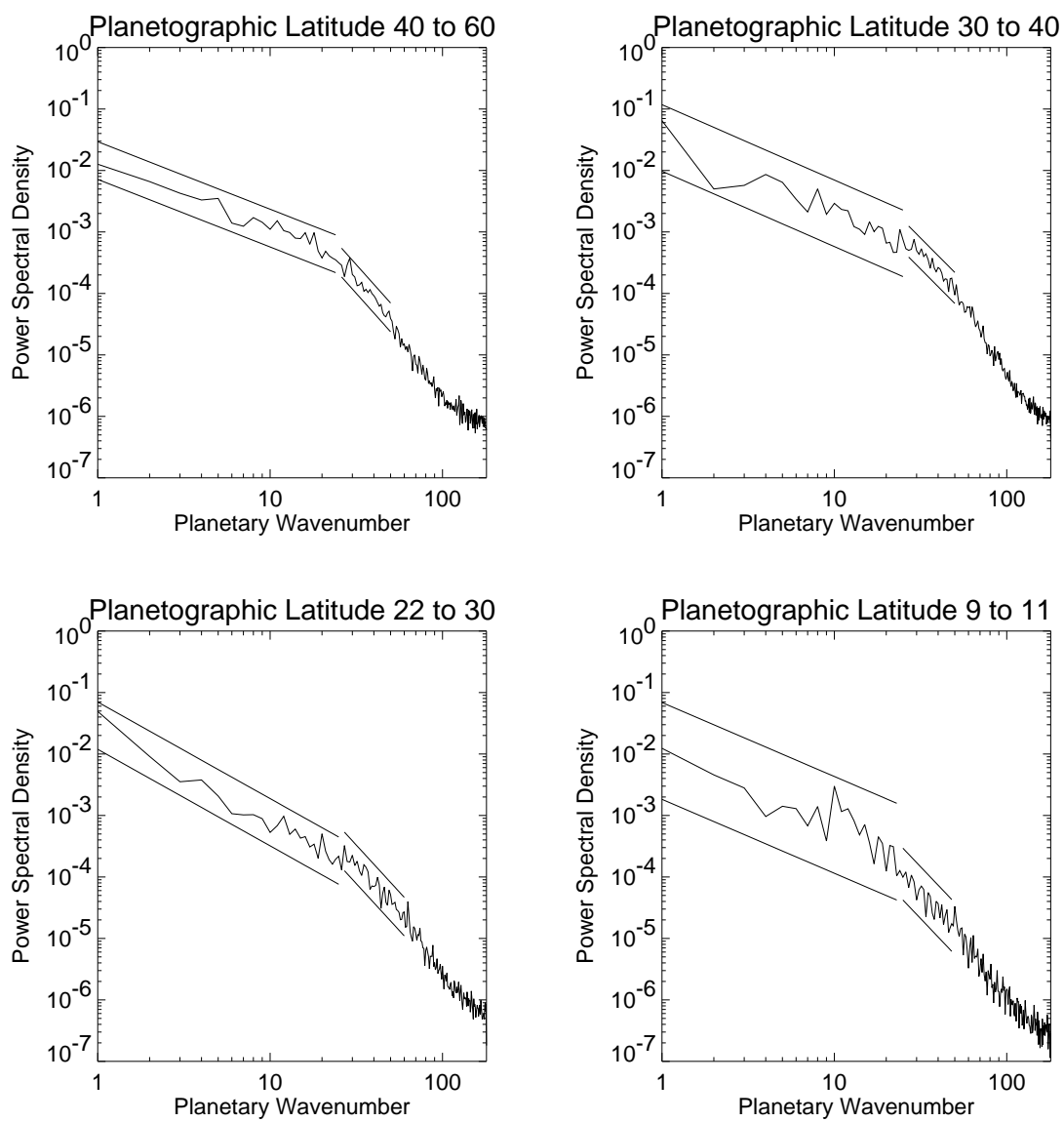


Fig. II.5—*Continued*

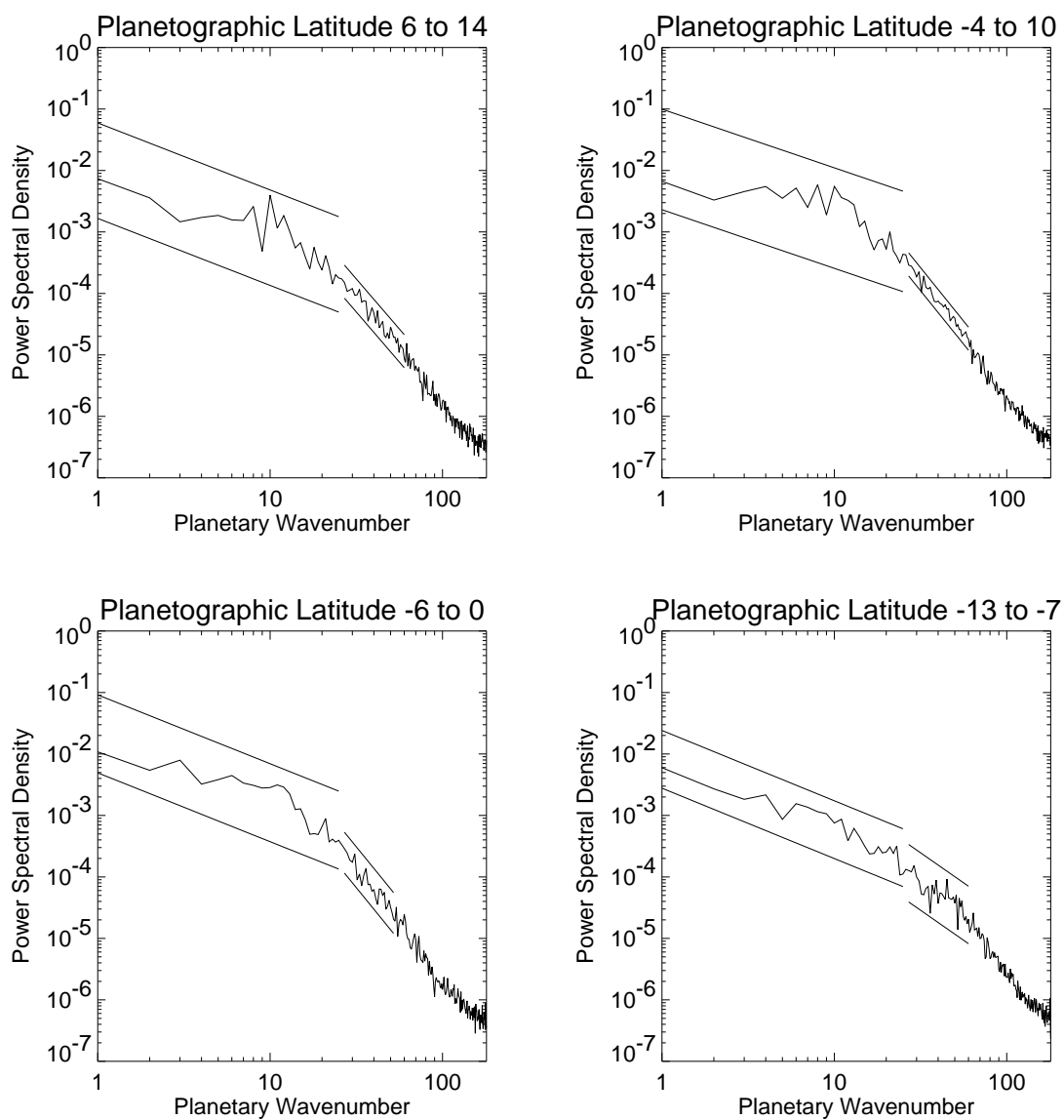


Fig. II.5—*Continued*

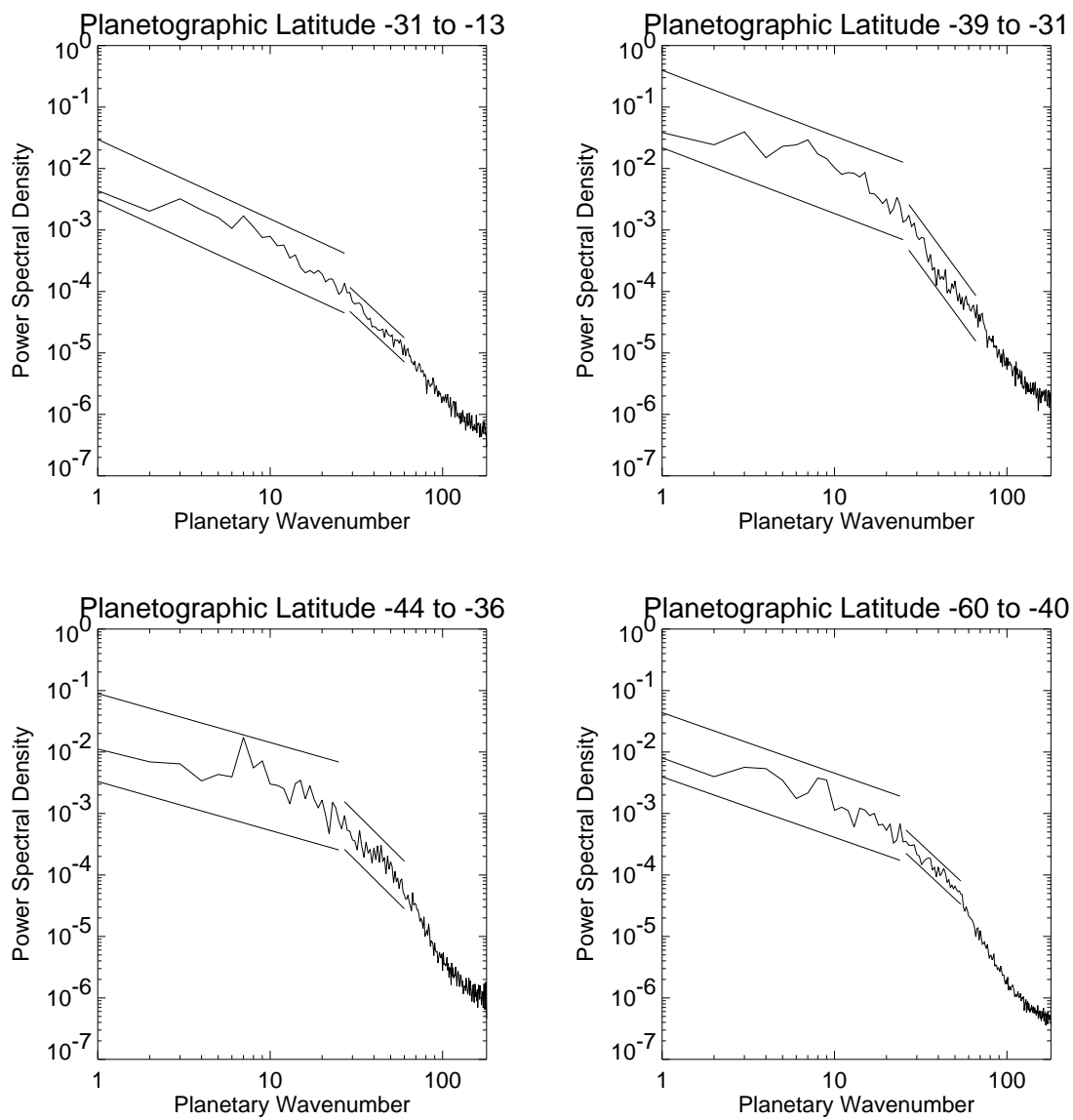


Fig. II.5—*Continued*

by atmospheric standards, to the predicted -3 enstrophy-cascade slope, except in the southern dark regions obscured by heavy clouds. The “grand average” fits (first in the list and first in Fig. II.5) include the latitudes north of this dark region.

Our fits support a lack of energy input between wavenumbers ~ 25 and ~ 50 , because any significant amount of added energy would cause cascades in both directions with the two power laws and would complicate the inertial subrange of cascading enstrophy. We do not see clear evidence for an inertial energy cascade.

Four parameters potentially affect the ends of the subranges. These are the image quality, the radius of deformation, the Rhines cascade-arrest scale, and the Rossby number. Fig. II.6 shows three of these parameters and where they appear relative to each other and the data.

First, image quality (atmospheric “seeing”, optical diffraction, telescope wind shake, tracking errors, etc.) places a fundamental limit on how small an object the images resolve. The full-width at half-maximum (FWHM) of the point-spread function (PSF) in this dataset is typically $0''.5$ – $0''.75$ and has a greater effect away from the sub-Earth point on the planet than near it. Seeing acts much like a Gaussian filter. To find its effect on power spectra, we convolved sine curves with Gaussian curves of the appropriate width. We find that at Jupiter’s equator a $0''.75$ FWHM PSF reduces the amplitude of the power spectrum at planetary wavenumber 60 by 50%. As latitude increases, this limit moves to lower wavenumbers, as shown in Fig. II.6A.

Second, if a cascade reaches sufficiently low wavenumbers, energy can propagate away in Rossby waves. This energy sink destroys a cascade's inertial character and terminates the linear portion of its power spectrum. The lower-limit wavenumber for turbulence in geostrophic systems is the Rhines cascade-arrest scale (Rhines 1979, Shepherd 1987),

$$k_\beta = \sqrt{\frac{\beta}{2U}}, \quad (\text{II.4})$$

where U is the horizontal wind scale, β is the local derivative of the vertical component of the Coriolis parameter, $f = 2\Omega \sin(\lambda)$, with respect to latitude λ , and Ω is the planetary rotation rate. By using the zonal-wind profile measured by Limaye (1986), and taking U to be half the range of wind speeds between minima in the profile, we find the k_β plotted in Fig. II.6B.

Third, the radius of deformation, L_d , is the principal length scale where fluctuations produced by baroclinic instability enter the dynamical system (Pedlosky 1987, p. 521), and we would expect energy input here if baroclinic instability were significant. The midlatitude terrestrial data in the left panel of Fig. II.4 show this input at $n = 6$. L_d for Jupiter is thought to be $\sim 3,000$ km in the stratosphere (Conrath *et al.* 1981) and less in the troposphere, though by how much is very uncertain. L_d is a reciprocal wavenumber and we have plotted three possible values in Fig. II.6C. Because of the proximity of the intermediate curve in panel C to the image-quality curve in panel A, we hesitate to assign the wavenumber cut-off to either effect (but see below).

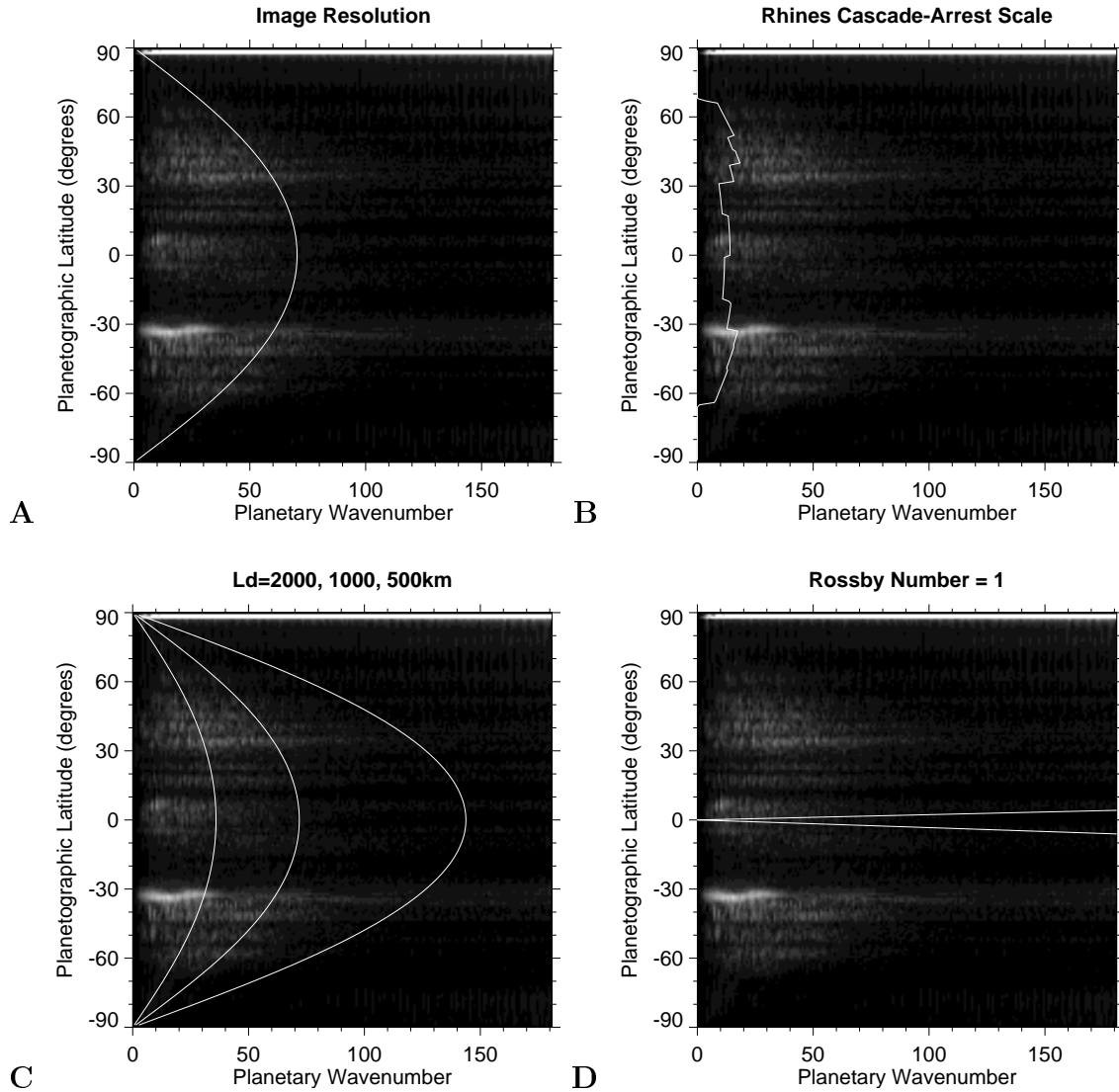


Fig. II.6. Scales that affect the spectra. In all panels, the horizontal scale is linear (not logarithmic) zonal planetary wavenumber, and the vertical scale is planetographic latitude. These are the same axes as the transform images in Fig. II.3, and each plot is superposed on the transform image of 22 March 1992 to show how the plotted limit relates to the data. Panel **A** shows the effect of image resolution on our sensitivity to high wavenumbers; because a circle of longitude is smaller at high latitude, our wavenumber sensitivity decreases there. Panel **B** shows the Rhines cascade-arrest scale, using the peak zonal wind in each latitude band as the velocity scale (see Eq. II.4). Panel **C** shows the location of three possible values of the deformation radius, L_d ; from left to right these are 2,000, 1,000, and 500 km. The proximity of the resolution and L_d curves makes drawing conclusions about the latter from these data risky. Panel **D** shows the wavenumber where the Rossby number equals unity; values are smaller poleward of the wedge and larger within it.

Finally, the quasi-geostrophic approximation, which involves the reduction to quasi-two-dimensional fluid dynamics, breaks down if

$$\epsilon = \frac{U}{fL} > 1, \quad (\text{II.5})$$

where ϵ is the Rossby number and L is the horizontal length scale. Figure II.6D shows the scale where $\epsilon=1$ on Jupiter using the same U as for k_β . We would not expect wavenumbers higher than this value at a given latitude to exhibit the -3 slope of an enstrophy cascade in quasi-two-dimensional turbulence.

These limits are all estimates rather than hard cut-offs, and a factor of 2 in accuracy is the best we can do for most of them (the image quality limit is somewhat better than this). We note that the spectra near the equator extend to lower wavenumbers than those near $\pm 30^\circ$ latitude. Our spatial resolution is best at the equator, and Fig. II.6A shows that we resolve these wavenumbers easily. However, as Fig. II.6D illustrates, the Rossby number is large in this region. Since the Coriolis parameter is zero here, the assumptions of geostrophic turbulence break down, and we expect different spectral behavior.

The spectra raise several interesting questions. Isotropy is a basic assumption of classical three-dimensional turbulence theories, but Jupiter's strong zonal flows violate this assumption. Shepherd (1987) addresses the degree to which the anisotropy of a zonal jet affects two-dimensional turbulent flow, and ties this to the Rhines scale.

The Rhines scale for Jupiter is near the typical width of a zonal jet, and the two may be causally related. That is, turbulence is confined within the jets and turbulent structures are not much larger zonally than a jet is meridionally. The only-slightly-elliptical shape of the smaller eddies supports this idea. Figure II.5 shows the steep and patterned meridional spectrum. We identify the peak of the linear range (whose slope is too steep to draw conclusions about its origin at this time) as the wavenumber equivalent to the undulation scale of the zonal wind profile, and we expect a turbulence cutoff wavenumber of $\sim 20\text{--}30$. This is what we see in the zonal spectra, and is consistent with the calculated Rhines scale, supporting the notion that the largest turbulent scale on Jupiter is the width of the jets.

Another question, which remains unresolved, is why we do not see a strong peak at wavenumber $1/L_d$. As stated previously, this is where we would expect the effects of baroclinic instability to enter the spectra, with a cascade away in each direction. Instead, we see a smooth enstrophy cascade at *lower* wavenumbers than the values of L_d proposed for the troposphere. Were this cascade to meet an energy cascade with the scale of L_d as the source, we would expect the two to disrupt each other. Does this mean that baroclinic instability is a relatively subdued process in Jupiter's troposphere? The location of the image quality curve near the center of the three possible L_d curves prevents us from resolving this question or from estimating L_d from these plots. We note, however, that a factor of 2 in improved spatial resolution would move the image quality limit well outside of where our data show power. If such improved data showed the same spectrum as we present here, we would then

be able to address the question of L_d directly from the spectra. If the region where power appears in such new spectra were to extend to the wavenumber limit of its image quality, we would be confident that we did not detect any effects of L_d in these data. That could, in turn, constrain the level of baroclinic instability.

Chapter 5

WAVE SEARCH

In addition to exploring patterns in the power spectra, we would also like to identify any discrete global periodic structure such as Rossby waves. The hallmark of a Rossby wave is the meridional undulation of a prevailing zonal wind (see Appendix D). We envision two ways that such an undulation could manifest itself in our data. First, since the zonal winds correspond well with the banded cloud structure (Limaye 1986), a Rossby wave near the edge of a bright or dark band could give rise to a meridional undulation in the location of the edge. Second, since the dynamical thickness of the weather layer containing a Rossby wave varies with the phase of the wave, the local cloud thickness could vary as well, giving rise to an undulating light pattern at a given latitude. Such oscillations are given by the perturbation streamfunction in the dispersion relation derivation of Appendix D.

Studying the undulations of the cloud belts at first appears promising. Jupiter's

banded cloud patterns, provide many regions where clouds end abruptly, so any Rossby waves strong enough to influence these cloud borders should show up as wiggles in the otherwise-straight interface between a cloud belt and a clear zone. There are other effects that would cause such undulation in an interface, however, including passing eddies and the spread of convected material. Errors in mosaicking and finding the planetary center would further contaminate an edge location analysis. Because of these difficulties, we concentrated on the second approach, looking for wave-like intensity variations at a given latitude. The waves in which we are most interested are global in extent and have relatively low wavenumbers.

Waves would appear as discrete, bright regions in transform amplitude. Unfortunately, other than the plumes, there are no such features that appear on more than three of the six nights with full longitude coverage. There are also no consistent sets of strong, discrete features at the same wavenumber but different latitudes; such a collection of features would support the banana-cell convection of Hart *et al.* (1986a,1986b). That we see no such pattern indicates that if the convection underlying the atmosphere follows the banana-cell pattern, any resulting variation in cloud opacity is too weak for us to detect.

Except for the plumes, periodic features do not zonally girdle the planet in any of the maps. However, there is one local periodic pattern, a series of brightenings in the narrow band at -9° latitude with an apparent wavenumber of about 50. The pattern is usually distinct only in a restricted area, and is most distinct on 22 Mar., our night

of best seeing. Since two or more nearby wavenumbers can create an interference pattern that appears strongly in one location and is absent elsewhere, we attempted to locate the pattern in the transform images. The feature appears at wavenumber 50 on 22 Mar., but is completely absent on all the other nights. Further investigation of the maps shows that the distances between brightenings is more regular on 22 Mar. than on the other nights when the pattern is visible. We conclude that, although there may be some wave action involved in generating the pattern, its transitory nature precludes a simple interpretation.

Since a linear plane wave mode propagates with a uniform speed, we would expect its phase in a Fourier transform to change at a uniform rate. We thus performed linear least-squares fits to the transform phases as a function of time, one six-point fit for each of the 32,000 pixels in the transform phase images. By making an image of the fit errors (see Fig. II.7), we can see where regions of sensible fits occur. If a sensible fit were to correspond to a wavenumber and latitude with significant amplitude, it would indicate a feature with a regular motion around the planet and the slope of the fit would give the rate of motion. This method is only sensitive to slowly-moving features situated fortunately enough that their phases do not cross the periodic phase boundary over a period of 70 days. For $m=1$ waves at the equator, the maximum speed is 11.8 m/s; for $m=2$ half that, etc. Thus, the technique is only useful for long waves that move slowly in System III, but these are the ones in which we are most interested. Eq. II.3 indicates that we could find waves up to $m \approx 6, n = 0$. In the fit error plot of Fig. II.7, all of the regions of good fit correspond to discrete spot

Phase Fit Errors

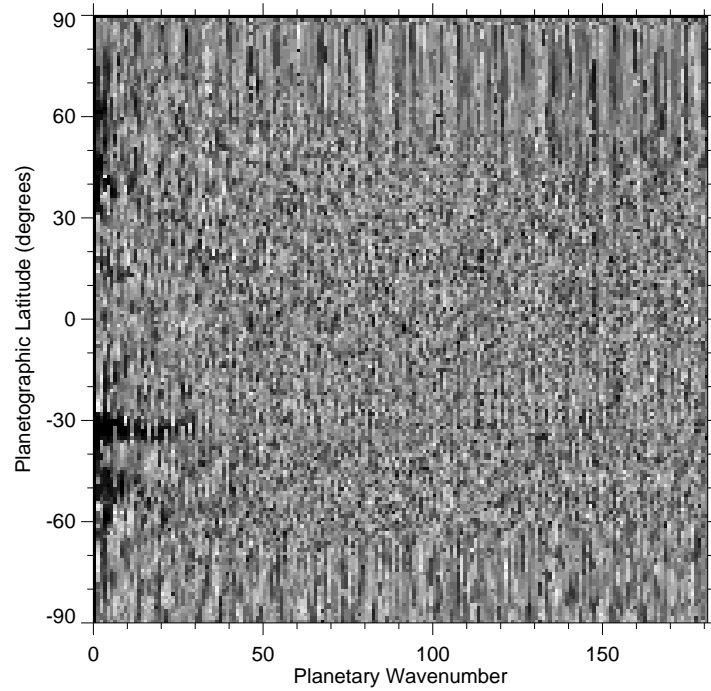


Fig. II.7. By fitting a line to the phases of our zonal FFT images as a function of time, we searched for particularly slowly-moving features. This image of the errors has the same coordinates as the FFT amplitude plots of Fig. II.3. The dark regions at low wavenumber look promising, but each matches to a previously-known feature on the planet, such as the Great Red Spot or the discrete bright feature at -32° . The vertical stripes correspond to high-wavenumber noise due to compositing the mapped images.

features, except that associated with the plumes. No other slowly-moving periodic features are apparent. We also examined the phase differences between the two adjacent full-coverage nights, 27 and 28 Feb., concentrating on regions where the transform amplitudes are largest. Except for the plumes, the phase differences of the large-amplitude features all correspond to wave speeds significantly higher than that of the local zonal wind, which indicates to us that they are not due to wave propagation.

With no detection of a propagating wave feature other than the equatorial plumes, we set an upper detection limit according to the RMS (root mean square) fluctuation of the signals in the transform amplitude images and reverse the modifications to arrive at limits in terms of map intensity values. To test the limits, we selected several latitude/wavenumber combinations, inserted sine waves with the amplitude of our limiting values into the mapped images, and re-created the transform images to determine if the wave would have attracted our attention. We find that regions in the transform amplitude images standing three times the local RMS fluctuation above the mean would definitely have attracted attention, as would single pixels standing 5 RMS above the mean. Since the mean map pixel value (see Fig. II.2) varies with latitude, so does the sensitivity. Likewise, the sensitivity increases for larger wavenumbers.

Figure II.8 shows the RMS signal fluctuation in a normalized, flattened transform amplitude plot. One can see how little variation there is after the normalization and

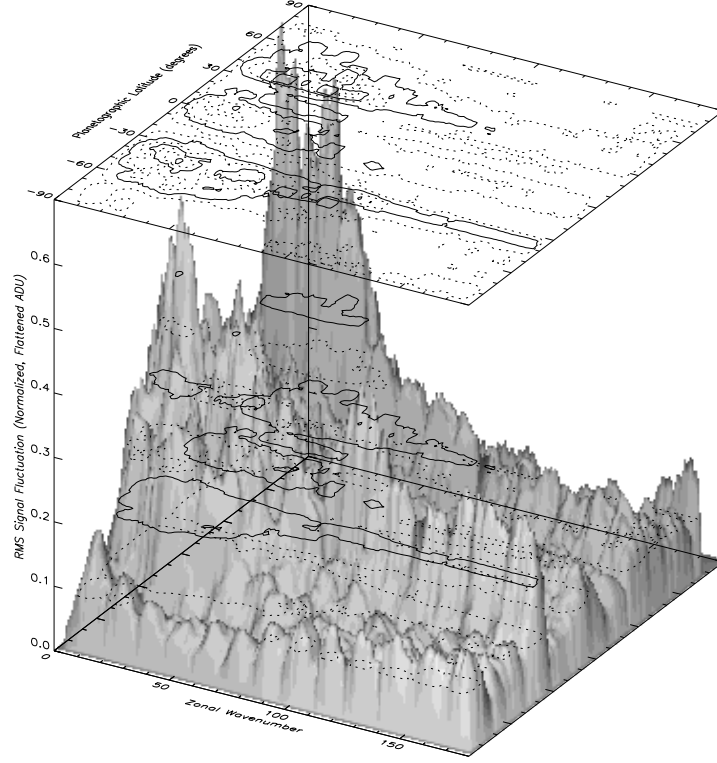


Fig. II.8. Root-mean-square signal fluctuation in the normalized, flattened zonal FFT of 22 March 1992 (see Fig. II.3).

empirical “flattening.” If the data contained any discrete planetary-scale waves they would stand out as tall spikes in this plot. Figure II.9 presents the level of a $3\text{-}\sigma$ detection limit in terms of image intensity. One can determine the wave amplitude sensitivity for a given planetary wavenumber, m , and latitude, λ , in the following manner: on the top (planar) contour plot on top of the cube in Fig. II.9, find the contour closest to the (m, λ) pair. Move down onto the surface plot to find where this contour lies in relation to sensitivities nearby, and read horizontally to the vertical axis to read the sensitivity in ADU. If a wave were constrained to $1\text{--}3^\circ$ of latitude and $1\text{--}3$ wavenumbers, we would expect to detect it at this level.

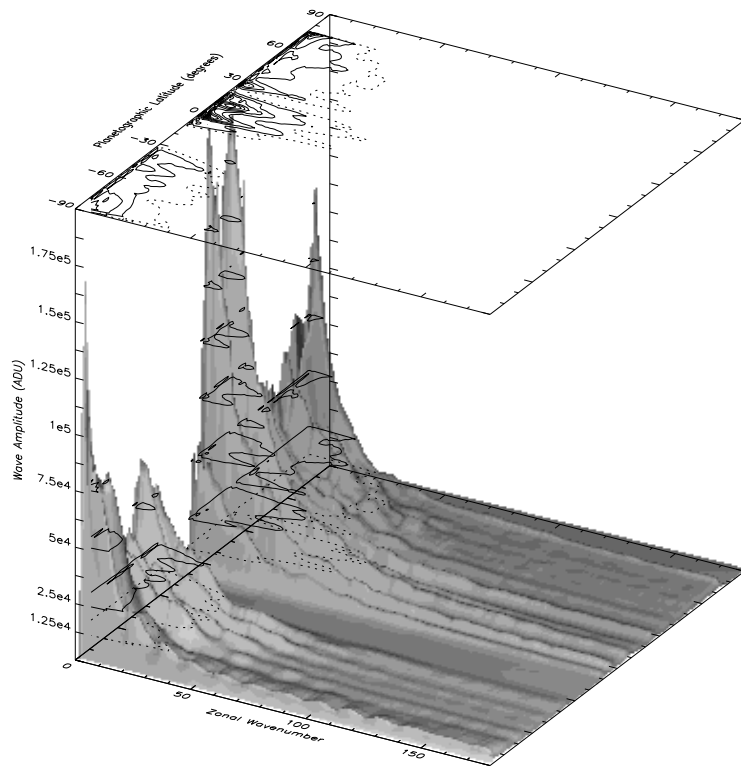


Fig. II.9. Limits to sensitivity as a function of wavenumber and latitude.

Chapter 6

CONCLUSIONS

The first search for tropospheric, planetary-scale waves on Jupiter, conducted by Magalhães *et al.* (1989, 1990) and based on rasterizing Voyager IRIS data, did not detect waves in the 5- μm wavelength region. That study did find periodic thermal features in the upper troposphere and both it and the study by Deming *et al.* (1989) detected slowly-moving thermal features in the stratosphere. With a factor of ten improvement in linear spatial resolution and twice the temporal coverage, we, too, have found no heretofore-unknown features at this wavelength, though we easily detect the equatorial plumes, which Magalhães *et al.* did not.

Our null wave search leaves unresolved the issue of how the slowly-moving stratospheric thermal features are tied to the internal rotation rate of the planet. Barring an interaction between the magnetosphere and the stratosphere, these waves must be connected to the deep interior through the troposphere, for it is unlikely that they

would be in the rest frame of the interior by chance. Similarly, we cannot address the effect of interior convection patterns on the troposphere, other than to say that, except for the equatorial plumes, we do not detect an effect that is consistent with wave propagation above our detection limits for cloud opacity fluctuations.

Although the appearance of Jupiter did not change on a large scale in our 99 days of observation, its appearance at $4.9\text{ }\mu\text{m}$ has been markedly different in other years. We have seen, for example, images at this wavelength where the rim of the GRS is very bright and where the entire latitude band of the GRS is among the brightest and most active on the planet, rather than the darkest. It is possible that the dynamics that cause changes in cloud distribution could also excite wave activity, so it may be worthwhile to perform this search one or more additional times, particularly when Jupiter's appearance is changing. Our investigation sampled regularly for just over three months. Were we to repeat the observations during a time of change, we would propose a different temporal sampling, with 3–4-day blocks of observing time separated by no more than 10 days over 2 months. The longer time in each block would be sensitive to the action of the zonal wind and would better characterize day-to-day changes. It would also be better suited to using phase information to constrain faster wave propagation than the 2-night pairs of the present program. The shorter gaps between observing blocks would reduce the chances of losing a wave's phase information in the midst of large-scale changes on the planet. Because of the desirability of applying Fourier techniques to naturally-periodic data, we would also avoid planning observations without the ability to cover all longitudes each night.

The main impediment to finding waves in this dataset is the high degree of other activity in Jupiter’s atmosphere. The plumes, vortices, and turbulent zones evident in visible-light images obscure any wave structure that may exist at a less intense level. Any new technique must better discern a weak signal underneath a strong one in order to find global wave patterns at this wavelength. Because of several difficulties with the present technique, we would not perform this investigation again without one of several improvements to the observing technique, as outlined below.

Perhaps the largest limit to the sensitivity of our Fourier approach, and one that significantly reduced the number of Jupiter images and prolonged the analysis, was the requirement of mosaicking and the time it took to do so. Thermal emission from the Earth’s atmosphere dominates the signal from Jupiter in the 5- μm region, and the emission level and pattern change during the time of an imaging sequence. Simple object-sky image differences do not produce consistent background levels. Interpolating sky frames in time and adjusting background levels so that neighboring images match does give a first-order correction for sky-level fluctuations, but the spatial variation of the thermal background is not uniform over the image, and some irreconcilable differences do remain. They are particularly apparent in the central piece(s) of the mosaics, which are harder to match to their neighbors because they contain no sky. Mosaicking also introduces small errors in the locations of some pieces, and these translate into an error in the location of the planetary center. While 1-pixel mosaicking and centering errors are uncommon, they do occasionally occur. Their combined effect at the edges of the map sections we used (up to 60°

from the image center) is a position error of $\sim 4^\circ$. The effect of these two types of errors is noise patterns in the transform amplitudes, which reduces their sensitivity to weak signals. Full-planet images do not suffer from these problems. In addition, the lack of mosaicking errors would make an analysis of the edges of cloud belts for meridional deviations feasible. We note that the IRTF recently introduced a new infrared camera, NSFCAM (Shure *et al.* 1994), with a 256×256 array that is capable of imaging the whole planet and of taking extremely short exposures in rapid succession.

A further limit to sensitivity is scattered light, which could be masking small variations at all brightness levels. A combination of reduced scattered light and improved spatial resolution, both by at least an order of magnitude, might render weaker signals detectable. Future space-based infrared cameras have the potential for making these improvements, provided that their optical designs limit internal scattered light. Were this project to be undertaken by a Jupiter-orbiting spacecraft with an infrared camera, its primary benefits would be essentially eliminating the effects of scattered light while vastly increasing spatial resolution.

Our spectral analysis found a power law relationship between wavenumbers ~ 25 and ~ 50 ; the fitted exponent is -3.09 ± 0.13 . If the correspondence between the power spectra of kinetic energy and cloud intensity holds for Jupiter, then we suggest that we have detected enstrophy cascading to higher planetary wavenumbers with a power law near the theoretical -3 in the stated inertial subrange at most latitudes where

the images are bright. As expected, the low-wavenumber cutoff of the linear range corresponds closely with the representative wavenumber of the belts and zones. This indicates that zonal turbulent length scales do not much exceed the width of a given zonal jet. The presumed input scale of baroclinic instability is the Rossby deformation radius, L_d , which is slightly below our image resolution. The lack of an energy cascade from this scale may indicate that baroclinic instability is not an important process on Jupiter. Doubling the image quality in an otherwise-similar study would lay this question to rest.

ACKNOWLEDGEMENTS

We thank the IRTF Time Allocation Committee for their generous allotment of telescope time, and P. Stone, G. Orton, and A. Ingersoll for helpful discussions. Special thanks go to IRTF Division Chief R. Joseph, Telescope Operators D. Griep, C. Kaminski, W. Golisch, and Programmers T. Denault and E. Pilger for their patience and assistance with the changes that made full automation at the telescope possible. Analysis work was funded by NASA Planetary Atmospheres grant NAGW-2956.

REFERENCES

- ALLISON, M. 1990. Planetary Waves in Jupiter's Equatorial Atmosphere. *Icarus* **83**, 282–307.
- BARON, R., J. E. P. CONNERNEY, T. SATOH, T. OWEN, AND J. HARRINGTON 1994. Variability of Jupiter's H_3^+ Aurorae. Submitted to *Nature*.
- BRACEWELL, R. N. 1986. *The Fourier Transform and Its Applications*, 2nd ed., revised. McGraw-Hill, New York.
- CHARNEY, J. G. 1971. Geostrophic Turbulence. *J. Atmos. Sci.* **28**, 1087–1095.
- CONNERNEY, J. E. P., R. BARON, T. SATOH, AND T. OWEN 1993b. Images of Excited H_3^+ at the Foot of the Io Flux Tube in Jupiter's Atmosphere. *Science* **262**, 1035–1038.
- CONRATH, B. J., P. J. GIERASCH, AND N. NATH 1981. Stability of Zonal Flows on Jupiter. *Icarus* **48**, 256–282.
- DANILOV, S. D. F. V. DOLZHANSKII, AND V. A. KRYMOV 1994. Quasi-two-dimensional hydrodynamics and problems of two-dimensional turbulence. *Chaos* **4**, 299–304.

- DEMING, D., M. J. MUMMA, F. ESPENAK, D. E. JENNINGS, T. KOSTIUK, G. WIEDEMANN, R. LOEWENSTEIN, AND J. PISCITELLI 1989. A Search for p -Mode Oscillations of Jupiter: Serendipitous Observations of Nonacoustic Thermal Wave Structure. *Astrophys. J.* **343**, 456–467.
- DOWLING, T. E. 1993. A Relationship between Potential Vorticity and Zonal Wind on Jupiter. *J. Atmos. Sci.* **50**, 14–22.
- DOWLING, T. E. 1994. Successes and failures of shallow-water interpretations of Voyager wind data. *Chaos* **4**, 213–225.
- DOWLING, T. E. 1995. Dynamics of Jovian Atmospheres. *Annu. Rev. Fluid Mech.* **27**, 293–334.
- DOWLING, T. E., AND A. P. INGERSOLL 1988. Potential Vorticity and Layer Thickness Variations in the Flow around Jupiter’s Great Red Spot and White Oval BC. *J. Atmos. Sci.* **45**, 1380–1396.
- DOWLING, T. E., AND A. P. INGERSOLL 1989. Jupiter’s Great Red Spot as a Shallow Water System. *J. Atmos. Sci.* **46**, 3256–3278.
- ERTEL, H. 1942. Ein neuer hydrodynamischer Wirbelsatz. *Meteorolog. Zeitschrift* **59**, 277–281.
- FLASAR, F. M., AND P. J. GIERASCH 1986. Mesoscale Waves as a Probe of Jupiter’s Deep Atmosphere. *J. Atmos. Sci.* **43**, 2683–2707.
- GAUTIER, D., B. CONRATH, M. FLASAR, R. HANEL, V. KUNDE, A. CHEDIN, AND N. SCOTT 1981. The helium abundance of Jupiter from Voyager. *J. Geophys. Res.* **86**, 8713–8720.

- GODFREY, D. A. 1988. A Hexagonal Feature around Saturn's North Pole. *Icarus* **76**, 335–356.
- HARRINGTON, J., R. P. LeBEAU, K. A. BACKES, AND T. E. DOWLING 1994. Dynamic response of Jupiter's atmosphere to the impact of comet Shoemaker-Levy 9. *Nature* **368**, 525–527.
- HART, J. E., G. A. GLATZMAIER, J. TOOMRE 1986a. Space-laboratory and numerical simulations of thermal convection in a rotating hemispherical shell with radial gravity. *J. Fluid Mech.* **173**, 519–544.
- HART, J. E., J. TOOMRE, A. E. DEANE, N. E. HURLBURT, G. A. GLATZMAIER, G. H. FICHTL, F. LESLIE, W. W. FOWLIS, AND P. A. GILMAN 1986b. Laboratory Experiments on Planetary and Stellar Convection Performed on Spacelab 3. *Science* **234**, 61–64.
- HOLTON, J. R. 1992. *An Introduction to Dynamic Meteorology*, 3rd ed. Academic Press, p. 217.
- INGERSOLL, A. P. 1973. Jupiter's Great Red Spot: A Free Atmospheric Vortex?. *Science* **182**, 1346–1348.
- INGERSOLL, A. P., AND P. G. CUONG 1981. Numerical Model of Long-Lived Jovian Vortices. *J. Atmos. Sci.* **38**, 2067–2076.
- INGERSOLL, A. P., H. KANAMORI, AND T. E. DOWLING 1994. Atmospheric gravity waves from the impact of comet P/Shoemaker-Levy 9 with Jupiter. *Geophys. Res. Lett.* **21**, 1083–1086.
- KUNDU, P. J. 1990. *Fluid Mechanics*. Academic Press.

- LIMAYE, S. S. 1986. Jupiter: New Estimates of the Mean Zonal Flow at the Cloud Level. *Icarus* **65**, 335–352.
- LINDAL, G. F., G. E. WOOD, G. S. LEVY, J. D. ANDERSON, D. N. SWEETNAM, H. B. HOTZ, B. J. BUCKLES, D. P. HOLMES, P. E. DOMS, V. R. ESHLEMAN, G. L. TYLER, AND T. A. CROFT 1981. The Atmosphere of Jupiter: An Analysis of the Voyager Radio Occultation Measurements. *J. Geophys. Res.* **86**, 8721–8727.
- MAGALHÃES, J. A., A. L. WEIR, B. J. CONRATH, P. J. GIERASCH, AND S. S. LEROY 1989. Slowly moving thermal features on Jupiter. *Nature* **337**, 444–447.
- MAGALHÃES, J. A., A. L. WEIR, B. J. CONRATH, P. J. GIERASCH, AND S. S. LEROY 1990. Zonal Motion and Structure in Jupiter’s Upper Troposphere from Voyager Infrared and Imaging Observations. *Icarus* **88**, 39–72.
- MARCUS, P. S. 1988. Numerical simulations of Jupiter’s Great Red Spot. *Nature* **331**, 693–696.
- ORTON, G. S., A. J. FRIEDSON, J. CALDWELL, H. B. HAMMEL, K. H. BAINES, J. T. BERGSTRALH, T. Z. MARTIN, M. F. MALCOM, R. A. WEST, W. F. GOLISCH, D. M. GRIEP, C. D. KAMINSKI, A. T. TOKUNAGA, R. BARON, AND M. SHURE 1991. Thermal Maps of Jupiter: Spatial Organization and Time Dependence of Stratospheric Temperatures, 1980 to 1990. *Science* **252**, 537–542.
- PEDLOSKY, J. 1987. *Geophysical Fluid Dynamics*, 2nd ed. Springer Verlag.
- PRESS, W. H., S. A. TEUKOLSKY, W. T. VETTERLING, AND B. P. FLANNERY 1992. *Numerical Recipes in C: The Art of Scientific Computing*, 2nd ed. Cambridge University Press, pp. 408–412.
- RHINES, P. B. 1979. Geostrophic Turbulence. *Ann. Rev. Fluid Mech.* **11**, 401–441.

- SHEPHERD, T. E. 1987. Rossby waves and two-dimensional turbulence in a large-scale zonal jet. *J. Fluid Mech.* **183**, 467–509.
- SHURE, M., D. W. TOOMEY, J. RAYNER, P. ONAKA, A. DENAULT, W. STAHLBERGER, D. WATANABE, K. CRIEZ, L. ROBERTSON, D. COOK, AND M. KIDGER 1994. A Powerful New Infrared Array Camera for the NASA Infrared Telescope Facility. In *Infrared Astronomy with Arrays*, I. McLean, ed, pp. 395–398.
- SMITH, B. A., L. A. SODERBLOM, R. BEEBE, D. BLISS, J. M. BOYCE, A. BRAHIC, G. A. BRIGGS, R. H. BROWN, S. A. COLLINS, A. F. COOK II, S. K. CROFT, J. N. CUZZI, G. E. DANIELSON, M. E. DAVIES, T. E. DOWLING, D. GODFREY, C. J. HANSEN, C. HARRIS, G. E. HUNT, A. P. INGERSOLL, T. V. JOHNSON, R. J. KRAUSS, H. MASURSKY, D. MORRISON, T. OWEN, J. B. PLESCIA, J. B. POLLACK, C. C. PORCO, K. RAGES, C. SAGAN, E. M. SHOEMAKER, L. A. SROMOVSKY, C. STOKER, R. G. STROM, V. E. SUOMI, S. P. SYNNOTT, R. J. TERRILE, P. THOMAS, W. R. THOMPSON, AND J. VEVERKA 1986. Voyager 2 in the Uranian System: Imaging Science Results. *Science* **233**, 43–64.
- SROMOVSKY, L. A., H. E. REVERCOMB, R. J. KRAUSS, AND V. E. SUOMI 1983. Voyager 2 Observations of Saturn’s Northern Mid-Latitude Cloud Features: Morphology, Motions, and Evolution. *J. Geophys. Res.* **88**, 8650–8666.
- TODY, D. 1986. The IRAF data reduction and analysis system. In *Instrumentation in Astronomy VI* (D. L. Crawford, Ed.) Proc. SPIE, Vol. 627, p. 733.
- TOOMEY, D. W., M. SHURE, E. M. IRWIN, AND M. E. RESSLER 1990. ProtoCAM - An innovative IR Camera for Astronomy. In *Instrumentation in Astronomy VII*

- Proc. SPIE, Vol. 1235, pp. 69–81.
- TRAVIS, L. D. 1978. Nature of the Atmospheric Dynamics on Venus from Power Spectrum Analysis of Mariner 10 Images. *J. Atmos. Sci.* **35**, 1584–1595.
- VEVERKA, J., J. GOGUEN, S. YANG, AND J. ELLIOT 1978. Scattering of Light from Particulate Surfaces I. A Laboratory Assessment of Multiple-Scattering Effects. *Icarus* **34**, 406–414.
- WAINSCOT, R. J., A. PICKLES, M. NEEDHAM, K. MAESATO, AND R. ELLER 1992. Changes and acquisitions for the 2.2m telescope. In *Mauna ‘ikena*. Institute for Astronomy, U. of Hawaii, Honolulu, HI 96822. May 1992, pp. II–IV.
- WILLIAMS, G. P., AND R. J. WILSON 1988. The Stability and Genesis of Rossby Vortices. *J. Atmos. Sci.* **45**, 207–241.

Appendix A

NOTES ON OBSERVING TECHNIQUE

During these observations, two classes of changes to the IRTF's regular procedures produced a significant improvement in image quality and data rate. The first class addressed "dome seeing" and the second involved automation of repeated sequences of telescope motions and camera actions.

The idea of dome seeing is not new; it simply states that a large component of atmospheric image blur is caused by thermal disequilibrium between the solid parts of the observatory, the air in the dome, and the air outside. Nevertheless, many observers fail to take steps that reduce the effect dramatically. The simple procedure listed below cools the dome and telescope quickly and replaces the warm dome air with cooler night air. They also keep a strong, steady airflow pattern through the telescope and dome, which prevent interior convection cycles from becoming established. The steps used at the IRTF for the 1992 observations were:

1. Go to the dome early to allow a longer thermal equilibration period. Ideally, the instruments should always be cold and the other procedures should start when the external temperature is lower than the internal temperature.
2. Fill the instrumentation with cryogenics immediately upon arrival at the dome.
3. Open the dome shutter, the inner and outer doors to the loading dock, and the mirror covers. This allows air exchange, and brings cool air past the warm telescope and mirror.
4. Close the insulating control-room window shade as far as possible.
5. Turn on the mirror cooling fan. The fan draws air across the primary mirror and through the Cassegrain hole. A smooth airflow pattern replaces any turbulent convection patterns above the mirror and cools the mirror faster. Needless to say, vibrations from this fan must not shake the telescope. This idea is from R. Baron.
6. Focus early and often. At the IRTF, significant focus changes during a night are common, and can increase the size of a point source by a factor of two or more. A possible source for these fluctuations is changes in the length of the steel structure separating the primary and secondary mirrors. Thermal expansion and contraction of the structure by a few millimeters causes the focus to change by larger amounts because of the high focal ratio of the secondary. Check focus especially after any changes in dome temperature or seeing.
7. If object availability permits, do whatever calibrations are possible at the be-

ginning of the night, while thermal equilibration is still in progress. They are usually less affected by poor image quality than are object observations.

During the 1992 runs, these simple steps reduced the typical point-spread function from $\sim 1''$ to $\sim 0.5''$ on most nights and to half that on the best nights. The diffraction limit for the IRTF at $4.9\text{ }\mu\text{m}$ is $0.13''$, and at the time there were some aberrations in the optics. The refurbishment project presently underway at the IRTF will install large cooling fans and more insulation to address dome seeing issues, and a tip-tilt secondary mirror to reduce image degradation by atmospheric turbulence. However, observers will still need to carry out some of the steps outlined above to get the best images possible.

The second major improvement over standard procedures was the automation of imaging sequences. Modern digital array cameras are remotely controlled by computers, as are the control systems of large telescopes. Frequently the operator never touches the camera once it is turned on at the beginning of the night. The use of computers to control cameras brings with it the possibility of programming repeated sequences in advance. For many routine observations, a fully-featured automatic mode can significantly decrease the time required to do the observations and shrink the number of opportunities for operator error. The 1992 mosaicking observations consisted largely of intricate but absolutely identical data acquisition sequences. Taking each mosaic entailed:

1. Setting 13 observing parameters (exposure time, number of readouts, number of cycles between star and sky positions, filter type, wavelength, etc.) to the values appropriate to the sequence. There were three sets of parameters, one for the aurora project's 3×3 mosaics at $3.4\text{ }\mu\text{m}$ and one each for the 3×3 and 4×4 mosaics at $4.9\text{ }\mu\text{m}$ for the present work.
2. Centering Jupiter on a video monitor with an acquisition camera and guide paddle.
3. Removing the acquisition camera pick-off mirror from the beam.
4. Moving the telescope to the position of the first image.
5. Taking an image of part of Jupiter.
6. Moving to the sky location (usually $120\text{--}240''$ away).
7. Taking an image of the sky.
8. Possibly repeating the previous 4 items several times if using long total exposures.
9. Moving to the position of the next image.
10. Repeating the last 5 items a total of 9 or 16 times.
11. Moving to the center of Jupiter.
12. Inserting the acquisition camera pick-off mirror into the beam.

When done manually, most of these items took only a few seconds. However, telescope motions by hand are done by means of position readouts on a monitor and a guide paddle with buttons for motion in the four cardinal directions. The telescope's inertia makes fast motions inaccurate. The instrument's manual mode already did the beam switching between object and sky, and the cycling for long exposures. At peak manual efficiency, the 3×3 mosaics took ~ 12 minutes at $4.9\text{-}\mu\text{m}$ and ~ 16 minutes at $3.4\text{-}\mu\text{m}$.

The ProtoCAM software allowed most commands to be taken from a file. While not a programming language, these files made it possible to batch the repeated operations. There was also an automated mosaic mode, though it only handled up to 3×3 mosaics. The IRTF staff was helpful in providing several additional commands necessary to batch 4×4 mosaics. The most significant of these improvements was the ability to command the telescope control system (TCS). When fully automated, time for 3×3 mosaics at $4.9\text{ }\mu\text{m}$ dropped from ~ 12 minutes to 7, and time for $3.4\text{-}\mu\text{m}$ mosaics of this size dropped from ~ 16 minutes to 13. The new features made telescope offsets and additional image buffers available and thus enabled automated 4×4 mosaics. Within a short time the only manual steps for taking a mosaic were centering the planet, removing the pick-off mirror, typing the command file name, and inserting the mirror after the exposures were finished. The key change in thinking was that instead of having a batch file that merely ran the camera system, the observer now had control of telescope motions as well, and could coordinate these with filter and readout operations.

The advantages of this approach were greater than just the 13–36% of cycle time saved. Exposure times for these observations were only 10–30 sec. Manual motion between images thus required the operator’s constant concentration, either moving the telescope as accurately as possible or watching for the end of the exposure. Twelve hours of such work at an altitude of 4,200 meters is mentally demanding, and is prone to mistakes. Alternating between two observers was the only way to maintain continuous observations with high efficiency. On the other hand, automated observing required attention only every 7–13 minutes, which is ample rest time between actions. A single observer had time to attend to other tasks, such as preparing for a sequence of standard stars or preliminary analysis of the data. Use of command files would also make observations for long-term monitoring programs easier: the researchers could give a command file to the telescope staff and arrange for an operator to run it after centering the object of study. The researchers would know that their exact instructions were being followed and the operator would have minimal work to do, even for a complex sequence of images, filters, and offsets. Both of the last two benefits result directly in reduced travel and personnel needs, and thus lower cost.

Appendix B

AUTOMATIC MOSAIC ASSEMBLY

The small number of pixels in early infrared arrays, especially those sensitive to thermal wavelengths, required a sacrifice of either the spatial resolution or the angular coverage to which observers had grown accustomed with CCD systems. A common infrared camera design compromise was to sacrifice a small amount of resolution, so that the majority of stellar and many planetary observations were possible in the chip's field, and to require mosaicking of larger extended sources. The angular resolution sacrifice was not large: on Mauna Kea, where a typical CCD system might have an image scale of $0''.07 - 0''.2/\text{pixel}$ (Wainscoat *et al.* 1992), infrared detectors are often operated with resolutions as large as $0''.35/\text{pixel}$ (ProtoCAM) and $0''.4/\text{pixel}$ (U. of Rochester camera). Some infrared cameras introduced multiple or variable image scales, so the observer could select the scale most appropriate to the work.

Prior to the introduction of the small infrared arrays, mosaicking of point-resolved

digital images was a relatively uncommon technique in astronomy. Point-resolved images are those in which the point-spread function is not substantially contained in one pixel; most astronomical images are point-resolved. The mosaicking program in IRAF is in fact called “irmosaic,” even though it is not specific to infrared images (Tody 1986).

The central task in mosaic assembly is determining the registration, or overlap, of adjacent images. However, other image processing tasks are often intimately intertwined with registration, requiring an iterative approach. Astronomical examples of such intertwined steps include matching background levels, so that overlapping sky regions of adjacent images have the same flux, and adjusting the geometry of objects in the frame depending on their placement in the final mosaic. “Derotating” a planet that had turned significantly during the mosaic exposures is an example of the latter, as it involves a map transformation based on the size and location of the planet in the final image. It is important to select the proper order in which these tasks are done; it may even be necessary to iterate the entire procedure, and to ensure that the iteration converges reasonably.

Placing the pieces of a mosaic consists of two conceptual steps (which may be iterated): registering adjacent pieces and reconciling any disagreement that results. There are several ways to approach the first step, choosing the relative placement of two adjacent pieces in a mosaic:

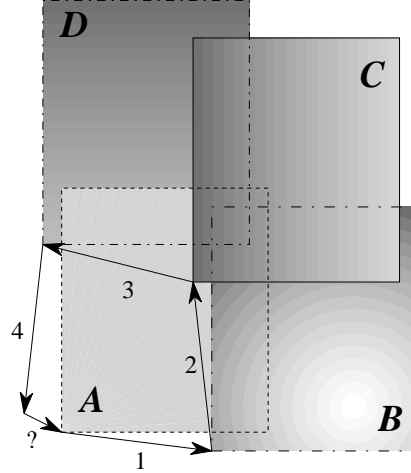


Fig. II.10. This 2×2 mosaic has four (non-corner) overlaps. Each overlap determines two numbers, the relative displacement of one piece with respect to the other both horizontally and vertically (vectors, labeled 1–4). However, the placement of three pieces with respect to the fourth completely determines the layout of the mosaic, and requires only six quantities. The four vectors, determined by image content that can change slightly between images, may not sum to zero, leaving a small residual (labeled with a question mark). The eight pieces of relative-position information must be reduced to six pieces of absolute-position information.

1. Use knowledge of camera pointing, regardless of the image content of the pieces.
2. Use control points, or unresolved image features that appear in the overlap regions of a pair of neighboring images, to register the images to one another.

One can achieve sub-pixel registration with multiple control points.

3. Use a fitting algorithm to generate a control point from resolved images. Frequently, the algorithm is estimating the center of fairly round features by eye. Model fitting to stars is common in astronomy.

4. Use a correlation algorithm that evaluates the overlapping portion of the two images for different candidate registrations, and chooses the best candidate.

For one-dimensional mosaics (strips of images), there can be no disagreement in piece placement because the problem is not overconstrained. Mosaics in two (or more) dimensions potentially have more overlap information than needed to place all the pieces. The concept of placement disagreement is best shown by an example, such as that in Fig. II.10. For two-dimensional mosaics with $m \times n$ pieces, there are $2(2nm - m - n)$ position values provided by the overlaps of adjacent pieces, but only $2(mn - 1)$ values to determine, since one piece defines the coordinate system without moving. There are many ways to reconcile differences in placement information. These include:

1. Discard enough information to make the problem go away.
2. Spread the disagreement in piece placement arithmetically to several adjacent pieces.
3. Use an algorithm that (perhaps iteratively) finds the best fit of all the pieces, effectively compromising based on the information in the image.

The mosaics from this project were difficult to assemble. Telescope pointing was not accurate to within the point-spread function, in part because of beam switches of up to $240''$ to take sky images. As a result, registration was necessarily by image content. Almost no stars appear in the overlaps of the Jupiter mosaics, eliminating the traditional astronomical control points. Since the planet rotated up to 18° during

one mosaic, the point-spread function was often not steady, and atmospheric features are rarely point-like near Jupiter's equator, features on the planet often changed between one image and the next. This eliminated fitting models to image features to derive control points, leaving only correlation techniques. The rotation and variable point-spread function also caused significant disagreement in the 2-dimensional overlap information. The 5,964 image overlaps in the combined aurora and atmospheric dynamics datasets made by-eye registration impractical, but simply discarding some positional information made unacceptably poor mosaics. These combined problems motivated the development of an automatic mosaic assembly algorithm and a program that implements it. The program is called 'jiggle'.

The jiggle procedure consists of several independent parts. They are implemented as separate, self-contained source modules so that any part can be modified or replaced without requiring code changes in the other modules. The jiggle program itself is a standalone C program that reads IRAF images from disk files. It can be called from IRAF or directly from the command line, and the image reading and writing functions are especially simple to allow the integration of other image formats.

The steps in the algorithm are:

1. Define a correlation function. This function produces a single value representing the quality of a candidate registration of one image with another. It is

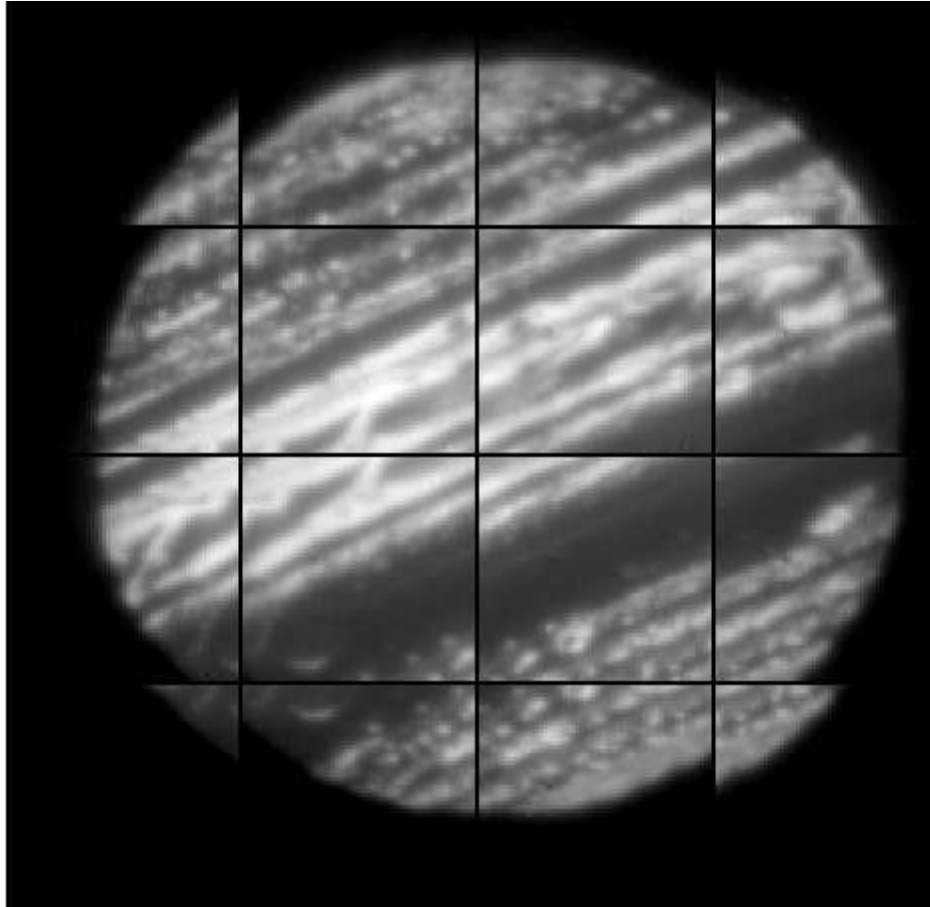


Fig. II.11. Pieces of a 4×4 -image mosaic of Jupiter at $4.9 \mu\text{m}$, taken between 9:05 and 9:17 UT on 22 March 1992. Image preprocessing removed detector nonlinearity, detector bias, “hot” and “cold” pixels, pixel sensitivity variations (flat field), and thermal emission from the sky, and trimmed a border of bad pixels. The images are 58×55 pixels each.

unimportant whether low or high values are good, but the mosaic evaluation function in step 3 below must know the convention. The scale of the values is unimportant, as is the rate at which they change with changing quality, though these items may affect computational performance.

2. Generate correlation images from all adjacent-piece overlaps using the correlation function. Each pixel in a correlation image corresponds to one possible registration of two images. The pixel's value is the value of the correlation function for that registration.
3. Define a mosaic evaluation function. This function, given a set of mosaic piece locations in the final image, uses the correlation images to generate a single value that represents the quality of the mosaic. To do this, the evaluation function must have knowledge of the shape and size of the pieces so that it can select the right pixel in each correlation function. By convention, low values are good.
4. Use a function minimizer to find the minimal value of the mosaic evaluation function and hence the optimal locations of all the pieces in the mosaic.

Correlation images are familiar from Fourier analysis (Bracewell 1986). They are a graphical representation of the quality of different registrations of two images. Figure II.12 shows how pixels in correlation images map to different image registrations. Figure II.13 shows the four correlations used in the jiggle program.

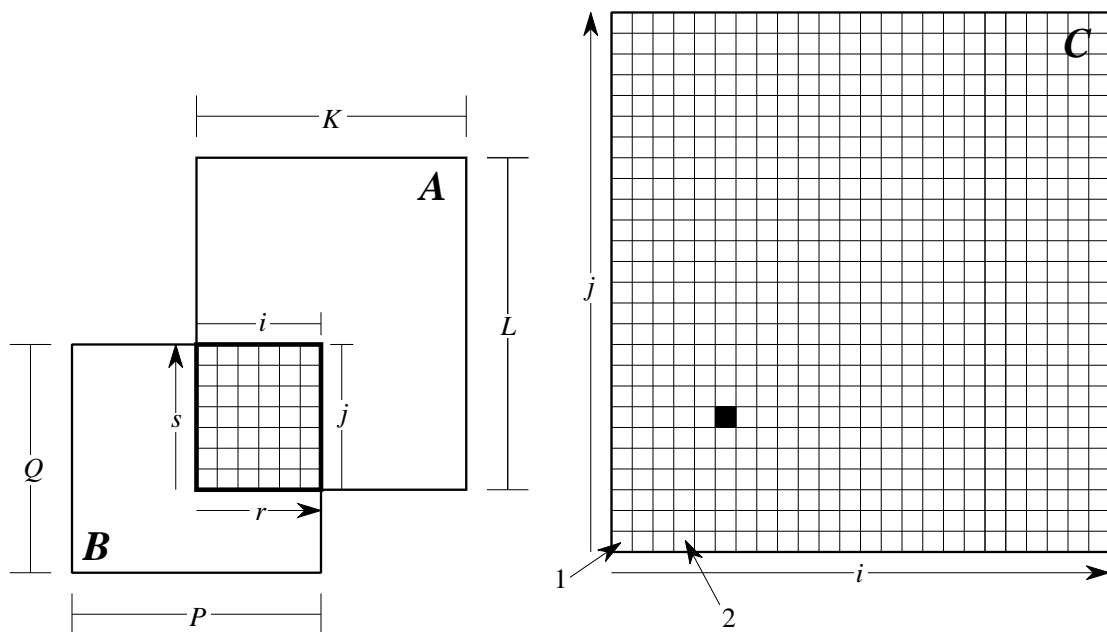


Fig. II.12. Each location in the correlation image, **C**, represents a unique registration, or overlap, of images **A** and **B**. The correlation image has indices i and j . The value of pixel C_{ij} is that of the correlation function applied to the overlapping parts of **A** and **B**. For notational simplicity, image sections **a** and **b** (not labeled), with indices r and s , refer to the indicated portions of images **A** and **B**, respectively. The dark pixel in image **C** represents the overlap of **A** and **B** shown here. The pixel labeled 1 represents a registration such that the lowest, leftmost pixel of **A** and the highest, rightmost pixel of **B** overlap each other. Pixel 2 is the overlap of the first 4 pixels in the bottom row of **A** and the last 4 pixels in the top of **B**. The center of the correlation image represents the two images perfectly centered on one another, and so on.

Consider images \mathbf{A} and \mathbf{B} , with dimensions $K \times L$ and $P \times Q$ pixels respectively. They are registered such that their respective rows and columns are parallel, and such that pixels \mathbf{B}_{PQ} and \mathbf{A}_{ij} coincide. The width and height of the overlap region are

$$w = \min(i, K) - \max(0, i - P) \quad (\text{II.6})$$

$$h = \min(j, L) - \max(0, j - Q). \quad (\text{II.7})$$

The image sections \mathbf{a} and \mathbf{b} define a secondary coordinate system whose origin in each image is the lower, left corner of the overlap region in that image:

$$\mathbf{a}_{rs} = \mathbf{A}_{\max(0, i-P)+r, \max(0, j-Q)+s} \quad (\text{II.8})$$

$$\mathbf{b}_{rs} = \mathbf{B}_{\max(0, P-i)+r, \max(0, Q-j)+s}. \quad (\text{II.9})$$

The four correlation functions in the jiggle program then use the indices r and s to access corresponding pixels in images \mathbf{A} and \mathbf{B} :

1. squared noise-to-signal ratio:

$$C_{ij} = \frac{1}{wh} \sum_{s=1}^h \sum_{r=1}^w \left(\frac{\mathbf{b}_{rs} - \mathbf{a}_{rs}}{\frac{\mathbf{b}_{rs} + \mathbf{a}_{rs}}{2}} \right)^2 \quad (\text{II.10})$$

2. squared noise:

$$C_{ij} = \frac{1}{wh} \sum_{s=1}^h \sum_{r=1}^w (\mathbf{b}_{rs} - \mathbf{a}_{rs})^2 \quad (\text{II.11})$$

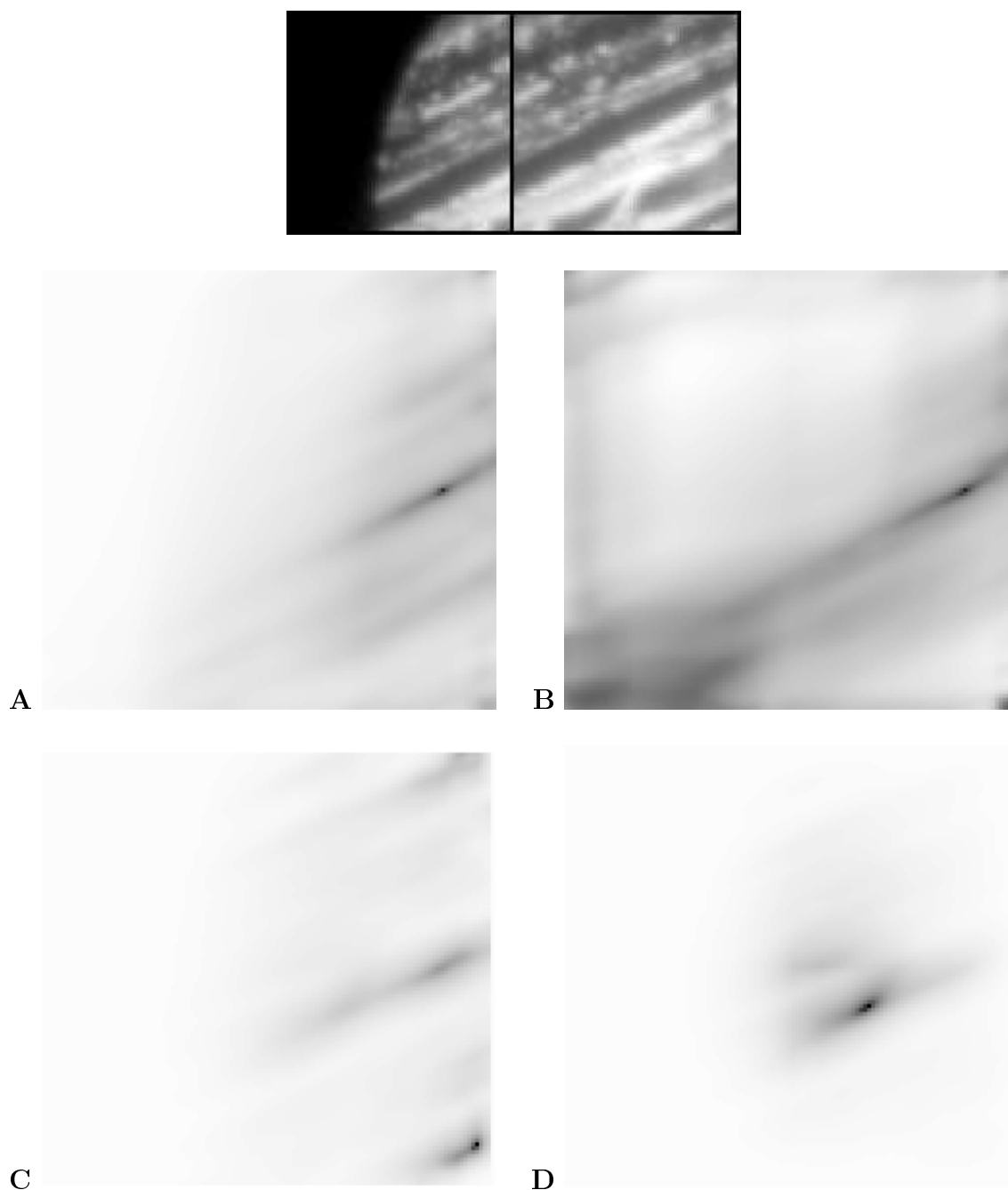


Fig. II.13. These are correlation images for the overlap of two mosaic pieces (top) from Fig. II.11. As described in Fig. II.12, each pixel corresponds to a possible registration of the two images, and low pixel values (dark) represents a good registration. The different correlation functions are: **A** squared ratio of noise to signal, **B** squared noise, **C** negative of mean product, and **D** negative of total product. All images have at the same logarithmic stretch. See the text for more detail about each correlation.

3. inverse mean product:

$$\mathbf{C}_{ij} = -\frac{1}{wh} \sum_{s=1}^h \sum_{r=1}^w \mathbf{b}_{rs} \mathbf{a}_{rs} \quad (\text{II.12})$$

4. inverse total product:

$$\mathbf{C}_{ij} = -\sum_{s=1}^h \sum_{r=1}^w \mathbf{b}_{rs} \mathbf{a}_{rs} \quad (\text{II.13})$$

In the product correlations, strong positive and strong negative features both multiply to the squares of their values when correctly aligned. As used in the jiggle program, both are negatives of the correlation described below, to conform to the convention that low values are good. The inverse total product is similar to the Fourier cross correlation, with several improvements.

The cross correlation (Bracewell 1986) is an application of the 2-dimensional Fourier transform, and as such the boundaries of the images are periodic: the images behave as though they were toroidal, wrapping both left-right and top-bottom. The periodic boundary condition causes problems unless images are first surrounded with wide borders of zero-valued pixels and the correlation image is renormalized so that each pixel represents the average, not the sum, of the products of image pixel values. Further, the input image pixel values must be arithmetically adjusted so that the mean value is zero to prevent a bias toward centrally-aligned images (note the strong central bias in image II.13D).

The jiggle program does not implement the cross correlation, but instead offers prod-

uct correlations without the periodic boundary condition. The main advantage to the Fourier cross correlation is the high calculation speed, but in mosaicking one generally knows something about where the pieces should go, and can place some limits on how far they may shift. One can use this knowledge to reduce the amount of calculation significantly, but only by using a brute-force method of calculation rather than a transform. The inverse total product correlation is a non-periodic cross correlation, and the inverse mean product correlation is renormalized so that the image doesn't discriminate against registrations containing fewer pixels.

The next step is to define a mosaic evaluation function. The parameters of such a function are the positions of all the pieces in the mosaic except one; for a two-dimensional image mosaic with $m \times n$ pieces, there are $2(mn - 1)$ parameters. Scaling, rotation and other geometric adjustments that might apply as free parameters (for example, in mosaics of spacecraft images) could potentially increase this number (and could also increase the number of dimensions in the correlation images). The jiggle program offers a single evaluation function that returns the sum of the appropriate pixel values, one from each correlation image. Different evaluation functions might choose to emphasize certain overlaps more than others. For example, the pieces of the 4×4 mosaics of Jupiter contain only a small amount of planet in each corner image (see Fig. II.11). Values from the corresponding overlaps could be given less weight. Since the locations requested by the minimizer in the final step may not be integers, the evaluation function must employ an interpolator. The jiggle program uses a simple bilinear routine, but the code allows for the substitution of any interpolator.

The final step is to use a function minimizer to explore the $2(mn - 1)$ -dimensional space represented by the evaluation function. This is significantly more efficient than actually generating a value for each point in the evaluation space and finding the minimal value, even for very restricted movement of mosaic pieces. The jiggle program uses one of the simplest of all multidimensional minimizers, the downhill simplex method. This minimizer, described in Press *et al.* (1992) and elsewhere, is an inefficient, brute-force approach. However, it is easy to implement and test and is not easily fooled. The implementation of the simplex minimizer in jiggle is original and improves on that presented by Press *et al.* After the routine finds a minimum, the program re-initializes it with points a fraction of a pixel away from the location it found. This helps to ensure that it is not fooled by local minima. If it finds the same place twice, the program returns the corresponding optimal offsets. Other programs then perform fractional-pixel shifts and assemble the mosaic (see Fig. II.14).

The jiggle program incorporates several efficiency enhancements and several more could be made. First, it only computes enough of each correlation image to include sensible offsets from the nominal positions. Other offsets are assigned large values in the correlation images so that the minimizer avoids them. Restricting the calculation reduced the time to generate correlation images by over a factor of 100 for the 1992 Jupiter mosaics. Second, the correlation functions are evaluated in a quadruply-nested loop. The mathematical functions are performed in line (without an explicit function call) since they are simple and function call overhead would otherwise dominate the run time. Other enhancement ideas include recording the results of each

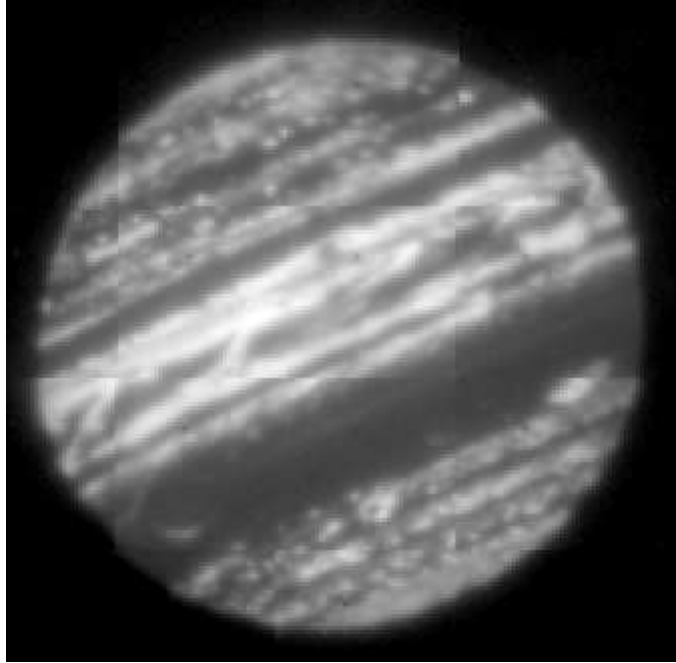


Fig. II.14. The final mosaic.

mosaic evaluation computation and re-using the values if the minimizer refers to the same point twice. Finally, ignoring pixels whose values are outside set limits would allow the separation of background and object pixels. This would ensure that the correlation reflected only matching object features and not, for example, matching detector bias patterns.

Appendix C

AUTOMATICALLY CENTERING THERMAL JUPITER IMAGES

Jupiter in the near thermal infrared ($\sim 5\text{ }\mu\text{m}$) looks very different from its appearance in visible light (see Fig. II.15). As mentioned in the main text, this wavelength is sensitive to thermal emission from deep in the troposphere and absorption by overlying clouds. The extinction is so strong that almost no light originating in or below the clouds appears on the detector, and almost no light is emitted or reflected above the clouds at these wavelengths. As a result, the final image is one of bright clear zones and dark cloud belts, with some of the cloud belts almost as dark as the nearby sky, particularly near the limb of the planet. Identifying the limb within the resolution limits imposed by image quality and pixel size can be challenging for a human analyst and computational limb-identification methods developed for visible-light images often fail on such images. Since mapping Jupiter images in longitude

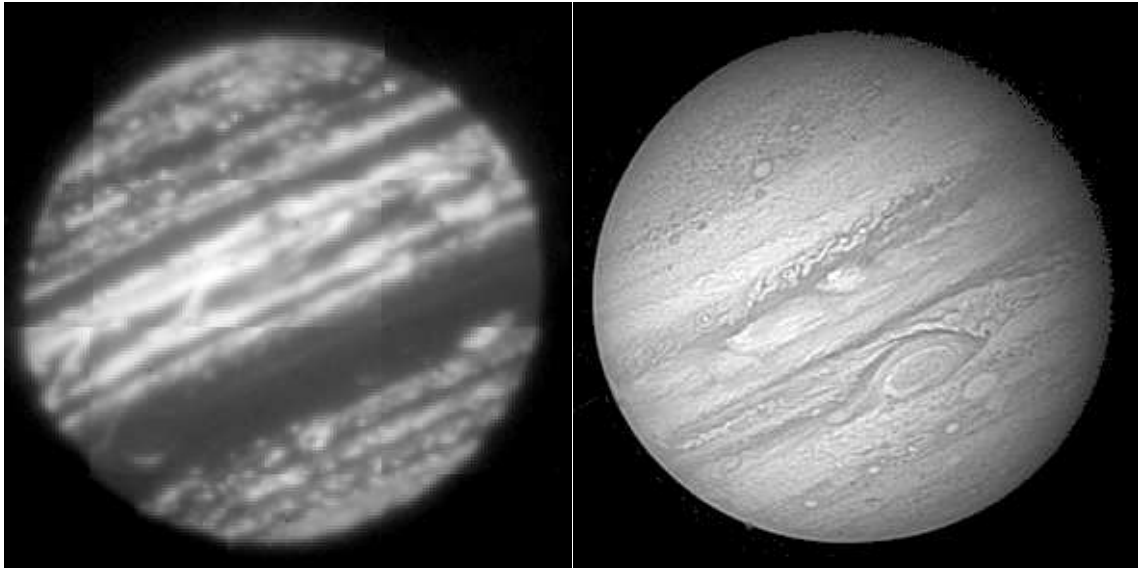


Fig. II.15. To a computer, this 4.9- μm image of Jupiter (left) is very different from a Voyager image in visible light (right). In the infrared image, which is shown with a logarithmic stretch, the background is $\sim 10,000$ analog-to-digital conversion units (ADU) near the planetary limb. The dark band in the southern hemisphere is $\sim 22,000$ ADU. The strongest features are over 1,800,000 ADU. Since both weak and strong features exist on the limb, and seeing widens all features, simply setting a cut-off level and fitting an ellipse to part of the sunlit limb would find the center of the optical image, but not the infrared one. On nights with poorer seeing, the problem is considerably worse.

and latitude is necessary for analysis, identifying the limb accurately is important.

A new limb identification method achieves high accuracy, however. After centering with the new method, a video sequence of the images does not show the rapid shifts that images aligned with other methods show. The method is conceptually simple:

1. Create a slightly “fuzzed” image by convolving the original image with a Gaussian filter that is about one pixel wide.
2. Subtract this image from the original, and set pixels with values outside rea-

sonable limits for the limb to zero. The result is similar to a truncated gradient image: both the background and the hottest areas have values at or near zero, and areas where the signal rises steeply have high values. The limb stands out as a narrow feature on much of the planet. The remaining features are fairly randomly distributed.

3. Fuzz the image a second time with a 2-pixel-wide Gaussian filter. This both eliminates noise and makes the limb wider and hence easier to locate. Fig. II.16 shows the intermediate and final images.
4. Define a function that returns minus the mean of pixel values on rotated ellipses in images. Since the limb consists of positive (rising signal) pixels, this function is a low-is-good quality indicator for candidate sets of high-valued pixels arrayed in an ellipse.
5. Starting with the approximate parameters for Jupiter's limb, use a function minimizer to explore the space of ellipse quality in the image. For Jupiter, good constraints include not allowing the eccentricity and orientation to vary, and not allowing the semimajor axis to vary by more than a few percent. This avoids locating the Great Red Spot (GRS) instead of the limb.

The “limbctr” program implements this procedure, using the bilinear image interpolator and function minimizer of the previous chapter, and a new quality function that fits rotated ellipses to image data.

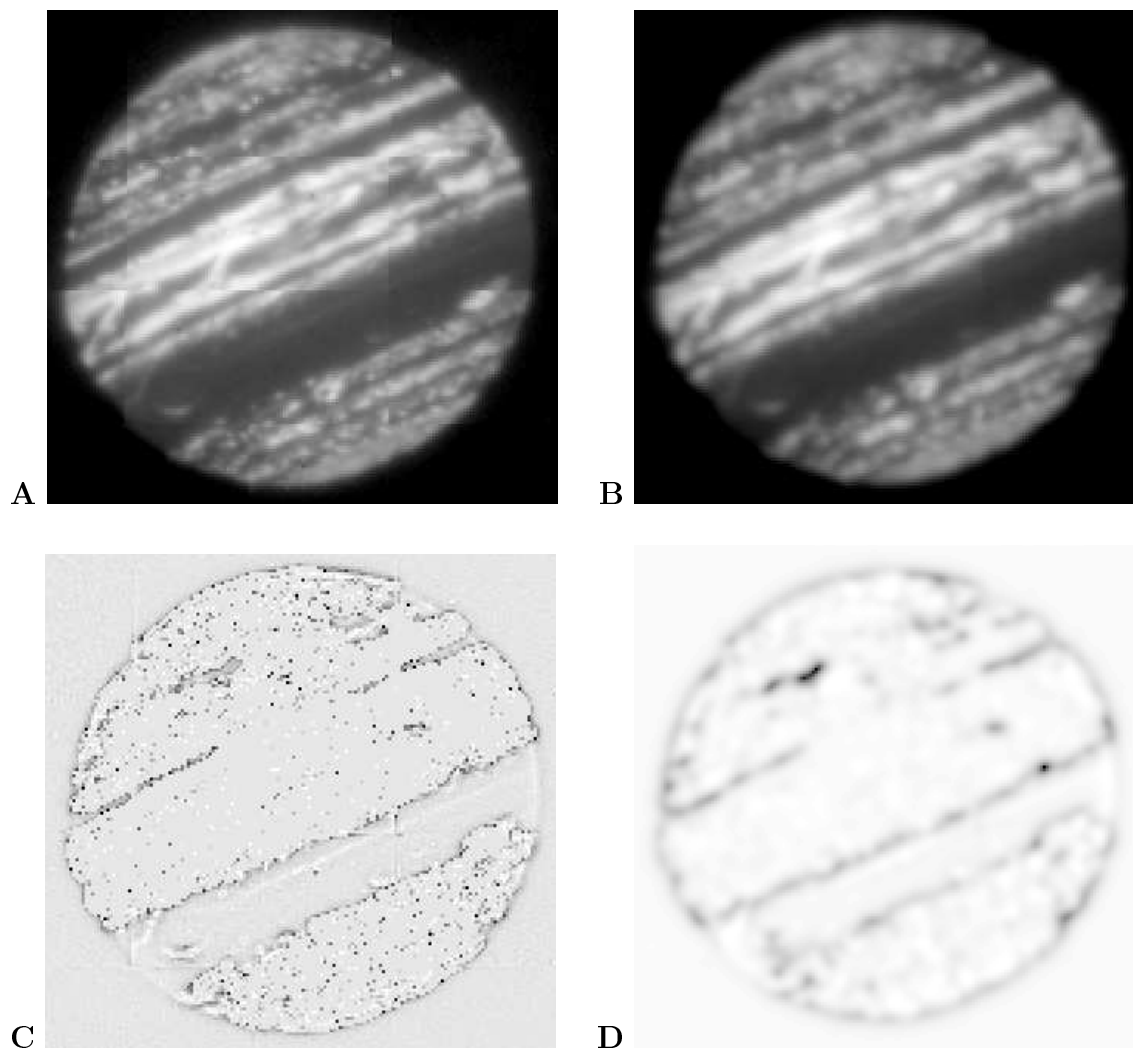


Fig. II.16. **A** The original 5- μm Jupiter image. **B** The image after convolution with a 1-pixel-wide Gaussian filter. **C** The difference between **A** and **B**, with extreme-valued pixels set to zero. **D** The final image after convolution with a 2-pixel-wide Gaussian filter. The limb now stands out as a smooth, coherent feature, wide enough to not to be missed by the ellipse fit.

Appendix D

FLUID DERIVATIONS FOR OBSERVERS

The following “intuitive” approach to some planetary-scale atmospheric phenomena will assist observers whose backgrounds do not include fluid dynamics. Rossby waves arise from the conservation of potential vorticity, q , in the absence of viscosity. This conservation law, worked out definitively by Ertel (1942), combines conservation of mass and angular momentum and has become a central tool in fluid dynamics. Consider a rotating, incompressible fluid cylinder (see Fig. II.17) with height h , radius r , and density ρ . It rotates rigidly around its axis with angular speed ω . For this cylinder,

$$m = \pi r^2 h \rho, \tag{II.14}$$

and

$$Q = \frac{1}{2} m r^2 \omega, \tag{II.15}$$

where m is mass, Q is the magnitude of angular momentum, and both are conserved.

Eliminating r gives

$$\frac{\omega}{h} = \frac{2\pi\rho Q}{m}. \quad (\text{II.16})$$

Everything on the right side is conserved, so the left side is also conserved. Fluid dynamicists use vorticity, ζ , to measure rotation. For a shallow fluid,

$$\zeta = (\nabla \times \mathbf{v}) \cdot \hat{\mathbf{k}}, \quad (\text{II.17})$$

where \mathbf{v} is the fluid velocity field and $\hat{\mathbf{k}}$ the surface-normal unit vector. For our cylinder, with axis parallel to $\hat{\mathbf{k}}$,

$$\zeta = -\frac{\partial u}{\partial y} + \frac{\partial v}{\partial x}, \quad (\text{II.18})$$

where x and y are Cartesian coordinates in the plane of the end of the cylinder and u and v are fluid velocities in those directions, respectively. The rigid-body rotation ω is equal to each of the two terms on the right side, yielding

$$\zeta = 2\omega. \quad (\text{II.19})$$

Thus,

$$q = \frac{\zeta}{h} = \frac{4\pi\rho Q}{m} \quad (\text{II.20})$$

for our cylinder of inviscid, incompressible fluid. We move this coordinate system onto a planetary surface by adding a planetary rotation term. In this case our ζ is

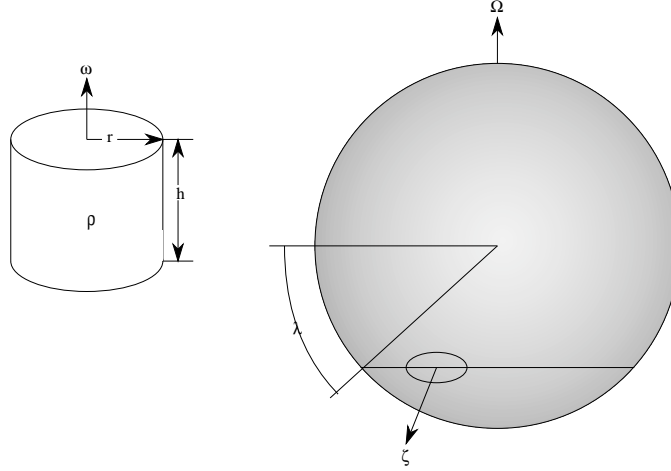


Fig. II.17. Fluid cylinder and planetary coordinate system used in potential vorticity example; see text.

called the relative vorticity and is added to the planetary vorticity, f , to form the absolute vorticity. The planetary vorticity is

$$f = 2\mathbf{\Omega} \cdot \hat{\mathbf{k}} = 2\Omega \sin(\lambda), \quad (\text{II.21})$$

where Ω and $\mathbf{\Omega}$ are the planetary angular speed and velocity, respectively, and λ is planetographic latitude. Planetary vorticity is a monotonically increasing function from the south to the north pole (assuming prograde rotation). The potential vorticity for a shallow planetary atmosphere is then

$$q = \frac{\zeta + f}{h}, \quad (\text{II.22})$$

where h is now the effective thickness of the atmosphere.

Rossby waves arise from conservation of q in each fluid element (Holton 1992, especially Fig. 17.4). To see this, consider a steady zonal (purely east-west) flow in a planetary atmosphere, and hold the thickness of the flow constant. Shear in such a flow creates vorticity; no vortices are needed for vorticity to exist. If a portion of the flow were diverted northward, f would increase. Since h and q are constant, ζ must decrease. This implies a new clockwise flow around the diverted fluid, pulling northward on the fluid to its west and southward on the fluid to its east. As they move, these two nearby regions experience changes in *their* f and ζ , and act on the regions adjacent to them. At the original latitude, the action is stronger on the fluid to the west because as it moves north it approaches the disturbed region and receives a stronger pull, whereas the eastern region moves away and receives progressively less. Rossby wave propagation in this simple example is therefore opposite the direction of planetary rotation (in general it is in the direction opposite the cross-stream potential vorticity gradient). The result of the continued wave action is that the original, steady, zonal flow now oscillates about its original latitude, tracing a sinusoidal path around the planet.

Any steady deflector can drive Rossby waves. One example is a vortex in the middle of a zonal flow. Such a vortex would divert flow around it and the flow would then oscillate after passing the vortex. The polar hexagon on Saturn is an example of such a flow (Godfrey 1988). Another driver would come into play if the lower atmospheric interface, instead of being smooth, had instead large meridional (north-south) ridges over which the zonal flow had to pass. As the flow went over a ridge, h would

decrease. There must now be a corresponding decrease in $(\zeta + f)$. Momentum would initially tend to keep the flow at the same latitude, inducing ζ to decrease. This again superposes a clockwise flow centered on the ridge, pushing material west of the ridge to the north and east of the ridge to the south, driving a wave. The “banana-cell” convection of Hart *et al.* (1986b) posits such effective ridges on the giant planets as a result of interior convection.

The generality of fluid dynamics literature and the many different formulations that are convenient for different situations make it difficult to find a simple, self-contained Rossby-wave dispersion relation derivation tuned to zonal flows on the giant planets. Ingersoll and Cuong (1981) give a good beginning, setting up the basic equations with the same approximations and assumptions used here.

We will first linearize the planetary vorticity equation and develop basic fluid equations under the quasi-geostrophic (QG) approximation, choosing a purely zonal basic state and a single shallow weather layer over a relatively unchanging deeper layer. We will then introduce small perturbations and nondimensionalize the equation for conservation of potential vorticity to discard terms with minimal effect. Next, we develop an expression for this in the rotating planetary coordinate system, and plug in the values from the linearized basic state. Finally, we look for wave-like solutions to derive the resultant dispersion relation. This is a larger number of approximations than a modeler would make in a realistic model. However, the basic physics survive and the resulting dispersion relation contains the terms of interest to the present

work.

We begin with the β -plane approximation to linearize the planetary vorticity:

$$f \approx f_0 + \beta y \quad (\text{II.23})$$

$$\beta = \left. \frac{\partial f}{\partial y} \right|_{y=y_0}, \quad (\text{II.24})$$

where symbols subscripted by 0 refer to their values at the linearization point of f .

The momentum equations from the QG approximation say that the two main driving forces for large-scale planetary winds are the pressure gradient between regions of differing pressure and the Coriolis effect (which builds a pressure gradient perpendicular to a moving wind), and that they tend to balance each other. Quasi-geostrophic balance gives rise to circulating currents around high and low pressure regions (the existence of which motivated this formulation for terrestrial meteorology). The approximation further states that the fluctuations in the thickness of the weather layer are small compared to the thickness. Continuing with the notation from above, the basic QG layer thickness and horizontal momentum equations are

$$h = H + \eta \quad (\text{II.25})$$

$$-f_0 v \approx -\frac{\partial}{\partial x} g(H + \eta + h_2) \quad (\text{II.26})$$

$$f_0 u \approx -\frac{\partial}{\partial y} g(H + \eta + h_2), \quad (\text{II.27})$$

where h is the layer thickness, the constant H is the mean thickness of the weather layer, $\eta(x, y, t)$ represents the (small) fluctuations in the weather layer thickness, g is the gravitational acceleration, and h_2 is the deep layer thickness, which we take not to evolve in time. Throughout this derivation, the subscript 2 indicates a quantity in the unchanging deep layer. The vertical momentum equation reduces to hydrostatic balance because we have assumed a shallow weather layer with small vertical winds.

The QG approximation lets us express u , v , and ζ as functions of a simple, analytically-tractable streamfunction, ψ , and the horizontal gradient operator ∇ :

$$u = -\frac{\partial\psi}{\partial y}, \quad v = \frac{\partial\psi}{\partial x} \quad (\text{II.28})$$

$$u_2 = -\frac{\partial\psi_2}{\partial y}, \quad v_2 = \frac{\partial\psi_2}{\partial x} \quad (\text{II.29})$$

$$\zeta = \nabla^2\psi \quad (\text{II.30})$$

$$\psi = \frac{g}{f_0}(\eta + h_2), \quad \psi_2 = \frac{g}{f_0}h_2 \quad (\text{II.31})$$

$$q = \frac{\nabla^2\psi + f_0 + \beta y}{H + \eta}. \quad (\text{II.32})$$

Next we substitute scale factors and non-dimensional variables into Eq. II.32, linearize it, and keep only first-order terms. The linearization occurs in the denominator:

$$\frac{1}{H + \eta} = \frac{1}{H(1 + \frac{\eta}{H})} \quad (\text{II.33})$$

$$\approx \frac{1}{H} \left(1 - \frac{\eta}{H}\right). \quad (\text{II.34})$$

The variables and their nondimensional substitutions (indicated by dots) are:

$$x \rightarrow L\dot{x}, \quad y \rightarrow L\dot{y}, \quad \nabla^2 \rightarrow \frac{1}{L^2} \dot{\nabla}^2 \quad (\text{II.35})$$

$$u \rightarrow U\dot{u}, \quad v \rightarrow U\dot{v} \quad (\text{II.36})$$

$$\psi \rightarrow UL\dot{\psi}, \quad \eta \rightarrow \frac{f_0 UL}{g} \dot{\eta} \quad (\text{II.37})$$

$$f \rightarrow f_0 \dot{f}, \quad \beta \rightarrow \frac{U}{L^2} \dot{\beta}. \quad (\text{II.38})$$

Equation II.32 then becomes

$$q = \frac{1}{H} \left(\frac{1}{L^2} \dot{\nabla}^2 UL\dot{\psi} + f_0 + \frac{U}{L^2} \dot{\beta} Ly \right) \left(1 - \frac{f_0 UL}{g} \frac{\dot{\eta}}{H} \right) \quad (\text{II.39})$$

$$q \frac{H}{f_0} = \left(1 + \epsilon \dot{\nabla}^2 \dot{\psi} + \epsilon \dot{\beta} y \right) \left(1 - \epsilon \frac{f_0^2 L^2}{gH} \dot{\eta} \right) \quad (\text{II.40})$$

$$\frac{q_{QG}}{f_0} = q \frac{H}{f_0} = \left(1 + \epsilon \dot{\nabla}^2 \dot{\psi} + \epsilon \dot{\beta} y \right) \left(1 - \epsilon \frac{L^2}{L_d^2} \dot{\eta} \right) \quad (\text{II.41})$$

$$= 1 + \epsilon \dot{\nabla}^2 \dot{\psi} + \epsilon \dot{\beta} y - \epsilon \frac{L^2}{L_d^2} \dot{\eta} + O(\epsilon^2). \quad (\text{II.42})$$

Here we have introduced the Rossby number,

$$\epsilon = \frac{U}{f_0 L} \ll 1. \quad (\text{II.43})$$

Typical scale values for Jupiter are $U = 50$ m/sec, $f_0 = 10^{-4}$ /sec, and $L = 3 \times 10^6$ m,

and for these values $\epsilon = 0.17$. We have also used

$$L_d = \frac{\sqrt{gH}}{f_0}, \quad (\text{II.44})$$

where L_d is the deformation radius. This is a typical length scale for Coriolis-driven interactions on Jupiter. We can now drop terms of second or higher order in Rossby number:

$$q \frac{H}{f_0} \approx 1 + \epsilon \dot{\nabla}^2 \psi + \epsilon \beta y - \epsilon \frac{L^2}{L_d^2} \dot{\eta}. \quad (\text{II.45})$$

Next, we return to the dimensional variables and cancel as many as we can:

$$q \frac{H}{f_0} \approx 1 + \epsilon L^2 \nabla^2 \frac{1}{UL} \psi + \epsilon \frac{L^2}{U} \beta \frac{1}{L} y - \epsilon \frac{L^2}{L_d^2} \frac{g}{f_0 UL} \eta \quad (\text{II.46})$$

$$qH \approx f_0 + \nabla^2 \psi + \beta y - \frac{1}{L_d^2} \frac{g}{f_0} \eta. \quad (\text{II.47})$$

Then we write η in terms of the ψ 's, and expand the Laplacian:

$$qH \approx f_0 + \nabla^2 \psi + \beta y - \frac{1}{L_d^2} (\psi - \psi_2) \quad (\text{II.48})$$

$$qH \approx \frac{\partial^2 \psi}{\partial x^2} + \frac{\partial^2 \psi}{\partial y^2} + f_0 + \beta y - \frac{1}{L_d^2} (\psi - \psi_2). \quad (\text{II.49})$$

Next we use the chain rule for differentiation to calculate what potential vorticity conservation in a fluid element following the path $(x(t), y(t), t)$ looks like in a stationary

reference frame:

$$\frac{d q(x(t), y(t), t)}{dt} = 0 \quad (\text{II.50})$$

$$\frac{\partial q}{\partial t} + \frac{\partial q}{\partial x} \frac{dx}{dt} + \frac{\partial q}{\partial y} \frac{dy}{dt} = 0 \quad (\text{II.51})$$

$$\frac{\partial q}{\partial t} + \mathbf{v} \cdot \nabla q = 0. \quad (\text{II.52})$$

Note that this is the material derivative,

$$\frac{D}{Dt} = \frac{\partial}{\partial t} + \mathbf{v} \cdot \nabla, \quad (\text{II.53})$$

a shorthand notation used frequently in fluid dynamics to connect fluid-element (Lagrangian) phenomena to a stationary (Eulerian) grid. Bold type indicates horizontal vector quantities.

Now take a zonal basic state and add small perturbations to the upper layer:

$$\psi(x, y, t) = \bar{\psi}(y) + \psi'(x, y, t) \quad (\text{II.54})$$

$$\psi_2(x, y, t) = \bar{\psi}_2(y) + 0. \quad (\text{II.55})$$

Since the primes and overbars correspond to the variables with respect to which the parameters vary, the derivation is clearer without the functional notation. The

linearity of the system gives other quantities a similar form:

$$u = \bar{u} + u', \quad \bar{u} = -\frac{\partial \bar{\psi}}{\partial y}, \quad u' = -\frac{\partial \psi'}{\partial y} \quad (\text{II.56})$$

$$v = \bar{v} + v', \quad \bar{v} = 0, \quad v' = \frac{\partial \psi'}{\partial x} \quad (\text{II.57})$$

$$\begin{aligned} q &= \bar{q} + q', \\ \bar{q} &= \frac{1}{H} \left(f_0 + \beta y - \frac{1}{L_d^2} [\bar{\psi}_2 - \bar{\psi}] + \frac{\partial^2 \bar{\psi}}{\partial y^2} \right), \\ q' &= \frac{1}{H} \left(-\frac{\psi'}{L_d^2} + \frac{\partial^2 \psi'}{\partial x^2} + \frac{\partial^2 \psi'}{\partial y^2} \right). \end{aligned} \quad (\text{II.58})$$

The basic-state quantities are functions of y only. Practically these are zonal averages and this is indicated by an overbar; for example, $\bar{u}(y)$ is the zonally-averaged wind.

Eq. II.52 now becomes

$$\frac{\partial q'}{\partial t} + (\bar{u} + u') \frac{\partial q'}{\partial x} + v' \left(\frac{\partial \bar{q}}{\partial y} + \frac{\partial q'}{\partial y} \right) = 0. \quad (\text{II.59})$$

Dropping the (small) products of perturbation quantities, this becomes the linear equation

$$\frac{\partial q'}{\partial t} + \bar{u} \frac{\partial q'}{\partial x} + v' \frac{\partial \bar{q}}{\partial y} = 0. \quad (\text{II.60})$$

Substituting only for the perturbation quantities,

$$\begin{aligned} & \left(-\frac{1}{L_d^2} \frac{\partial \psi'}{\partial t} + \frac{\partial^3 \psi'}{\partial t \partial x^2} + \frac{\partial^3 \psi'}{\partial t \partial y^2} \right) + \\ & \bar{u} \left(-\frac{1}{L_d^2} \frac{\partial \psi'}{\partial x} + \frac{\partial^3 \psi'}{\partial x^3} + \frac{\partial^3 \psi'}{\partial x \partial y^2} \right) + \\ & \quad \frac{\partial \psi'}{\partial x} \frac{\partial \bar{q}}{\partial y} = 0. \end{aligned} \quad (\text{II.61})$$

Finally, we try oscillating solutions for ψ' :

$$\psi' = e^{i(kx+ly-\omega t)}, \quad (\text{II.62})$$

where k and l are zonal and meridional wavenumbers and $c = \omega/k$ is the zonal phase speed (note that this is a different ω from the angular speed used at the beginning of this chapter). For this solution,

$$\frac{\partial \psi'}{\partial x} = ik\psi', \quad \frac{\partial \psi'}{\partial t} = -i\omega\psi', \quad \frac{\partial^3 \psi'}{\partial x^3} = -ik^3\psi' \quad (\text{II.63})$$

$$\frac{\partial^3 \psi'}{\partial x \partial y^2} = -ikl^2\psi', \quad \frac{\partial^3 \psi'}{\partial t \partial^2 x} = i\omega k^2\psi', \quad \frac{\partial^3 \psi'}{\partial t \partial^2 y} = i\omega l^2\psi'. \quad (\text{II.64})$$

The Rossby wave dispersion relation appears after one more substitution and a consolidation of terms:

$$\begin{aligned} & \frac{1}{L_d^2} i\omega\psi' + i\omega k^2\psi' + i\omega l^2\psi' + \\ & \bar{u} \left(-\frac{1}{L_d^2} ik\psi' - ik^3\psi' - ik l^2\psi' \right) + \\ & ik\psi' \frac{\partial \bar{q}}{\partial y} = 0 \end{aligned} \quad (\text{II.65})$$

$$\omega \left(\frac{1}{L_d^2} + k^2 + l^2 \right) - \bar{u} k \left(\frac{1}{L_d^2} + k^2 + l^2 \right) + k \frac{\partial \bar{q}}{\partial y} = 0 \quad (\text{II.66})$$

$$c = \frac{\omega}{k} = \bar{u} - \frac{\frac{\partial \bar{q}}{\partial y}}{\frac{1}{L_d^2} + k^2 + l^2}, \quad (\text{II.67})$$

where c is the Rossby wave phase speed we seek.

This equation becomes more useful for an observer if we replace the wavenumbers k and l by the non-dimensional planetary wavenumbers m and n , respectively, which count the wavelengths girdling the planet zonally and meridionally:

$$c = \bar{u} - \frac{L_d^2 \frac{\partial \bar{q}}{\partial y}}{1 + \frac{L_d^2}{R^2} \left(\frac{m^2}{\cos^2(\lambda)} + n^2 \right)}, \quad (\text{II.68})$$

where R is the planetary radius and λ is the latitude.

Equation II.68 shows that short waves (large m and n) move nearly at the local zonal wind speed, \bar{u} , and that longer waves move slower. The quantity $\frac{\partial \bar{q}}{\partial y}$ determines how longer waves behave. Dowling (1993) discusses how this quantity is distributed on Jupiter.

Part III

Predictions for the Impact of Comet

P/Shoemaker-Levy 9 on Jupiter

Chapter 1

Dynamic response of Jupiter's atmosphere to the
impact of comet Shoemaker-Levy 9

Dynamic response of Jupiter's atmosphere to the impact of comet Shoemaker-Levy 9

Joseph Harrington, Raymond P. LeBeau Jr,
Kari A. Backes, and Timothy E. Dowling

Massachusetts Institute of Technology, 77 Massachusetts Avenue,
Cambridge, Massachusetts 02139, USA

Submitted to *Nature* 12 December 1993.

Received 14 December 1993.

Revised 8 February 1994.

Accepted 3 March 1994.

Publication reference:

Harrington, J., LeBeau, R. P., Backes, K. A. & Dowling T. E.
Nature **368**, 525–527 (1994).

© 1994 Macmillan Magazines Limited. Reprinted by permission.

DURING the period 18–24 July 1994, over 20 fragments of comet Shoemaker-Levy 9 will collide with Jupiter^{1–3}. The thermal and condensation signatures of inertia-gravity waves emanating from the impact sites will, if detectable, provide valuable insight into the stratification of Jupiter’s atmosphere. We report here simulations of the event using a global multi-layer model⁴ of Jupiter’s atmosphere and a range of impact kinetic energies (10^{27} – 10^{30} erg) that allows for the uncertainties in the sizes and densities of the comet fragments^{5–8}. The resulting inertia-gravity waves give rise to temperature perturbations in the range 0.004–1.2 K. The signature of the larger impacts may be detectable by thermal infrared imaging, and even weak signals may be detectable if one allows for the fact that the waves propagate in coherent rings centred on each impact site. Our simulations also indicate that a small vortex should form in the atmosphere following each impact, but that these will be sheared apart by the zonal winds within a few weeks.

An atmosphere’s density stratification, the rate at which density decreases with altitude, strongly influences the type of weather it exhibits. On Jupiter, stratification is poorly constrained in the most active region of the atmosphere, the troposphere. The deformation radius, L_d , is one measure of stratification. For length scales smaller than L_d , gravity flattens pressure highs and lows; for length scales larger than L_d , the Coriolis force sustains these anomalies. On Jupiter, L_d ranges from $\sim 3,000$ km in the stratosphere⁹ to zero in the neutrally-stable convecting interior. Observational data

poorly constrain the transition between these extremes, yet the transition greatly affects tropospheric meteorology. For example, the effective L_d in two-layer atmosphere models^{10–13} is uncertain by a factor of five, and as L_d is usually squared in fluid equations, key dynamical terms are uncertain by a factor of 25.

One can determine L_d by measuring the speed of inertia-gravity waves. These waves are generated by the adjustment process that brings large-scale disturbances into geostrophic balance. The group velocity of the leading wavefront is $c \approx L_d f$, where $f = 2\Omega \sin(\lambda)$ is the Coriolis parameter, Ω is the planetary rotation rate, and λ is the planetographic latitude. The Shoemaker-Levy 9 impacts may provide the perturbations needed to set observable waves in motion, after which wave speeds will not depend on anything to do with the comet — a perfect experiment and one that is unlikely to recur soon¹⁴.

To investigate the dynamical response to comet impacts, we ran simulations with the Explicit Planetary Isentropic-Coordinate (EPIC) atmospheric model for Jupiter⁴, which is based on the finite-difference algorithm of Hsu and Arakawa¹⁵. To resolve Jupiter’s nonlinear dynamics, our horizontal resolution is 512×256 cells, equivalent to 0.7° or ~ 900 km at the equator. Five active layers simulate the atmosphere (see Fig. III.1), and a sixth layer with a steady wind profile models the interior. Specifying the initial wind in each layer is problematical¹⁶. The Voyager infrared observations and the thermal wind equation¹⁷ indicate that Jupiter’s winds decay with height above the cloud tops. How they vary below the clouds is unknown, although we expect the

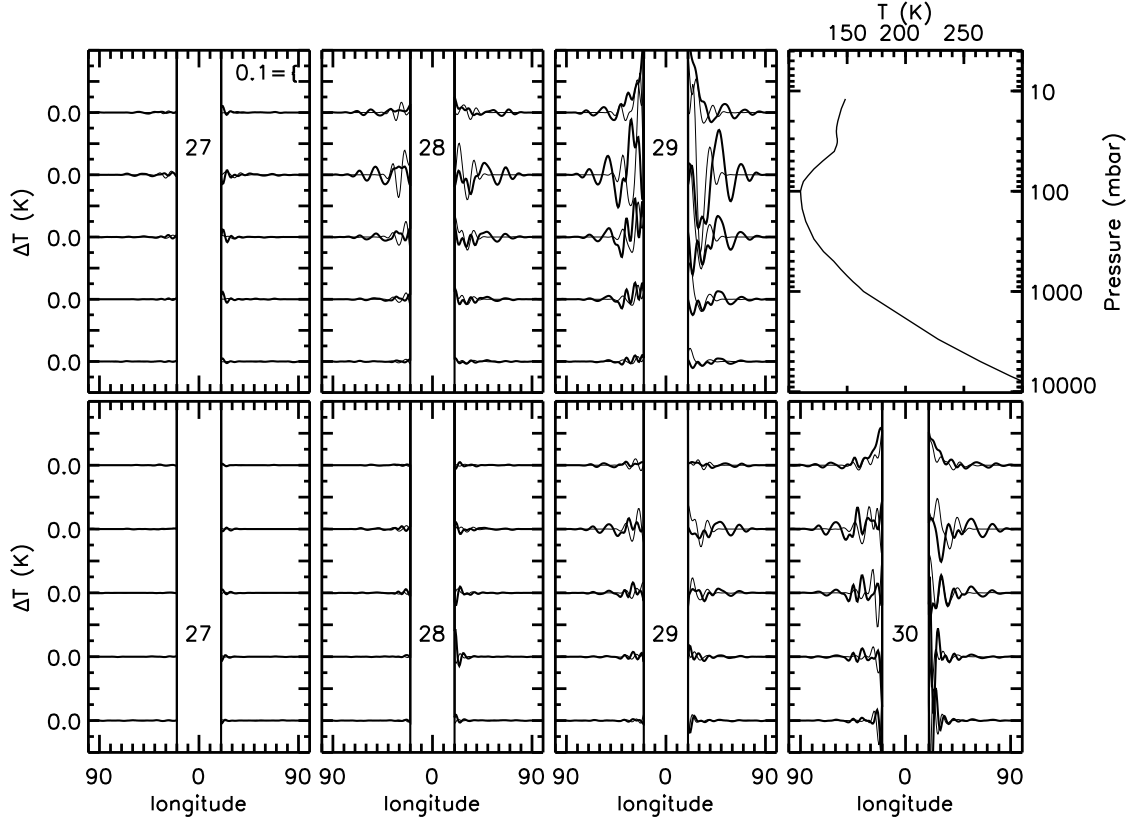


FIG. III.1 Upper right, The initial temperature versus pressure, $T(p)$, curve for the model atmosphere, showing the tropopause at ~ 100 mbar. We used the available Voyager data for pressures less than 700 mbar. For higher pressures we extrapolated as shown assuming a slightly stable atmosphere. Such guesswork will be unnecessary if inertia-gravity wave speeds are measured in the troposphere. Other plots, Temperature deviation profiles for comet-Jupiter impact simulations. The top row of three plots corresponds to energy deposition into the stratosphere, the lower row of four plots to tropospheric energy deposition. The five vertically-stacked profiles in each of the seven plots correspond to layer interfaces in the model. The top layer extends to zero pressure and the steady-wind interior begins at 5,000 mbar. The plots show temperature deviations from an unperturbed model one day (light line) and two days (heavy line) after the impact of a comet fragment. Minor ticks on the vertical axis are 0.1 K. Energy deposition altitudes are indicated by the placement of the log of the impact energy in ergs. To determine interface pressure levels (and hence layer spacings), extend the zero of the vertical scale to the pressure axis of the $T(p)$ plot. The region close to the impact point is masked for clarity. A low-pass filter removed grid-scale noise.

deep interior to rotate with the magnetic field. In the simulations presented here, we constructed the initial wind field in each active layer by multiplying the observed cloud-top zonal wind¹⁸ by a gaussian function in altitude centred at 500 mbar with a width parameter $\sigma = 2$ pressure scale heights. We set the interior profile to half the cloud-top winds. The choice of interior wind affects planetary-scale (Rossby) waves but does not significantly affect inertia-gravity waves, which are the focus of this work. We gradually force the initial winds for ~ 50 d to allow the mass and momentum fields to balance. The model then runs without forcing for ~ 150 d so shear instabilities can develop and equilibrate before the impact perturbation.

The EPIC model was designed for large-scale meteorological applications and hence incorporates the hydrostatic approximation, which equates the vertical pressure gradient with gravity and ignores vertical accelerations. This unfortunately eliminates sound waves that, in the Shoemaker-Levy 9 event, may provide seismic information about Jupiter’s deep interior¹⁹. EPIC employs a wave-damping ‘sponge’, gradually introduced in the upper 20% of the layers to prevent reflections from the top of the model²⁰. For the runs reported here only the top layer contains the sponge, but it is nevertheless effective; future work will use more layers. A low-pass filter at the poles prevents numerical instabilities resulting from the small grid spacing.

The impact velocity is well-established³ at $\sim 60 \text{ km s}^{-1}$. On the other hand, disparate estimates of the maximum fragment size (1 – 4 km, refs 5 and 6) and varying density

assumptions ($0.2 - 1.0 \text{ g cm}^{-3}$, refs 7 and 8) combine to make the impact kinetic energy uncertain by a factor of ~ 400 . Further, no reliable constraint has been placed on the energy fraction that remains in the atmosphere after the nonhydrostatic phase. Models^{7,8,21} of the first minutes after an impact vary greatly in their predictions. Reference 21 predicts fragment penetration to 100 bar and a gradual release of energy, ref. 7 predicts explosive vaporization at 10 – 100 mbar, whereas ref. 8 predicts it at 10 bar. Reference 8 further predicts a rapid ($\sim 10 \text{ km s}^{-1}$) rise of superheated gas that escapes the atmosphere and then falls back down onto the stratosphere over a range of several thousand kilometres. Because there are ~ 20 fragments of various brightnesses, we expect a range of actual impact altitudes and energies.

To bracket these uncertainties, we modelled heat deposition in the range of 10^{27} – 10^{30} erg at the predicted impact latitude of 43.9° S (10^{28} erg corresponds to a 1-km diameter fragment of density 1 g cm^{-3} and mass $5 \times 10^{14} \text{ g}$). Our hydrostatic model cannot handle large vertical accelerations, so we start our simulations well after the rise of gas by adding heat to a single layer instantaneously. The heat is spread over as small a disc as possible without violating the hydrostatic assumption; diameters are a few thousand kilometres. We did not run a 10^{30} -erg stratospheric case as the disc size was unrealistically large. Because models of the early event disagree on where the energy will ultimately go, we simulated stratospheric and tropospheric depositions, in the layers spanning 16–69 mbar and 287–1,197 mbar, respectively.

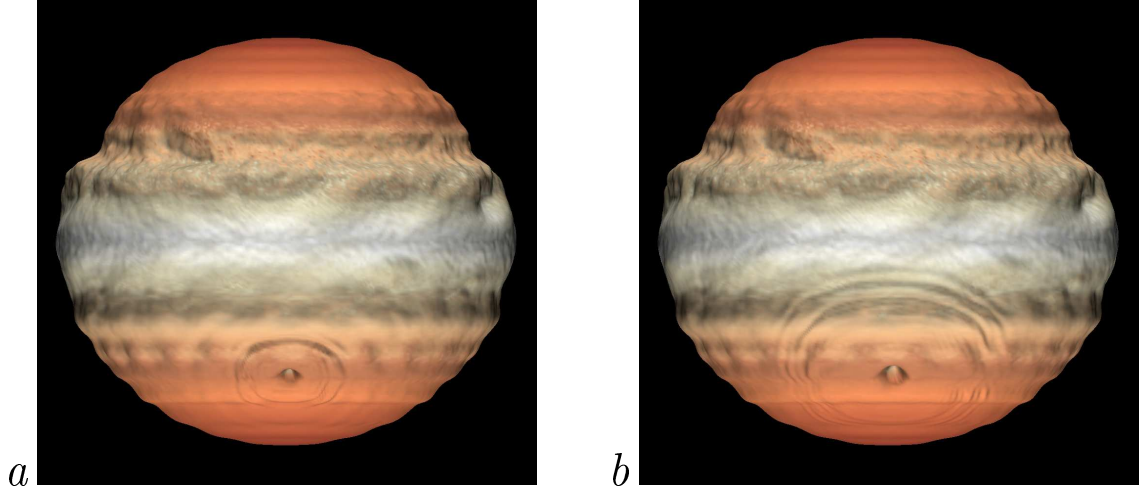


FIG. III.2 a, Simulation of Jupiter's atmosphere one day (24 h) after impact of a comet fragment. b, Same simulation two days after impact. 10^{28} erg were deposited in the layer spanning 16–69 mbar (stratospheric deposition); the 69-mbar pressure level is shown here. Height variations on the spheres correspond to changes in pressure, whereas colour corresponds to potential vorticity and indicates material initially at the same latitude. Inertia-gravity waves propagate outward from the impact site. The wave propagation rate is determined by the deformation radius, a key dynamical parameter that is uncertain in the troposphere. The circular coherence of the waves even after several days will facilitate detection of relatively small temperature fluctuations.

All our simulations show both a set of globally-propagating inertia-gravity waves and a longer-lived vortex at the impact site (see Fig. III.2). Vortex behaviour depends on local conditions, but in our longest-run case (10^{28} erg, stratospheric deposition, 36 d) the vortex sheared into two components that moved west-northwest and east-southeast. In all simulations inertia-gravity waves travel at $\sim 400 \text{ m s}^{-1}$ in the stratosphere and slower in the troposphere. There is an antipodal wave crossing, but no single focus of energy because of wave dispersion and Jupiter's oblateness. Because there is less mass and stronger stratification, stratospheric deposition excites stronger waves than tropospheric deposition (see Fig. III.1). Table III.1 contains each simulation's temperature deviation range. The waves interfere with one another behind the first wavefront, making it difficult to determine the functional form of the increase

of temperature range ΔT with comet energy, although it is not faster than linear.

TABLE III.1 Ranges of zonal temperature deviation profiles

| | 10^{27} erg | | 10^{28} erg | | 10^{29} erg | | 10^{30} erg | |
|-------------------------------------------------------|-------------------------|-------------------------|-------------------------|-------------------------|-------------------------|-------------------------|-------------------------|-------------------------|
| Pressure (mbar) | Day 1 ΔT (K) | Day 2 ΔT (K) | Day 1 ΔT (K) | Day 2 ΔT (K) | Day 1 ΔT (K) | Day 2 ΔT (K) | Day 1 ΔT (K) | Day 2 ΔT (K) |
| Stratospheric energy deposition (16–69-mbar layer) | | | | | | | | |
| 16 | 0.02 | 0.06 | 0.1 | 0.1 | 0.4 | 0.6 | | |
| 69 | 0.04 | 0.09 | 0.4 | 0.2 | 1.2 | 0.7 | | |
| 287 | 0.02 | 0.08 | 0.2 | 0.1 | 0.7 | 0.5 | | |
| 1,197 | 0.009 | 0.07 | 0.1 | 0.1 | 0.3 | 0.2 | | |
| 5,000 | 0.004 | 0.03 | 0.04 | 0.04 | 0.1 | 0.08 | | |
| Tropospheric energy deposition (287–1,197-mbar layer) | | | | | | | | |
| 16 | 0.004 | 0.02 | 0.01 | 0.04 | 0.07 | 0.04 | 0.3 | 0.3 |
| 69 | 0.009 | 0.02 | 0.04 | 0.07 | 0.3 | 0.1 | 0.4 | 0.4 |
| 287 | 0.009 | 0.03 | 0.04 | 0.1 | 0.2 | 0.1 | 0.5 | 0.3 |
| 1,197 | 0.01 | 0.04 | 0.06 | 0.2 | 0.06 | 0.1 | 0.3 | 0.9 |
| 5,000 | 0.007 | 0.02 | 0.02 | 0.05 | 0.1 | 0.1 | 0.7 | 0.8 |

Observers can probe different atmospheric levels by selecting wavelengths that are sensitive to different regions. The predicted temperature deviations caused by Shoemaker-Levy 9 inertia-gravity waves bracket the detection threshold for thermal infrared imaging, which probes the stratosphere^{22–24}. Transient condensation effects similar to those seen in mountain lee waves may be visible in high-resolution, reflected-light images of the waves’ horizontal passage through the ammonia clouds (upper troposphere). Whether such effects are indeed seen will depend upon local circumstances and the size of the wave. Inertia-gravity waves will be distinguishable from seismic waves¹⁹ by the former’s slower propagation rate and stronger thermal signature. Observers should be careful not to confuse the remnant signatures of seismic

effects close to the impact sites with those of propagating inertia-gravity waves. In all cases, techniques that take advantage of the waves' circular coherence (see Fig. III.2), such as averaging in radial bins around the impact locations, will improve the signal-to-noise ratio of the wave trace. Because of the uniqueness of this event and the potential for significant improvements in dynamical modelling, observers should attempt to determine inertia-gravity wave speeds at as many pressure levels as possible.

ACKNOWLEDGMENTS

We thank E. Charrette and the MIT Earth Resources Laboratory for programming assistance and use of their nCUBE 2 massively parallel computer. This work was funded by NASA.

REFERENCES

1. Nakano, S. *IAU Circ. No. 5800* (1993).
2. Carusi, A. & Yeomans, D. K. *IAU Circ. No. 5807* (1993).
3. Chodas, P. W. & Yeomans, D. K. *Bull. Am. Astr. Soc.* **25**, 1042–1043 (1993).
4. Dowling, T. E. *Bull. Am. Astr. Soc.* **25**, 1031 (1993).
5. Scotti, J. V. & Melosh, H. J. *Nature* **365**, 733–735 (1993).
6. Weaver, H. A. *et al. Science* **263**, 787–791 (1994).
7. Sekanina, Z. *Science* **262**, 382–387 (1993).
8. Zahnle, K. & Mac Low, M.-M. *Icarus* (in the press).
9. Conrath, B. J., Gierasch, P. J. & Nath, N. *Icarus* **48**, 256–282 (1981).
10. Dowling, T. E. & Ingersoll, A. P. *J. atmos. Sci.* **46**, 3256–3278 (1989).
11. Ingersoll, A. P. & Cuong, P. G. *J. atmos. Sci.* **38**, 2067–2076 (1981).
12. Marcus, P. S. *Nature* **331**, 693–696 (1988).
13. Williams, G. P. & Wilson, R. J. *J. atmos. Sci.* **45**, 207–241 (1988).
14. Melosh, H. J. & Schenk, P. *Nature* **365**, 731–733 (1993).
15. Hsu, Y.-J. G. & Arakawa, A. *Mon. Weath. Rev.* **118**, 1933–1959 (1990).
16. Dowling, T. E. *J. atmos. Sci.* **50**, 14–22 (1993).
17. Pirraglia, J. A., Conrath, B. J., Allison, M. D. & Gierasch, P. J. *Nature* **292**, 677–679 (1981).
18. Limaye, S. S. *Icarus* **65**, 335–352 (1986).
19. Marley, M. S. *Astrophys. J. Lett.* (in the press).

20. Klemp, J. B. & Lilly, D. K. *J. atmos. Sci.* **35**, 78–107 (1978).
21. Ahrens, T. J., Takata, T. & O’Keefe, J. D. *Bull. Am. Astr. Soc.* **25**, 1043 (1993).
22. Deming, D. *et al.* *Astrophys. J.* **343**, 456–467 (1989).
23. Gezari, D. Y. *et al.* *Nature* **342**, 777–780 (1989).
24. Orton, G. S. *et al.* *Science* **252**, 537–542 (1991).

Chapter 2

PREDICTION DETAILS AND LIMITATIONS

This chapter discusses modeling details, including the input energies and altitudes, the modifications made to the EPIC model to simulate the impact, the method for extracting the temperature deviation profiles, and some limitations of the simulations. It also presents additional temperature data for all of the model runs.

In general, the total energy available for side-effects of an inelastic collision of two objects in space is no more than the kinetic energy of the objects relative to each other at the moment of impact. This statement assumes that there are no sources of potential energy that would be released in the impact; the literature has not so far discussed such a possibility for the case of the P/Shoemaker-Levy 9 impact. The kinetic energy of an impactor is roughly

$$E \approx \frac{2}{3}\pi r^3 \rho v^2 \tag{III.1}$$

where E is the kinetic energy, r is the radius of the object, ρ is the mean density, and v is the velocity relative to the planet at impact. The analytical uncertainty arises from the unknown shape and density distribution of the object and the unknown mass of the coma. However, the large measurement uncertainties in ρ and r for the P/Shoemaker-Levy 9 fragments make the assumption of a spherical object with uniform density as good as any other set of assumptions. The comae are considered to have negligible mass. Table III.II gives several combinations of radius and density that yield the total kinetic energies considered in the impact model.

TABLE III.II
Impactor Sizes for Various Energies

| Impact Energy log(ergs) | Radius (meters) | | |
|-------------------------------|---------------------------------------|--------------------------------------------|---------------------------------------|
| | $\rho = 0.2 \text{ g/cm}^3$ (snow) | $\rho = 1.0 \text{ g/cm}^3$ (water ice) | $\rho = 5.0 \text{ g/cm}^3$ (rock) |
| 27 | 405 | 237 | 138 |
| 28 | 872 | 510 | 298 |
| 29 | 1,879 | 1,099 | 643 |
| 30 | 4,048 | 2,367 | 1,384 |

Several effects reduce the energy available to atmospheric dynamics from the total kinetic energy. First, the entire impactor is vaporized. It takes 2.6×10^{10} erg to turn 1 g of ice into steam, but the kinetic energy of 1 g moving at 60 km/sec is 1.8×10^{13} erg, so this is a small effect. Other minor effects include ionization of some of the impactor and atmosphere. Thermal radiation at tens of thousands of degrees Kelvin, lofting of the plume, and the formation of a downward-directed pressure pulse will be much larger effects. Depending on the circumstances, Zahnle and Mac Low (1994) predict that 20–40% of the impact energy will go into heat, pressure, and gravity waves, with

a few tenths of the impact energy ultimately remaining in the atmosphere as heat.

The highest published fragment diameter estimate is 4,300 meters (Weaver *et al.* 1994a). The largest post-impact plume in the simulations of Zahnle and Mac Low (1994) is about 800 km in diameter. These sizes are very small when considering the atmosphere of the largest planet; the 877-km equatorial grid size in the EPIC Jupiter model already challenges computational resources. All of the initial effects will therefore most likely happen below the model's spatial resolution. Even if spread over an entire horizontal grid cell, 10^{28} ergs is enough local heating to violate the hydrostatic assumption in the EPIC model, resulting in negative layer thicknesses. The ~ 10 km/sec rise of the plume in Zahnle and Mac Low's simulation confirms that the first minutes after impact are not hydrostatic.

Using the EPIC model therefore required some assumptions about the early atmospheric response in order to start a simulation after the nonhydrostatic period. The primary criterion for these models was that the simulation begin as soon after impact as possible. This is equivalent to saying that the energy be contained in as few cells as possible and that the model barely be hydrostatic at the beginning of the run. The version of EPIC used for these models defined three primitive variables (and their time derivatives) at each location: the eastward and northward wind speeds and the layer thickness (which corresponds to the pressure decrease per unit potential temperature increase).

Since the grid interval was roughly at the horizontal scale of the plume and was much larger than the impactor, and since an indeterminate amount of time would have passed before the atmosphere became hydrostatic, predicting meaningful horizontal winds would have been difficult without first modeling the initial event with a hydrodynamics code. Zahnle and Mac Low have not run their models to a completely hydrostatic state to date, though recent versions of their work do have much longer model runs than some of their earlier work (see below). Rather than inserting arbitrarily-chosen radial winds, the EPIC simulations changed only the layer thicknesses to represent an impact. Thickness modification corresponds to the addition of heat to the model, and occurred instantaneously between two timesteps in an otherwise-unmodified model.

Two different approaches to adding heat produced only slightly different qualitative results. The first approach was to warm cells in a vertical column proportionally to the mass in each cell. The column included all cells above a given detonation depth, and would have simulated an object depositing heat uniformly in the mass it encountered as it descended. Several conceptual problems arose with this method. First, for most energies the heat still was not distributed enough to prevent negative layer thicknesses without also spreading the heat horizontally. Second, both Sekanina (1993) and Zahnle and Mac Low (1994) predicted an even larger fraction of the impactor energy being deposited in the terminal layer than simple mass proportionality. Finally, it became clear from discussions with Zahnle and Mac Low as their work progressed that in their models even small impactors would explode well

below the EPIC simulation regime. Simulating their heat deposition would require an unacceptable extrapolation of the model $T(p)$ profile. Using the initial heat deposition patterns of their models was also questionable because the nonhydrostatic plume would redistribute the energy before the EPIC simulation began.

The second approach was to distribute the energy uniformly over a disc-like pattern of cells occupying only a single layer. Vertically-isolated heat sources would allow some characterization of how quickly the waves propagated vertically, although the inertia-gravity waves are nonlinear close to their source and superposition of solutions would not be possible. Part of the initialization sequence for each run was to adjust the disc size manually until it was as small as possible without resulting in negative layer thicknesses. Results from these runs were qualitatively similar to those from test runs using the first method. Table III.III presents the number of horizontal cells heated in each run, the corresponding heated area, and the temperature increase (ΔT) within those cells. The variation of the temperature in a given layer at lower energies is due to the small number of heated cells in those models; for example, the tropospheric 10^{27} -erg case easily contains its energy in one cell. All the heated cells in a given run received the same energy.

Recent results from Zahnle and Mac Low have exonerated early criticism of the high-altitude deposition of energy under the second heating approach. Their latest model, run to one hour after impact, shows large amounts of hot (>500 K) plume material raining down on the stratosphere at least to the boundaries of their simulation,

TABLE III.III
Sizes and Temperatures of Heating Discs

| Impact Energy (erg) | 16 – 69 mbar | | | 287 – 1,197 mbar | | |
|---------------------------|------------------------|------------------------------------|-------------------|------------------------|------------------------------------|-------------------|
| | Area Heated (cells) | (10 ⁶ km ²) | ΔT (K) | Area Heated (cells) | (10 ⁶ km ²) | ΔT (K) |
| 10 ²⁷ | 2 | 1.1 | 50.3 | 1 | 0.6 | 6.3 |
| 10 ²⁸ | 15 | 8.3 | 67.1 | 4 | 2.2 | 15.7 |
| 10 ²⁹ | 141 | 77.7 | 71.4 | 51 | 28.1 | 12.3 |
| 10 ³⁰ | | no run | | 507 | 279.5 | 12.4 |

5,000 km from the impact site. In addition to the descending material, their model shows several wave-like structures propagating outward, though the exact nature of those structure is not clear.

Each temperature deviation profile in Fig. III.1 and Fig. III.3, below, has input from two simulations: an impact run and a control run with no impact. Equation 5.44 of Hsu and Arakawa (1990),

$$T_l = \left(\frac{p_l}{p_0} \right)^\kappa \theta_l, \quad (\text{III.2})$$

gives the layer temperature T_l as a function of layer and reference pressures, p_l and p_0 , respectively, layer potential temperature, θ_l , and κ , the ratio of the gas constant to the specific heat at constant pressure. Vertically integrating layer thicknesses down from the top of the model atmosphere gives p_l , and the other parameters are all constants in the EPIC model. The temperature deviation profiles are the difference between the absolute temperature profiles of an impact run and a no-impact run.

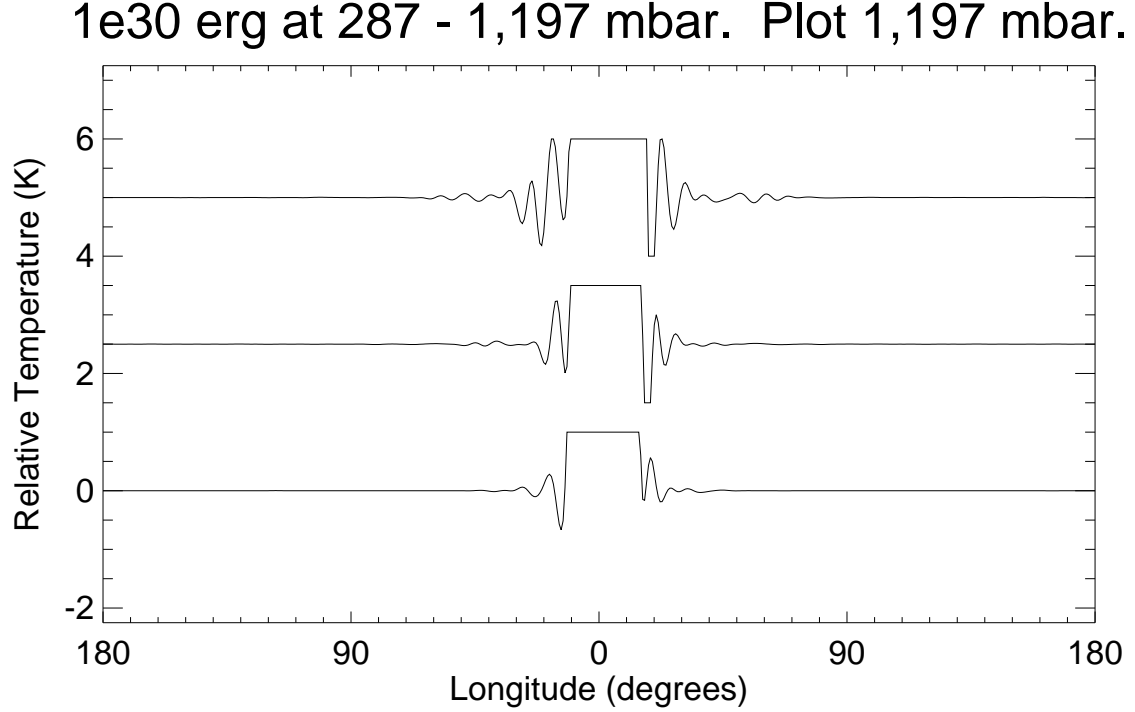
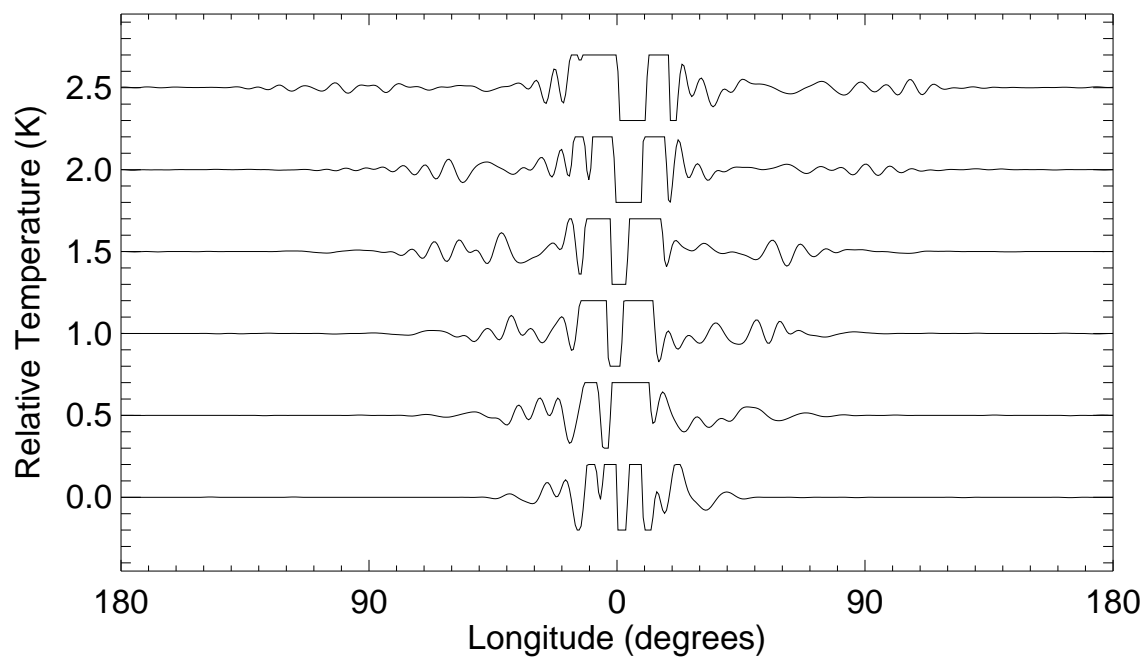


Fig. III.3. Time evolution of the waves in the first week. As in Fig. III.1, the profiles are temperature deviations relative to an unperturbed run. However, these are profiles only of the 1,197-mbar level, stacked in time sequence. The bottom profile in each panel is 24 hours after impact, and the later profiles are separated by this interval. The vertical temperature scale is relative; the large flat portion of each profile represents zero temperature deviation from an unperturbed model. The data are truncated above and below a given level so that the temperature scale of the waves, rather than that of the central disturbance, is most visible. The initial temperature perturbations are much larger than the waves (see Table III.III). We only ran the 10^{30} -erg model for three days.

1e29 erg at 16 - 69 mbar. Plot 1,197 mbar.



1e29 erg at 287 - 1,197 mbar. Plot 1,197 mbar.

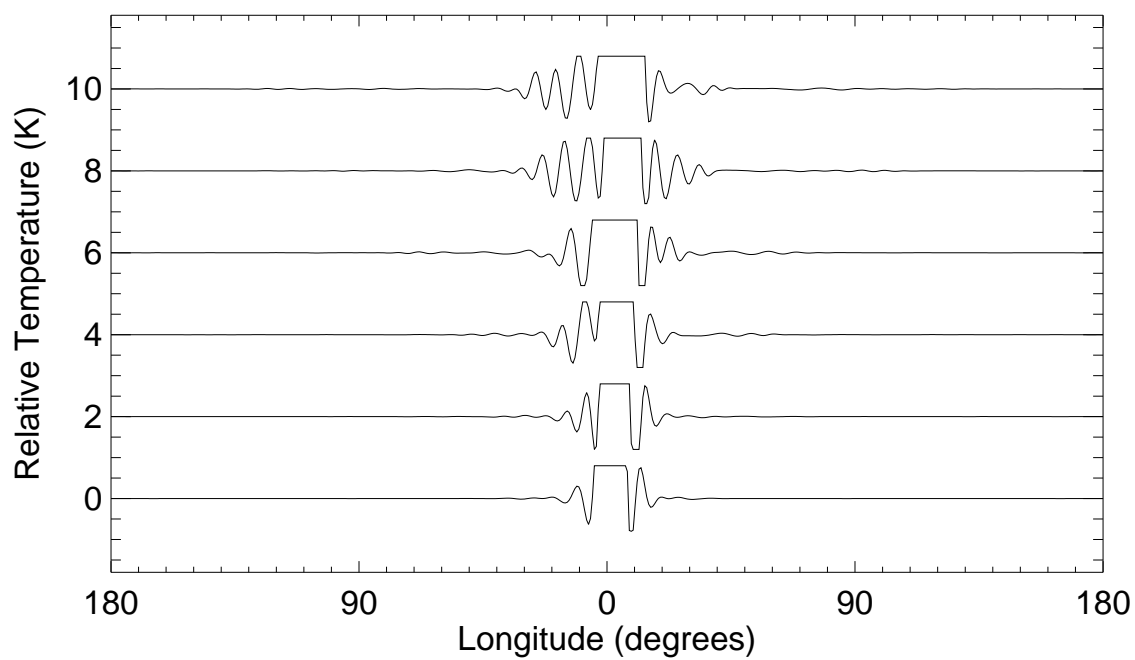
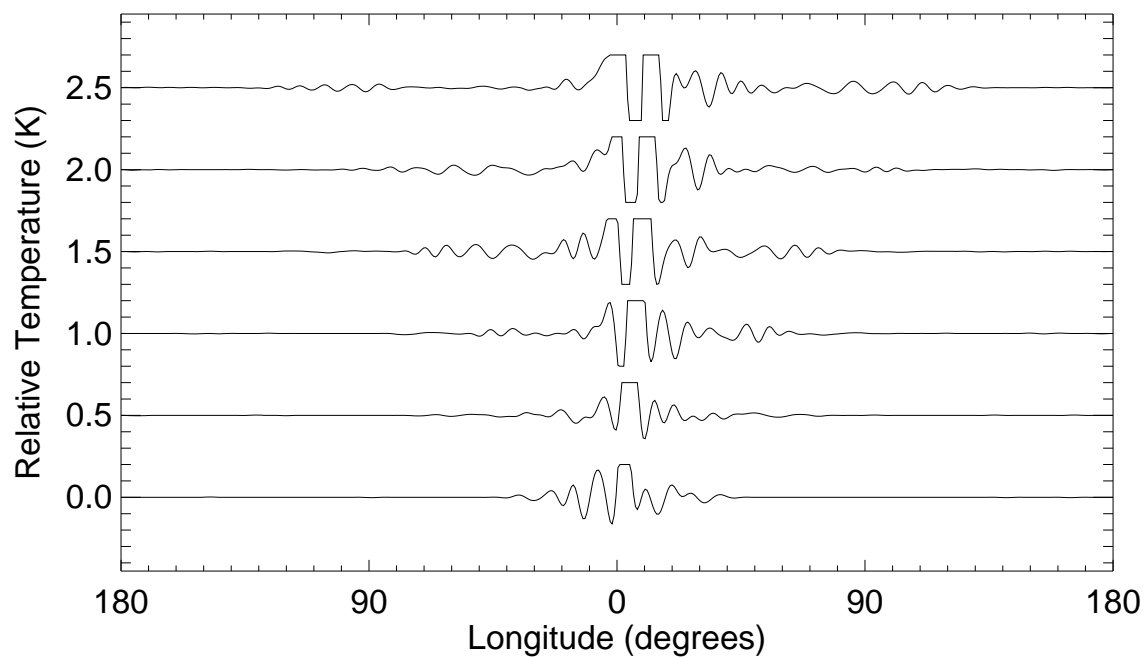


Fig. III.3—*Continued*

1e28 erg at 16 - 69 mbar. Plot 1,197 mbar.



1e28 erg at 287 - 1,197 mbar. Plot 1,197 mbar.

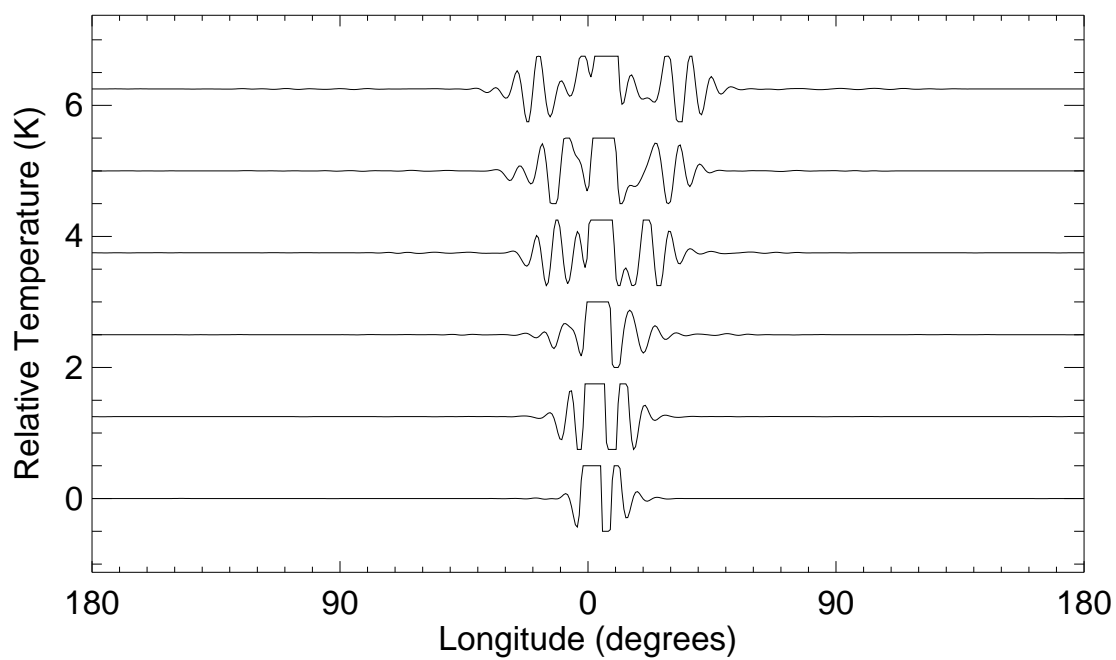
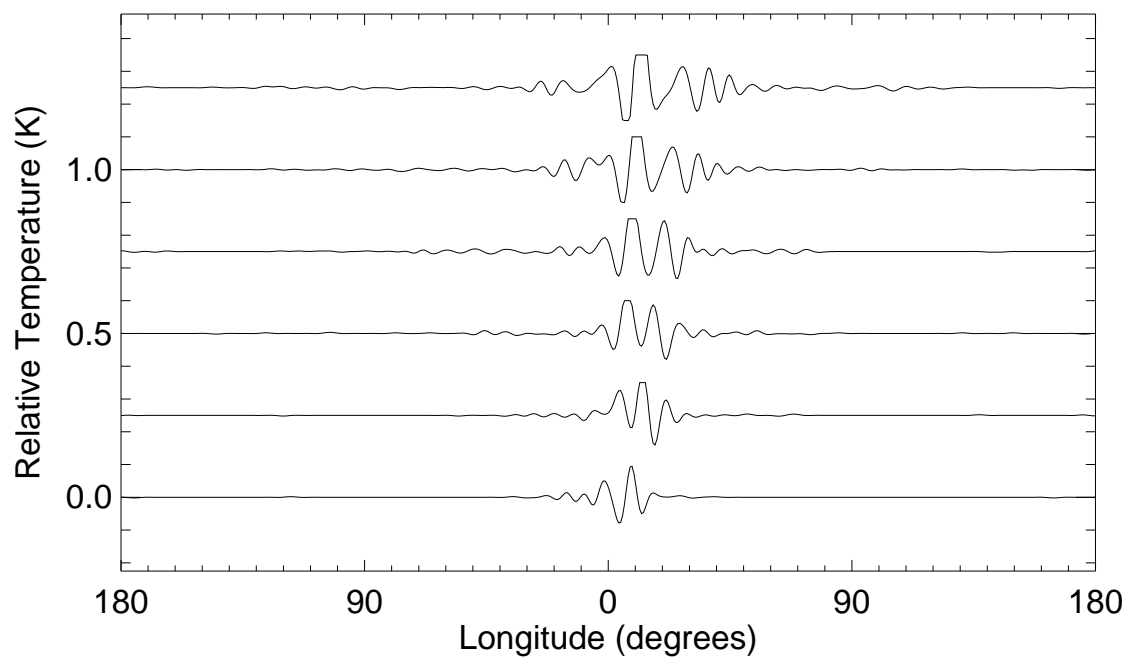


Fig. III.3—*Continued*

1e27 erg at 16 - 69 mbar. Plot 1,197 mbar.



1e27 erg at 287 - 1,197 mbar. Plot 1,197 mbar.

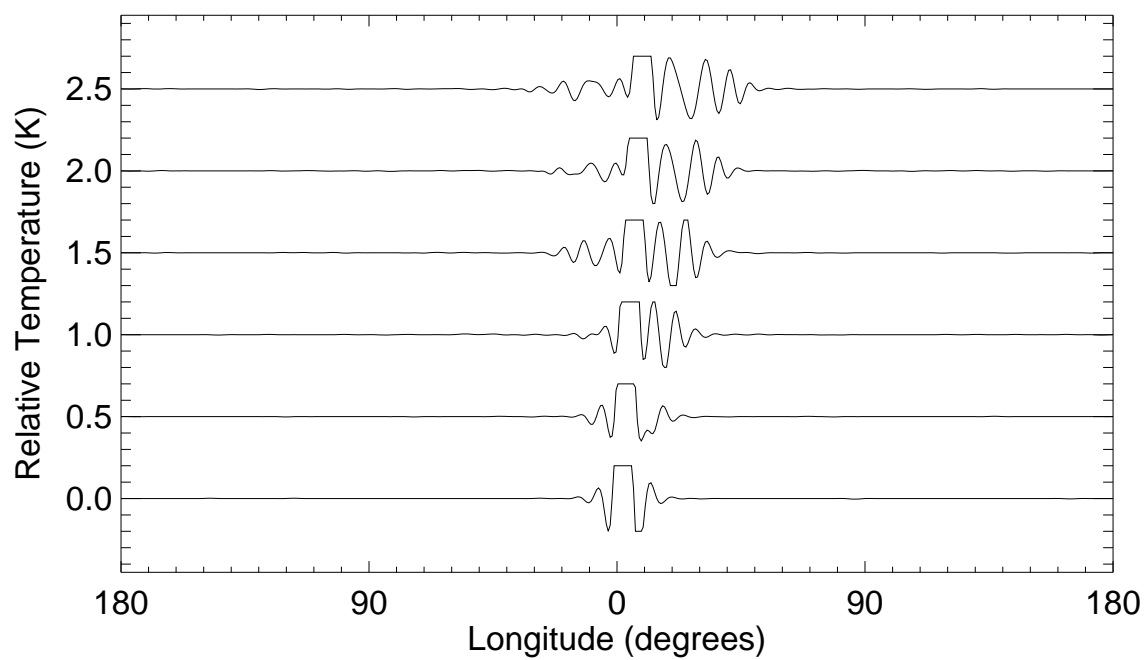


Fig. III.3—*Continued*

The leading wavefronts of the profiles are small compared to the undulations that follow them. This is unfortunate because the deformation radius is much easier to derive from a velocity measurement of the leading wavefront than from later peaks, but the model shows that the peaks will be easiest to detect. To show that still-larger waves do not emerge from the 20° masked zones of Fig. III.1, Fig. III.3 presents the full data from each model run, usually 6 days after impact. To restrict the number of plots, the figure only includes the 1,197-mbar level, but the other model layers have similar behavior in that waves with much larger amplitudes do not emerge after two days.

The wave pattern after several days is quite complex, particularly for stratospheric deposition. Comparing these cases to their tropospheric-deposition analogs, one can see that the fastest waves at this level appear to travel faster in the stratospheric-deposition cases. Since only one dispersion relation governs wave propagation at a given level, we conclude that these fast motions are due to downward propagation of the waves in the stratosphere. Taking the tropospheric-deposition cases as a guide, the amplitude of these fast forerunners is smaller than that of waves from the initial disturbance that propagated downward first, and then began to move horizontally. However, tropospheric speeds will be much easier to distinguish in the case of tropospheric deposition.

The accompanying videotape presents a rendering of the model data in the same manner as that of Fig. III.2. These renderings are primarily for a general audience,

but are also a practical way to present the full qualitative behavior of the model, particularly the 36-day run of the 10^{28} -erg, stratospheric-deposition case. Text segments on the tape prior to each video segment describe the following run. All of the segments but the first have, in addition to the round rendering of Fig. III.2, a rendering of all the layers decomposed into latitude and longitude, with the lowest layer corresponding to highest pressure.

There are several further limitations to the models presented here. These arise from sources including the hydrostatic approximation, the coarse vertical resolution, the choice of initial bottom condition, and finally the uncertainty in the impact energy and its actual deposition pattern.

The hydrostatic approximation has two main effects on the model: it makes the early impact impossible to simulate and it eliminates the vertical component of compression waves. The discussion of heating pattern, above, includes the first effect. Marley (1994) predicts that seismic waves (compression waves with periods of up to 140 sec) are likely to be an important effect immediately after the impacts. Because of the rapid change in the density of Jupiter's interior with depth, downward-propagating waves should refract, turn upward, and re-emerge some distance away from the impact site; waves with periods shorter than about 4 minutes would break in the stratosphere and deposit their energy as heat. The hydrostatic approximation eliminates these waves from the EPIC model, and the atmospheric shell that the model simulates is not thick enough to contain the depths at which Marley predicts

refraction.

The coarse vertical resolution of the models is not sufficient to predict detailed effects of the cloud decks on inertia-gravity waves. Ingersoll *et al.* (1994) used a specialized model to study tropospheric inertia-gravity wave propagation in more detail. Theirs is a linear model with two spatial dimensions, one horizontal and one vertical. The vertical resolution is high to resolve waves in the troposphere, where they use a moist adiabat. They find a waveguide in the troposphere that traps energy and produces temperatures much higher than those found in the EPIC impact simulations. However, their model is linear and cannot handle effects like breaking waves. It is therefore highly dependent on the initial hydrostatic adjustment process, and none of the sub-kilometer-resolution models have been run to a hydrostatic state so far. Still, the version of the EPIC model used for the impact simulation cannot address the question of cloud decks as wave guides.

Chapter 3

CONCLUSIONS

The EPIC impact simulations serve primarily to characterize the relative importance of different dynamical effects and to determine time and rough temperature scales useful in planning observations of the event. The models show that even impacts that are an order of magnitude larger than the currently-expected energies are not individually large enough to disrupt the zonal wind pattern or to create major storms on the scale of the Great Red Spot. If observers can determine the speeds of inertia-gravity waves with sufficient vertical resolution, that information will be directly useful to dynamical modeling.

Cometary impacts have been linked to the extinction of the dinosaurs (Sharpton *et al.* 1993) and to the delivery of the Earth's water in the early part of this planet's history (Pepin 1989). The Shoemaker-Levy 9 impacts will be the first such collisions to be witnessed by humanity. Despite diligent efforts by many different groups,

no single model currently simulates all or even very many aspects of the impact aftermath; there are interactions between scales and types of physics that specialized models cannot simulate, such as the effect on the weather of stratospheric heating caused by breaking seismic waves (Marley 1994). Astronomers should recognize the impossibility of modeling so many effects with current computing technology and plan broad and flexible observing campaigns that maximize the likelihood of detecting the unexpected. It is unlikely that we will have a similar opportunity again in our lifetimes (Melosh and Schenk 1993).

REFERENCES

- AHRENS, T. J., T. TAKATA, AND J. D. O'KEEFE 1993. Comet Shoemaker-Levy 9 Impact on Jovian Atmosphere. *Bull. Amer. Astron. Soc.* **25**, 1043.
- BAINES, K. H., R. A. WEST, L. P. GIVER, AND F. MORENO 1993. Quasi-Random Narrow-Band Model Fits to Near-Infrared Low-Temperature Laboratory Methane Spectra and Derived Exponential-Sum Absorption Coefficients. *J. Geophys. Res.* **98**, 5517–5529.
- CARUSI, A., AND D. K. YEOMANS 1993. Periodic Comet Shoemaker-Levy 9 (1993e). *IAU Circ. No. 5807*.
- CHODAS, P. W. AND D. K. YEOMANS 1993. Periodic Comet Shoemaker-Levy 9 (1993e). *Bull. Amer. Astron. Soc.* **25**, 1042–1043.
- CONRATH, B. J., P. J. GIERASCH, AND N. NATH 1981. Stability of Zonal Flows on Jupiter. *Icarus* **48**, 256–282.
- DEMING, D., M. J. MUMMA, F. ESPENAK, D. E. JENNINGS, T. KOSTIUK, G. WIEDEMANN, R. LOEWENSTEIN, AND J. PISCITELLI 1989. A Search for p -Mode Oscillations of Jupiter: Serendipitous Observations of Nonacoustic Thermal Wave

- Structure. *Astrophys. J.* **343**, 456–467.
- DOWLING, T. E., AND A. P. INGERSOLL 1989. Jupiter’s Great Red Spot as a Shallow Water System. *J. Atmos. Sci.* **46**, 3256–3278.
- DOWLING, T. E. 1993a. A Relationship between Potential Vorticity and Zonal Wind on Jupiter. *J. Atmos. Sci.* **50**, 14–22.
- DOWLING, T. E. 1993b. An Explicit Planetary Isentropic-Coordinate Atmospheric Model for Jupiter, Saturn, Uranus, and Neptune. *Bull. Amer. Astron. Soc.* **25**, 1031.
- GEZARI, D. Y., M. J. MUMMA, F. ESPENAK, D. DEMING, G. BJORAKER, L. WOODS, AND W. FOLZ 1989. New features in Saturn’s atmosphere revealed by high-resolution thermal infrared images. *Nature* **342**, 777–780.
- HSU, Y.-J. G., AND A. ARAKAWA 1990. Numerical Modeling of the Atmosphere with an Isentropic Vertical Coordinate. *Monthly Weather Rev.* **118**, 1933–1959.
- INGERSOLL, A. P., AND P. G. CUONG 1981. Numerical Model of Long-Lived Jovian Vortices. *J. Atmos. Sci.* **38**, 2067–2076.
- INGERSOLL, A. P., H. KANAMORI, AND T. E. DOWLING 1994. Atmospheric gravity waves from the impact of comet P/Shoemaker-Levy 9 with Jupiter. *Geophys. Res. Lett.* **21**, 1083–1086.
- KLEMP, J. B., AND D. K. LILLY 1978. Numerical Simulation of Hydrostatic Mountain Waves. *J. Atmos. Sci.* **35**, 78–107.
- LIMAYE, S. S. 1986. Jupiter: New Estimates of the Mean Zonal Flow at the Cloud Level. *Icarus* **65**, 335–352.
- MARCUS, P. S. 1988. Numerical simulations of Jupiter’s Great Red Spot. *Nature*

331, 693–696.

- MARLEY, M. S. 1994. Seismological Consequences of the Collision of Comet Shoemaker-Levy/9 with Jupiter. *Astrophys. J. Lett.* **427**, L63–L66.
- MELOSH, H. J., AND P. SCHENK 1993. Split comets and the origin of crater chains on Ganymede and Callisto. *Nature* **365**, 731–733.
- NAKANO, S. 1993. Periodic Comet Shoemaker-Levy 9 (1993e). *IAU Circ. No. 5800*.
- ORTON, G. S., A. J. FRIEDSON, J. CALDWELL, H. B. HAMMEL, K. H. BAINES, J. T. BERGSTRALH, T. Z. MARTIN, M. E. MALCOM, R. A. WEST, W. F. GOLISCH, D. M. GRIEP, C. D. KAMINSKI, A. T. TOKUNAGA, R. BARON, AND M. SHURE 1991. Thermal Maps of Jupiter: Spatial Organization and Time Dependence of Stratospheric Temperatures, 1980 to 1990. *Science* **252**, 537–542.
- ORTON, G. S., A. P. INGERSOLL, R. J. TERRILE, AND S. R. WALTON 1981. Images of Jupiter from the Pioneer 10 and Pioneer 11 Infrared Radiometers: A Comparison with Visible and 5-micron Images. *Icarus* **47**, 145–158.
- PEPIN, R. O. 1989. Atmospheric Compositions: Key Similarities and Differences. In *Origin and Evolution of Planetary and Satellite Atmospheres*, pp. 291–305. Univ. of Arizona Press, Tucson.
- PIRRAGLIA, J. A., B. J. CONRATH, M. D. ALLISON, AND P. J. GIERASCH 1981. Thermal structure and dynamics of Saturn and Jupiter. *Nature* **292**, 677–679.
- SCOTTI, J. V., AND H. J. MELOSH 1993. Estimate of the size of comet Shoemaker-Levy 9 from a tidal breakup model. *Nature* **365**, 733–735.
- SEKANINA, Z. 1993. Disintegration Phenomena Expected During Collision of Comet Shoemaker-Levy 9 with Jupiter. *Science* **262**, 382–387.

- SHARPTON, V. L., K. BURKE, A. CAMARGO-ZANOQUERA, S. A. HALL, D. S. LEE, L. E. MARÍN, G. SUÁREZ-REYNOSO, J. M. QUEZADA-MUÑETON, P. D. SPUDIS, J. URRUTIA-FUCUGAUCHI 1993. Chicxulub Multiring Impact Basin: Size and Other Characteristics Derived from Gravity Analysis. *Science* **261**, 1564–1567.
- WEAVER, H. A., P. D. FELDMAN, M. F. A’HEARN, C. ARPIGNY, R. A. BROWN, E. F. HELIN, D. H. LEVY, B. G. MARSDEN, K. J. MEECH, S. M. LARSON, K. S. NOLL, J. V. SCOTTI, Z. SEKANINA, C. S. SHOEMAKER, E. M. SHOEMAKER, T. E. SMITH, A. D. STORRS, D. K. YEOMANS, AND B. ZELLNER 1994a. Hubble Space Telescope Observations of Comet P/Shoemaker-Levy (1993e). *Science* **263**, 787–791.
- WEAVER, H. A. 1994b. Periodic Comet Shoemaker-Levy 9 (1993e). *IAU Circ. No.* 5947.
- WILLIAMS, G. P., AND R. J. WILSON 1988. The Stability and Genesis of Rossby Vortices. *J. Atmos. Sci.* **45**, 207–241.
- ZAHNLE, K., AND M.-M. MAC LOW 1994. The Collision of Jupiter and Comet Shoemaker-Levy 9. *Icarus* **108**, 1–17.